From the holdings of the Department of Special Collections , Princeton University Library, Princeton, NJ

These documents are either in the public domain, or can only be used for educational and research purposes (Fair use) as per U.S. Copyright law (text below). By accessing this file, all users agree that their use falls in the public domain or within fair use as defined by the copyrightlaw. We do not charge any permission or usage fees for the publication of images of material inour collections, including those provided by Princeton University Library, via our website, catalog, or directly from staff.For more information regarding copyright, credit, and citation please review the information onthe Copyright, Credit and Citation Guidelines page of our website.
https://library.princeton.edu/special-collections/policies/copyright-credit-and-citation-guidelines. If you have any questions, including how to order higher-quality images from the collection, contact Special Collections Public Services via our Ask Us! Form. https://library.princeton.edu/special-collections/ask-us

---

Doctoral Dissertations, 2011-2026 Atmospheric and Oceanic Sciences

---

2014

Variability and Trends in the Carbon Cycle

Majkut, Joseph

Princeton, NJ : Princeton University

---

http://arks.princeton.edu/ark:/88435/dsp01qj72p936q

U.S. Copyright law: The copyright law of the United States (Title 17, §108, United States Code) governs the making of photocopies or other reproductions of copyrighted material. Under certain conditions specified in the law, libraries and archives are authorized to furnish a photocopy or other reproduction. One of these specified conditions is that the photocopy or reproduction is not to be used for any purpose other than private study, scholarship, or research. If a user makes a request for, or later uses, a photocopy or reproduction for purposes in excess of fair use that user may be liable for copyright infringement. This institution reserves the right to refuse to accept a copying order if, in its judgment, fulfillment of the order would involve a violation of copyright law. https://www.copyright.gov/title17/title17.pdf

Variability and Trends in the Carbon Cycle

Joseph Daniel Majkut

A Dissertation
Presented to the Faculty
of Princeton University
in Candidacy for the Degree
of Doctor of Philosophy

Recommended for Acceptance
by the Program in
Atmospheric and Oceanic Sciences
Adviser: Professor Jorge L. Sarmiento

September 2014

© Copyright by Joseph Daniel Majkut, 2014.

All rights reserved.

Abstract

This thesis examines the mechanisms that control the removal of anthropogenic CO_2 from the atmosphere on timescales of decades to centuries. I focus on applying Bayesian statistical methods to constrain models of CO_2 uptake, detect trends from observations and provide uncertainty analysis for integrated assessment models for climate change.

I first apply a data assimilation technique to a newly-released database of surface ocean carbon measurements. This application uses model-based information to compensate for data sparsity in a novel way and globally maps trends in the partial pressure of surface ocean pCO_2. The results provide a new estimate of the growth in the total air-sea flux of CO_2 and regional trend estimates. In particular, the result in the Southern Ocean provides new insights into the physical and chemical controls on CO_2 uptake in that region of the ocean.

I then review model and data-based estimates of the Southern Ocean CO_2 uptake and how it may change under climate change. I use an observational system observing experiment to show that the standing uncertainty in Southern Ocean CO_2 uptake could be resolved with a float-based sampling network with between 150-200 members. I also show that changes to Southern Ocean CO_2 fluxes predicted by models as a result of climate change will take decades to detect directly.

The last chapter focuses on the implications of uncertainty in the present and future carbon cycle for models that are used to price CO_2 emissions as an externality of economic growth. The scientific contribution quantifies the implications of the large uncertainty in estimates of historical land use emissions of CO_2 to future projections. This study novelly highlights the critical role that uncertainty in the response of the natural carbon sinks plays in evaluating the economic impacts of climate change and quantifies how reductions in that uncertainty can be used to improve the efficiency of climate policy design.

Acknowledgements

I would like to acknowledge my colleagues, friends and teachers from the Princeton University Program in Atmospheric and Oceanic Sciences and the NOAA Geophysical Fluid Dynamics Laboratory for creating a stimulating and exciting environment in which to do research. Pursuing a Ph.D. here, with my 2009 cohort, has been a privilege.

Foremost consideration goes to my advisor, Jorge Sarmiento. I am honored to have been included in his dynamic and fascinating group and to have been given the freedom and support to define my own research. I can only hope to one day attain his mastery over ideas, teaching, and the patient pursuit of scientific inquiry.

The work presented in this thesis has benefited from the input and help of collaborators and coauthors. Rick Slater and Eric Galbraith taught me how to run and analyze GCMs. Keith Rodgers has been a generous colleague, coauthor and mentor. So too have Thomas Frölicher, Carolina Dufour, Brendan Carter, Michael Oppenheimer and Robert Kopp.

My studies and endeavors have benefited from the wisdom of many other advisors here in Princeton, including my advisory committee and examiners. Others include Rob Socolow, John Danner and Greg van der Vink. Bob Hallberg deserves special mention. His early encouragement led me to Princeton and I am very grateful for his continued advice.

I thank the residents of Sayre Hall for providing an engaging and supportive environment, especially Anna Valerio, Laura Rossi, Bob Key and my fellow graduate students and postdocs.

Friends, family and colleagues who have seen me along the way are too many to list, dearly appreciated and overshadowed by Stephanie.

Dedicated to John Evans,

my little grandfather.

Contents

Abstract iii

Acknowledgements iv

List of Tables ix

List of Figures xi

1 Introduction **1**

1.1 Role of the Ocean 3

1.1.1 Southern Ocean Observations 5

1.2 Land-Biosphere and Climate Policy 6

1.3 Publication, Coauthorship and Funding Sources 7

2 Ocean Flux History **9**

2.1 Introduction 9

2.2 Methods 12

2.2.1 Estimating pCO_2 time series 13

2.2.2 MCMC Inversion 15

2.2.3 Calculating Fluxes from pCO_2 16

2.2.4 Defining Inversion Parameters 18

2.2.5 Demonstration Study 20

2.3 Results 24

2.3.1 MCMC output 25

2.3.2 Flux Estimates 26
2.3.3 Sensitivity Studies 28
2.4 Discussion 33
2.4.1 Pacific 34
2.4.2 Atlantic 35
2.4.3 Southern Ocean 36
2.5 Conclusions 41

3 Southern Ocean Carbon Trends: Modeling and Detection 43
3.1 Review of Southern Ocean CO_2 uptake 46
3.1.1 Decadal estimates 48
3.1.2 Southern Ocean carbon-climate feedbacks 52
3.2 Float-based sampling experiment 55
3.2.1 Estimates 58
3.2.2 Trend detection 61
3.2.3 Sensitivity Studies 61
3.3 Discussion 64
3.4 Conclusions 67

4 Carbon System Feedbacks and Climate Policy 70
4.1 Introduction 70
4.2 Model Formulation 73
4.2.1 Carbon Cycle Model 74
4.2.2 Energy Balance 77
4.2.3 Economic Factors 78
4.3 Parameter Estimation via MCMC 81
4.3.1 Emulating Earth System Models 82
4.3.2 MCMC Inversion 84

4.3.3 Model Forcing 87
4.4 Results 88
4.4.1 Sampling Results 88
4.4.2 Integrated Assessment 93
4.4.3 Policy Implications 100
4.5 Conclusions 102

A Ocean Flux Supplement **116**
A.1 Model Information 116
A.2 Timeseries 117
A.3 Regional Trends and Fluxes 125

Bibliography **131**

List of Tables

2.1 pCO_2 Slope Estimates 35

2.2 Alternative pCO_2 estimates 37

2.3 pCO_2 Component Trends 38

4.1 Linear feedback parameters the simple carbon model and earth system models 111

4.2 Carbon cycle model parameter estimates 112

4.3 Carbon cycle model parameter correlation 112

4.4 Excess atmospheric CO_2 and net land uptake under BAU and efficient policies in 2025, 2050 and 2100. Median values are shown as the estimate with the 5-95% confidence range. 113

4.5 Expected consumption benefit of distinguishing LUC case, shown as net present value [NPV, 2005$ billion] and as a fixed percentage of consumption from 2010-2310 [%] 114

4.6 Key of carbon model parameters, based on SCCM Raupach (2013); Harman et al. (2011) 115

A.1 Coupled ocean-biogeochemistry models and reanalysis forcings 116

A.2 Coupled CMIP5 ocean-atmosphere-biogeochemistry models 117

A.3 pCO_2 Slope Estimates 126

A.4 Regional Flux Estimates 127

A.5 Regional Slope Sensitivity (μatm yr^{-1}) 128
A.6 Regional Flux Sensitivity (1e-3 PgC yr^{-1}) 129

List of Figures

2.1 These figures show (a) pCO_2 time series and (b) the distributions associated with the parameter A for a grid cell in the Eastern Pacific. The green line shows the posterior estimate for the pCO_2 time series and the magenta shows the prior estimate. The red dots indicate the monthly-averaged measurements from LDEO2010. 14

2.2 This figure shows different pCO_2 slope estimates $\mu atm\ yr^{-1}$ for the GFDL ESM2M verification experiment. The true case, (a), is the slope of the fully-sampled model pCO_2, A_{full}. Panel (b) shows the same slope calculated by MCMC, A_{mcmc}, with the synthetic LDEO2010 measurements. Panel (c) shows the sub-sampled slope A_{sub}, calculated from the synthetic data with ordinary least squares. Panel (d) shows the prior used to initialize the MCMC from (b). Panel (e) shows A_{iav}, the bias in slope that results when subsampling the IAV term. Lastly, panel (f) shows the sum of A_{sub} and A_{iav}. 23

2.3 The prior and posterior means (a,b) and standard deviations (c&d) for the slope parameter, A, and the intercept term, B, (e,f,g,h) for the MCMC inversion of LDEO2010. The coloring in (a,b) indicates growth with respect to the atmospheric growth rate (blue indicates slower than atmospheric growth) and in (e,f) indicates the 06/1995 value with respect to the atmospheric pCO_2 (blue indicates ocean uptake of CO_2). 27

2.4 The posterior mean estimates for the scaling parameters (a) C and (b) D from the MCMC inversion of LDEO2010. Values smaller than 1 indicate that the amplitude of the imposed variability has been muted by the inversion. 28

2.5 The mean flux, 1995-2005, from the MCMC pCO_2 inversion is shown in panel (a). Panel (b) shows the difference between the MCMC-derived flux in (a) and the climatology of (Takahashi et al., 2009a). Positive values mean less uptake in the MCMC-derived estimates. 29

2.6 The total uptake of anthropogenic CO_2 timeseries, 1980-2009, for the MCMC featuring the MOM4p1-Bling seasonal cycle (green) and the empirical seasonal cycle (red) and the MCMC version with the MOM4p1-Bling seasonal cycle and no interannual variability (black). The dotted lines indicate $\pm$ 1 σ for the global integral, including the uncertainty in gas exchange piston velocity. The red dot and associated error bars represent the anthropogenic uptake calculated by (Takahashi et al., 2009a) of 2.0 $\pm$ 1.0 PgC yr^{-1}. The black triangles show the the decadally-averaged estimates from (Khatiwala et al., 2009). The other box and whisker plots indicate other estimates for anthropogenic CO_2 uptake by the ocean from table 1 in (Gruber et al., 2009). 30

2.7 Panel (a) shows the difference in the mean of A between the standard MCCM inversion and the run with no interannual variability and panel (b) shows the same between the standard case and the run with the MOM4p1-Bling based seasonality. In both panels, positive values indicate faster growth in the standard case. Panel (c) shows the difference in mean year 2000 flux between the standard and no interannual variability cases and panel (d) shows the same for the seasonal difference. Here positive values indicate more outgassing or less uptake. 32

2.8 Panel (a) shows the MCMC slope estimate for the Southern Ocean in μatm yr^{-1}. Panel (b) is the trend in the temperature-driven component of pCO_2, and (c) shows the non-temperature component trend. 40

3.1 The number of surface measurements of pCO_2 in gridded SOCAT v2, between 1995 and 2012. (a) Total monthly observations, south of 30 ° S, with winter months (June-July-August) in red. (b) Calendar months occupied, where twelve indicates full occupation of the seasonal cycle and white indicates no available measurements. 44

3.2 The cumulative fluxes integrated from 90°S to 90°N, in PgC yr^{-1}, of (a) anthropogenic CO_2 and (b) total CO_2. Estimates come from forced (red) and coupled (blue) OGCMs averaged over 1995-2005 and show significant spread by 30 °S. The black line in (a) shows the oceanic inversion results from Mikaloff-Fletcher et al. (2007). In (b), the LDEO pCO2 year 2000 climatological flux is in black and the MCMC pCO2 history, averaged over 1995-2005, is in green. 49

3.3 The seasonal cycle of CO_2 uptake into the Southern Ocean, south of 45° S, in Pg C yr^{-1}. The CMIP5 models are shown in blue, MOM4p1-BLING models in red, and the LDEO pCO_2 climatology in black and the MCMC pCO_2 history in green. The area south of 45°S was chosen to avoid contaminating the seasonal cycle with subtropical signals. . 51

3.4 (a) The impact of climate change on the total global ocean CO_2 uptake between 1970-2005. The time series show the uptake of CO_2, with (dashed) and without (solid) climate variability, by the ocean from CMIP5 (blue) and MOM4p1-BLING simulations (red). The MCMC uptake is shown in green and an extrapolation of the Mikaloff-Fletcher inversion is shown in solid black. (b) The climate impact on CO_2 uptake, in PgC, integrated over 1970-2005 and northward from 90°S for each model. (c) The climate impact on CO_2 uptake, in PgC, integrated over 1860-2100 and northward from 90°S for the RCP4.5 simulations 53

3.5 The modeled annual flux, in mole m^{-2} yr^{-1}, from the ESM2M historical simulation is shown as calculated (a) directly on the fully sampled model grid and (b) using 200 randomly distributed and stationary floats with a 20% sampling error. The true flux for the year was 0.79 PgC and the reconstruction shown here results in a flux of 0.76 PgC. 57

3.6 The annual reconstruction of the Southern Ocean CO_2 uptake, in PgC yr^{-1}, from the ESM2M historical simulation years over the period from 1996 to 2000 (top) and the averaged monthly uptake values for the 5 year reconstruction (bottom). The black line connects the true values of the flux. The blue bars show the $\pm 1\sigma$ uncertainty for each estimate, based on a 1000 member Monte Carlo simulation of 200 floats with 20% fractional sampling error. 60

3.7 Minimum detectable trend (red lines), in Pg C yr^{-1} $decade^{-1}$, is a function of the number of years of monthly sampling, the error in the monthly estimates and the autocorrelation in the timeseries of uptake. Fifteen years of continuous monthly sampling are required to capture the historical trend associated with the uptake of anthropogenic CO_2 in the southern ocean (blue diamond, 0.2 Pg C yr^{-1} $decade^{-1}$). More than 20 years are required to capture a trend with the magnitude expected from changes in the overturning circulation (green circle, -0.08 Pg C yr^{-1} $decade^{-1}$). 62

3.8 The proportion of months for which the bootstrapped error estimate is larger than the threshold value of 1 mole m^{-2} yr^{-1}. The area of exceedance decreases from samplings with 75 (top), 200 (middle) and 400 (bottom) floats. The bootstrapped errors come from the 1000 member Monte Carlo simulation for each number of floats. 63

3.9 Error estimates for the annual reconstruction of the Southern Ocean CO_2 uptake, in PgC, for varying number of floats (left). The error estimates are calculated as the standard deviation of the basin-integrated annual CO_2 flux from the reconstructed fields and the true model. The percentage of the Southern Ocean, south of 30° S, where the monthly error estimate is larger than the threshold value of 1 mole m^{-2} yr^{-1} (right). In both plots, different lines reflect reconstructions with varying levels of sampling error. The error in the estimate of total uptake is less sensitive to the sampling error than the percentage of exceedance. 65

4.1 The cumulative annual emissions of CO_2 [GtC] from 1850 to present day. The cumulative emissions plots show the substantial difference in the estimates of LUC emissions rates before 1960. 104

4.2 Hindcasts of the CO_2 budget shown as atmospheric CO_2 concentration [ppm], total oceanic uptake [GtC] and net land uptake [GtC] for historical simulations under the BOOK and ISAM LUC cases. 105

4.3 Histograms of 1000 samples from the MCMC chains for the carbon cycle parameters (a) m_{NPP} [-], (b) q_{10} [-], (c) k_{m1} [yr^{-1}] and (d) k_{m2} [yr^{-1}]. Prior distributions are shown in grey. 106

4.4 Projections of atmospheric CO_2 [ppm] and temperature warming [°C] for business as usual (BAU) and efficient policies: (a) Atmospheric CO_2 under BAU, (b) Temperature change under BAU, (c) Atmospheric CO_2 under efficient policy, and (d) Temperature change under efficient policy. The credible confidence range (5-95th percentile) is shown separately for the BOOK and ISAM LUC posterior parameters. The thin dashed line shows results for the DICE2013 prediction of atmospheric CO_2. 107

4.5 The social cost of carbon [SCC, \$ ton^{-1}] under different damage functions (upper values: cubic, lower values: quadratic) and different policy scenarios: (a) business as usual and (b) efficient policies. Crosses show the SCC calculated with uncertainty in the carbon system; the horizontal hatch mark shows the SCC and the vertical line shows the range in SCC estimates for each case. Values are shown for the combined (grey, center), BOOK (green, left) and ISAM (magenta, right) LUC cases. The long horizontal lines are the coincident SCC values calculated with the DICE2013 carbon cycle. 108

4.6 The optimal carbon tax [\$ ton^{-1}] under different parameterizations of the carbon system (combined, grey; BOOK, green; ISAM, magenta). 109

4.7 The mitigation effort necessary to limit warming to a threshold of 2.5° C under the different LUC cases in our model (combined, grey; BOOK, green; ISAM, magenta), shown as (a) cumulative emissions post-2010 [GtC] and (b) total mitigation burden [2005$ NPV]. 110

A.1 Southern Ocean Results, < 45S: RMSE in region and 4 example timeseries 118

A.2 Southern Ocean Results, <30S, >45S: RMSE in region and 4 example timeseries 119

A.3 Indian Ocean Results: RMSE in region and 4 example timeseries . . . 120

A.4 Equatorial Pacific Results: RMSE in region and 4 example timeseries 121

A.5 North Pacific Results: RMSE in region and 4 example timeseries . . . 122

A.6 Subpolar North Atlantic Results: RMSE in region and 4 example timeseries 123

A.7 Subtropical North Atlantic Results: RMSE in region and 4 example timeseries 124

A.8 The CARBONTRACKER regions used for dividing the ocean are mapped and labeled in this figure. 130

Chapter 1

Introduction

Over much of the last 400,000 years, the atmospheric concentration of carbon dioxide has been relatively stable. As the earth moved from cold glacial conditions to warm interglacials, atmospheric CO_2 varied between 180 and 300 ppm, as evidenced by the concentration of CO_2 in ice-trapped bubbles taken from Antarctic glaciers (Petit et al., 1999). This stability indicates a fairly consistent balance between the major reservoirs of CO_2 that readily exchange with the atmosphere, the ocean and land biosphere. Over that time period, the ocean and land carbon stocks maintained a rather steady inventory of carbon, holding approximately 38000 and 4000 GtC respectively (1 GtC $\sim$ 2.13 ppm, 1 GtC $\sim$ 3.67 Gt CO_2).

Since the dawn of the industrial age, atmospheric CO_2 has increased sharply, from the preindustrial average of 278 ppm to 401 ppm at the time of writing. In the meantime, the burning of fossil fuels and the large scale deforestation have contributed over 555 $\pm$ 85 GtC (2011 total) to the atmosphere, known as anthropogenic carbon or anthropogenic CO_2 (Ciais et al., 2013). The difference between the amount of carbon emitted and the atmospheric accumulation indicates that about half of emitted carbon has been absorbed by the ocean and land biosphere, the natural carbon sinks. This is an important effect, as excess CO_2 in the atmosphere leads to global

warming and significant climate changes may have significant negative impacts on human and ecological well-being. The natural sinks of anthropogenic CO_2 act to reduce atmospheric CO_2 and buffer potential warming.

On the longest timescales, it will take millennia for the natural system to fully resorb anthropogenic CO_2. The longest timescales of removal are limited by the rate of silicate weathering on land and buffering by carbonate on the sea floor (Archer et al., 2009), which are long geological processes. This thesis is more concerned with the redistribution of anthropogenic CO_2, and potential disruption of the preindustrial CO_2 balance, that will occur over the coming decades and centuries and how these may be affected by changes in the climate and biogeochemisty brought on by excess atmospheric CO_2 (Joos et al., 2013). These are the timescales over which humanity will face the impacts of a changing climate and may aim to adjust its behavior to slow or halt CO_2 emissions in order to stabilize atmospheric CO_2.

I am particularly interested in using models of varying complexity to understand and interpret the variability and trends that are observed in observations and the potential for earth system monitoring to help us understand them. For example, detailed statistical analyses of the recent trends in the growth rate of atmospheric CO_2 and emissions rates indicate that the combined land-ocean sink of CO_2 has grown from 2.4 ± 0.8 PgC yr^{-1} in 1960 to 5.0 ± 0.9 PgC yr^{-1} in 2010 (Ballantyne et al., 2012). Partitioning this growth into oceanic and land fractions will be a helpful step in identifying the relative importance of the ocean and land sinks over the past few decades. Physical and biological understanding of those individual trends may help us to understand how the sinks will behave in the future.

A significant portion of the thesis is also devoted to my attempt to understand how uncertainties in future carbon uptake affect the ability to make efficient policy to reduce emissions of atmospheric CO_2. This question has been asked before, particularly in terms of the level of emissions that would be necessary to stabilize

atmospheric CO_2 along certain pathways (Sarmiento et al., 1995). Building on these previous efforts, I adopt an integrated assessment model from the climate economics literature to try to understand the future economic costs associated with uncertainty in CO_2 uptake.

For the quickly browsing reader, this thesis presents work which attempts to directly or indirectly address three basic questions:

1. Are there multi-decadal trends in the uptake of anthropogenic CO_2 in response to climate variability or change?

2. If a change to the carbon sinks is predicted by a model or process-based hypothesis, will we be able to detect it and when?

3. If we do confidently identify a feedback mechanism in the global carbon cycle, what implications does that have for climate policy?

For the first question, I investigate the recent trends in sea-air CO_2 flux using a new data-based history of surface ocean pCO_2 and statistical methods for identifying trends. For the second, I consider model projections of the effect of climate change on the Southern Ocean CO_2 uptake in the 21st century. For the third, I investigate the implications of uncertainty in carbon cycle projections for climate policy and simulate learning as a significant reduction in the uncertainty surrounding the CO_2 fertilization of the land carbon sink.

1.1 Role of the Ocean

Concerted community efforts have been devoted to producing an authoritative climatology of present-day air-sea CO_2 fluxes, based on databases of surface pCO_2 observations (Takahashi et al., 2009a). However, identifying multi-decadal trends in CO_2 fluxes from observations has proven to be more challenging (Doney et al., 2009). The

available surface pCO_2 estimates are too sparse to separate long-term trends from decadal and seasonal variability using simple analysis on the global scale. However, model studies of the ocean flux forced by known atmospheric conditions indicate that the ocean uptake of CO_2 may have decreased since the 1960s, relative to the growth that would be expected, because of the impacts of climate change on ocean circulation (Sarmiento et al., 2010).

In chapter 2, I introduce Markov Chain Monte Carlo sampling as a novel technique for estimating the historical pCO_2 at the ocean surface. The result is a plausible history of surface pCO_2 based on available measurements and variability inferred from model simulations. From the surface ocean pCO_2 history, I can examine trends in the oceanic uptake of anthropogenic CO_2. This was one of a few co-incident studies that looked at constraining multi-decadal trends in ocean CO_2 uptake from observations.

Applying the method to a modern database of pCO_2 data, I find that two thirds of the ocean surface is trending toward increasing uptake of CO_2, with a mean (year 2000) uptake of 2.3 ± 0.5 PgC yr^{-1} of anthropogenic carbon and an increase in the global annual uptake over the 30-year time period of 0.4 ± 0.1 PgC yr^{-1} $decade^{-1}$. This estimate relates well to other global estimates of the mean CO_2 uptake, but provides a globally consistent analysis with regional details.

The results are particularly interesting in the Southern Ocean, where we find increasing uptake of carbon over 1980-2009. This result is seemingly in contrast to previous studies (Le Quéré et al., 2007). By a linearization of the surface carbonate system, I find evidence for increased ventilation of deep ocean carbon, in response to increased winds, which would be consistent with others (Lenton et al., 2012). However, I show that this increase in carbon content is more than offset by an associated surface cooling such that the CO_2 flux with the atmosphere grows consistently from 1980-2009.

1.1.1 Southern Ocean Observations

Building off of the Southern Ocean results in chapter 2, I review current estimates of the CO_2 uptake in the Southern Ocean and projections of its response to climate change in chapter 3. I show how the Southern Ocean is critically important to the oceanic uptake of anthropogenic CO_2, yet it is also the source of the most uncertainty in estimates of uptake because of poor data coverage and an incomplete understanding of the processes that govern CO_2 uptake in the region. The uncertainty in the future evolution of the Southern Ocean uptake is subject to the same uncertainties.

I discuss how the uncertainty in Southern Ocean uptake is true for both empirical and model-based estimates, where empirical estimates are limited by the lack of available data in the Southern Ocean and model estimates show significant differences across models at the process level. I then argue that increased observational density is necessary to resolve the uncertainty in the Southern Ocean CO_2 uptake and the process-level understanding of the dynamics which govern the Southern Ocean CO_2 flux.

I then perform an observational system simulation experiment where I try to reconstruct the output of an earth system model using a simulated network of float-based biogeochemical samplers. Such a network will likely provide a significant opportunity to improve both our estimates of the oceanic CO_2 flux, resolve discrepancies between different methods and provide resolution to what physical and biogeochemical processes control trends in Southern Ocean CO_2 uptake.

An observation system with 100-200 floats deployed in the Southern Ocean would increase the precision of the month-to-month estimate of CO_2 uptake to 0.1 GtC yr^{-1}, or a significant reduction of the present uncertainty in multi-source estimates. It would additionally provide an opportunity to accurately measure the seasonal cycle. The results of the sampling will be a significant improvement over a range of sampling densities.

1.2 Land-Biosphere and Climate Policy

The implications of the natural sinks of CO_2 for public policy and the global climate are commonly cited as a motivating factor in studies of the present-day carbon cycle. Given the potential for significant changes to the climate from increased CO_2 emissions and the potentially negative impacts on human and ecological well-being that could result from warming, this is not a surprising incentive for undertaking research into the mechanisms that govern CO_2 uptake. I am particularly interested in the potential benefit of resolving uncertainties or detecting feedbacks with climate in CO_2 uptake for the purpose of making efficient climate policies.

In chapter 4, I attempt to address how uncertainty in the future strength of the natural CO_2 sinks affects assessments of the economic effects of climate change and the potential for making efficient policy to reduce emissions and prevent future damages. The uncertainty in the carbon cycle is explored using a simple model of anthropogenic CO_2 uptake constrained by currently available observations, including those described in section 1.1. After constraint, I use the simple model to develop probabilistic projections of the atmosphere-ocean-land CO_2 balance for various pathways of future CO_2 emissions.

I find that the parameterization of the uncertain carbon model is sensitive to the assumed historical emissions from land use change. The emissions from historical land use change are subject to the largest uncertainty in the historical carbon budget (Le Quéré et al., 2013). Given that the oceanic and atmospheric stocks of anthropogenic CO_2 are fairly well known, the imbalance between them is attributed to a 'missing sink', possibly the terrestrial biosphere. Any uncertainty in land use change emissions projects into uncertainty in the net uptake of CO_2 by the land biosphere. What drives this missing sink seems to be a great mystery within the carbon cycle research community. It is hard to balance the global carbon budget without invoking significant increases in net primary production and carbon storage in the

land biosphere (Shevliakova et al., 2013). Yet, observations which confirm that CO_2 fertilization actually contributes to long-term storage of anthropogenic CO_2 at the forest or ecosystem level are not certain, because of the long timescales necessary for direct observation and limited testing in tropical forests and at high-latitudes (Norby and Zak, 2011; Luo et al., 2011). To address this uncertainty, I implement two plausible histories of CO_2 emissions from land use change when parameterizing the data-constrained model. I then compare the outcomes of these two parameterizations in terms of future atmospheric CO_2 and temperature increases under emissions scenarios.

I then use an integrated assessment model to show that resolving the difference would allow for more efficient emissions mitigation policy. The value of additional information increases for policies built for high expected damages, low discounting rate and a warming threshold. This study provides a blueprint for future studies into evaluating the economic benefits of learning about feedbacks and uncertainties in the global carbon cycle.

1.3 Publication, Coauthorship and Funding Sources

Outside of the abstract and introduction, this thesis is written in the first person plural. This reflects that much of the presented work has been written with multiple authors as articles for publication. In each case, I performed all of the original research tasks, including conceiving of the individual experiments, performing calculations and writing the results. The coauthors assisted in the conception of the studies, interpretation of the results and editing of the written presentation. The ocean flux history documented in chapter 2 was published in an article in *Global Biogeochemical Cycles* with coauthors Jorge Sarmiento and Keith Rodgers (Majkut et al., 2014a). The review of Southern Ocean CO_2 modeling and observation system simulation

experiment in chapter 3 was done with a larger group of collaborators, additionally including Brendan Carter, Thomas Frölicher, Carolina Dufour. It was published in a special issue of *Philosophical Transactions of the Royal Society - Series A*, focused on the physics and biogeochemistry of the Southern Ocean (Majkut et al., 2014b). At the time of writing, the work presented in chapter 4 is being prepared for submission as an article in collaboration with Robert Kopp, Michael Oppenheimer and Jorge Sarmiento.

I have been supported by the National Oceanographic and Atmospheric Administration (NOAA-NA11OAR4310066); the Princeton Environmental Institute Science, Technology and Environmental Policy Fellowship; the Princeton Carbon Mitigation Initiative; and the Cooperative Institute for Climate Sciences.

Chapter 2

Ocean Flux History

2.1 Introduction

The flux of CO_2 at the air-sea interface controls atmospheric CO_2 concentrations on centennial timescales and is an important term in the year-to-year carbon budget of the atmosphere. Currently, the ocean absorbs CO_2 from the atmosphere. Each year the uptake is equivalent to about 30% of annual fossil fuel emissions (Sarmiento et al., 2010). The flux amounted to 2.0 ± 1.0 PgC yr^{-1} in the decade surrounding the year 2000, according to multiple estimation techniques based on observations of surface ocean carbon (Takahashi et al., 2009a; Wanninkhof et al., 2013), though estimates that infer ocean circulation from models result in smaller uncertainties, 2.0 ± 0.6 PgC yr^{-1} (Gruber et al., 2009).

Recent analysis of the atmospheric carbon content has shown that the combined land-ocean sink of CO_2 from the atmosphere has grown from 2.4 ± 0.8 PgC yr^{-1} in 1960 to 5.0 ± 0.9 PgC yr^{-1} in 2010 (Ballantyne et al., 2012). Partitioning the growth in the carbon sink into terrestrial and oceanic components will be helpful in developing an understanding of the dynamics that lead to trends in the land and ocean sinks and how they affect the response of the climate system to anthropogenic

forcing through carbon cycle feedbacks (Friedlingstein et al., 2006). In the future, if we wish to have a system that monitors the carbon budget between the atmosphere, terrestrial biosphere and ocean, having an updating estimate of the air-sea flux and an understanding of its trends will be essential.

Studies of the trends in the oceanic uptake of CO_2 largely hinge on surface measurements of pCO_2. Since the air-sea CO_2 flux is based on the disequilibrium in the partial pressure of the gas, pCO_2, a common metric of the flux trend is the rate of change of pCO_2 in the sea surface compared to the atmospheric pCO_2 growth rate. However, the scarcity of direct measurements makes it difficult to directly examine local trends in the air-sea CO_2 flux (Doney et al., 2009) and estimates of the trend in the global flux vary significantly across methodologies (Wanninkhof et al., 2013).

Regional trends in surface pCO_2 are somewhat tractable. Fay and McKinley (2013) calculated trends in surface pCO_2, globally but divided into ocean 'biomes', areas of similar biogeochemical and physical taxonomy, and showed that trends in pCO_2 from the surface measurements are strongly influenced by subsampling of decadal variability. Correcting for the subsampling, they showed that the multi-decadal trend in surface pCO_2 for the tropics and subtropics is consistent with or slightly slower than the atmospheric growth rate, indicating a growing ocean uptake flux. Likewise, time series at two of the most highly sampled oceanic regions, from the ocean stations BATS (Bermuda Atlantic Time series Study) and HOT (Hawaii Ocean Time Series), also show that the surface ocean pCO_2 growth rate is similar to the atmospheric growth rate (Bates, 2007; Dore et al., 2009).

Surface pCO_2 data in other regions can indicate significant differences from the atmospheric growth rate across several decades. In the Subtropical North Pacific, the surface pCO_2 has grown slower than the atmospheric partial pressure (Takahashi et al., 2006), implying an increasing uptake flux. In the the North Atlantic, surface pCO_2 trends imply a decreasing air-sea flux between 1994-1995 and 2002-2004 (Schus-

ter and Watson, 2007). In the Equatorial Pacific, surface pCO_2 data show that the degassing flux from the Equatorial Pacific increased in the mid-1990s, concurrent with the shift in the Pacific Decadal Oscillation [PDO] in 1997 (Feely et al., 2006). In the Southern Ocean, winter pCO_2 was increasing faster than the atmospheric value from 1981-2007 (Le Quéré et al., 2010). The trends that are implied by these local studies might point to substantial changes in the oceanic CO_2 uptake and it is important to understand how the global trend emerges from the regional trends.

Takahashi et al. (2009a) have collected a substantial set of surface pCO_2 measurements and used them to build an authoritative atlas of the annual cycle of pCO_2 in the surface ocean and implied climatology of air-sea CO_2 flux. The observations that were used to make the climatology, mostly underway measurements of pCO_2 from research cruises and volunteer ships of opportunity, have been released as a database, LDEO2010, for public download (Takahashi et al., 2009b). More recently, the efforts of Pfeil et al. (2012) and Sabine et al. (2012) have resulted in the SOCAT database and gridded products, a quality controlled and publicly documented collection of surface pCO_2 measurements. These initiatives allow for the continued use of surface measurements as a source of information about the surface ocean carbon system. For us, the availability of these data provides an opportunity for a global analysis of trends in the sea surface pCO_2 and the air-sea CO_2 flux over the past few decades.

Despite the size of the LDEO2010 database, the available surface pCO_2 measurements are sparse. The associated climatology of the sea-air flux is reported on a grid of 5° (longitude) x 4° (latitude) boxes (Takahashi et al., 2009a). The observations cover less than 5% of the values needed if one wishes to have a pCO_2 history on that grid with monthly values from 1980 to 2005. Data availability is highest in the North Atlantic and North Pacific. Large parts of the Southern Hemisphere, tropics and sub-tropics are sampled with a seasonal bias, once or twice or not at all. The small number of available measurements over the whole globe makes it difficult to separate

trends from interannual variability, the seasonal cycle and transient variations in each region of the ocean.

We introduce the Markov-Chain Monte Carlo, MCMC, method in the methods section below. We then demonstrate the MCMC method on a synthetic dataset and finally use it to estimate pCO_2 timeseries and trends using data from the LDEO2010 database. The results section shows the estimated trends, sensitivity to the representation of seasonal and interannual variability and the fluxes that result from the pCO_2 timeseries associated with our inversions. Lastly, we discuss the implications of the inversion for the ocean carbon sink and the global carbon cycle.

2.2 Methods

Here we describe the formulation of the simple model we use for the surface pCO_2 and the Markov Chain Monte Carlo inversion technique. Then we discuss how we implement the two using the LDEO2010 data. The MCMC inversion is a Bayesian technique and requires us to impose an *a priori* distribution for the parameters in the pCO_2 model. The a priori distribution represents our best knowledge about the model before it is inverted with data. In this section, we describe how we estimate the prior distribution for the pCO_2 model from a selection of ocean general circulation model simulations with biogeochemistry, which are described in table A.1.

Briefly, the MOM4p1-BLING model we used for prior information is based on the NOAA GFDL Modular Ocean Model version 4.1 (Griffies et al., 2004) with 3° horizontal resolution. The circulation model is coupled to the BLING idealized biogeochemistry model (Galbraith et al., 2011). This model configuration was included in several variations, with simulations forced by different reanalysis products: CORE-II (Large and Yeager, 2009), ERA-40 (Uppala et al., 2005) and NCEP1 (Kalnay et al., 1996) and a simulation forced with a climatology derived from CORE-II. Addition-

ally, we used two simulations from the latest versions of the NEMO-PISCES model (Aumont and Bopp, 2006), using the ORCA2 configuration of NEMO Version 3.2, with 2 degree horizontal resolution and 31 vertical levels. This model was forced with the DRAKKAR Forcing Set 4.1, or DFS4.1 (Brodeau et al., 2010).

2.2.1 Estimating pCO_2 time series

We implement and perform inversion of a simple model for the surface water pCO_2, shown in equation 2.1, which has terms for four modes of variability with monthly resolution:

$$\begin{aligned} pCO_2^{\text{sea}}(x,y,t) &= A(x,y)\cdot t + B(x,y) \\ &\quad + C(x,y)\cdot SEAS(x,y,T) + D(x,y)\cdot IAV(x,y,t) \end{aligned} \quad (2.1)$$

The coefficient of the first term, A in μatm yr^{-1}, is meant to represent the multi-decadal linear trend with time. We generally expect A to have a positive value, as a warming ocean that is also absorbing anthropogenic CO_2 from the atmosphere should exhibit increasing pCO_2. B gives the June 1995 value for pCO_2 in μatm; t is referenced to that month. The constant term allows for regional differences in the mean carbon content of the surface ocean. The seasonal and interannual variability about that linear model are represented by the remaining two terms. In this case, we consider seasonal variations to be a climatological repeating cycle, $SEAS$ in μatm, based on the average annual cycle for a grid box. The time dependence of this term is climatological and thus it depends on the repeating monthly time grid, T. The monthly value of SEAS is calculated as the average deviation from the linear trend for each month, from 1980-2006. The interannual term, IAV μatm, represents mean year-to-year variability, such as decadal trends, and interannual variability at monthly timescales, such as an early spring bloom or the increasing seasonality in pCO_2. Both

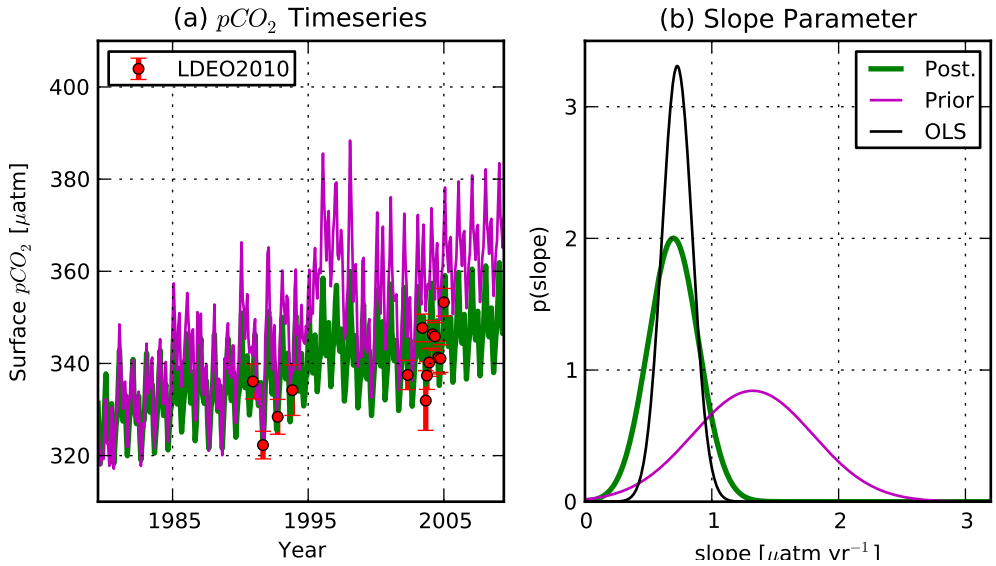

Figure 2.1: These figures show (a) pCO_2 time series and (b) the distributions associated with the parameter A for a grid cell in the Eastern Pacific. The green line shows the posterior estimate for the pCO_2 time series and the magenta shows the prior estimate. The red dots indicate the monthly-averaged measurements from LDEO2010.

the seasonal and interannual terms have zero averages over the whole time period. Thus, the trend parameter, A, should fully represent the changes in surface pCO_2 over the 30 year window. Figure 2.1(a) shows how the model represents the surface pCO_2 data in the Eastern Pacific 5x4 degree box centered at (132.5W,16N), with different coefficients from before and after inversion.

Previous attempts to estimate pCO_2 as a function of time have generally been limited to a simple linear function including the $A(x,y) \cdot t$ and $B(x,y)$ terms and some representation of the seasonal cycle, our $C(x,y) \cdot SEAS(x,y,T)$, (Takahashi et al., 2009a); and using ordinary least squares to estimate the model parameters. Our contribution is to add the interannual variability, $D(x,y) \cdot IAV(x,y,t)$ and to implement a Bayesian inversion scheme that allows us to include prior estimates as constraints on the model parameters.

2.2.2 MCMC Inversion

The inversion scheme we implement is a version of Markov Chain Monte Carlo sampling. Each of the parameters (A, B, C, D) in equation 2.1 is subject to Bayesian inversion using the observations in LDEO2010 and the pCO_2 values predicted by the simple model. The prior distribution for the parameters (A, B, C, D) is updated with the available observations to yield posterior distributions for each of the parameters. Thus, the inversion can change the probability distributions governing the trend, initial value and the amplitude of the prescribed seasonal and interannual variability. In this implementation it cannot change the phase of the seasonal cycle or modify the model-based estimate of a singular event such as a particular El Niño.

The MCMC performs an iterative random walk of the parameter space of the pCO_2 model to arrive at an optimal parameter estimate given the prior information and available data. Given a seed vector x_n in parameter space (A, B, C, D), the MCMC algorithm randomly selects a nearby point as a proposed step, x_{n+1}, and uses a specific decision criterion to accept or reject that next step based on the misfit of the observations and model predictions and the prior probability assigned to that point in parameter space. If the proposed step is accepted, then the walk moves to that position and starts again, otherwise it starts again from the current position. Under this decision criterion, the set of positions occupied during the random walk converge to a sampling of the posterior distribution of the parameters given the observations (Hastings, 1970).

Our implementation of the MCMC uses the Metropolis-Hastings decision criterion. The proposed step is approved with probability, α, determined by

$$\alpha = \min[1, \frac{p(x_{n+1})L(M|x_{n+1})}{p(x_n)L(M|x_n)}]. \tag{2.2}$$

In equation 2.2, $p(x)$ is the prior probability of the point x in parameter space. $L(M|x)$ is the likelihood function for the parameter given the data available. The likelihood is the probability of obtaining the pCO_2 measurements M from LDEO2010, in the case that the true parameters of the model are located at x. If the misfit between the modeled pCO_2 at the parameter values in x is larger than the error associated with the measurements, then the likelihood will be low at that point. The likelihood calculation requires the error covariance matrix for the observations M and M varies in size depending on how many observations are available in each grid box of the inversion.

Under the probabilistic metropolis rule, the random walk will tend to move toward areas of parameter space where both the prior probability and the model likelihood are high and thus a good fit of the data. That tendency generates the sampling of the posterior distribution. Figure 2.1(b) demonstrates how inversion with the data in LDEO changes the model-based prior distribution for the slope parameter A. The MCMC inversion both changes the mean and the standard deviation of the parameter's distribution, indicating that the data has substantial information about this parameter in that region.

2.2.3 Calculating Fluxes from pCO_2

The air-sea flux of CO_2 is a function of the difference in pCO_2 between the two media, ΔpCO_2, and an exchange velocity, k_w.

$$\Phi = k_w \Delta pCO_2 \tag{2.3}$$

The gas exchange velocity is calculated as a function of the squared windspeed at 10 meters above sea level, the solubility of CO_2 in seawater, α, and the local Schmidt

number, Sc (Wanninkhof et al., 2009).

$$k_w = \gamma \cdot \alpha \cdot \left(\frac{Sc}{600}\right)^{-0.5} \cdot U_{10}^2 \tag{2.4}$$

The value of γ in these calculations is 0.27 (Sweeney et al., 2007). In the year 2000, we use the gas exchange piston velocity from (Takahashi et al., 2009a) so that the fluxes are directly comparable to those from the climatology. We then diagnose the time variation in k_w from the reanalysis forced simulation with MOM4p1-BLING.

In this work, we define ΔpCO_2 to be positive for excess pCO_2 in the ocean relative to the atmosphere, such that a positive flux is out of the ocean and a negative flux is into the ocean.

$$\Delta pCO_2 = pCO_2^{\text{sea}} - pCO_2^{\text{air}} \tag{2.5}$$

We use the atmospheric mixing ratio of CO_2 from the global monitoring stations at Mauna Loa and the South Pole, assigning the Muana Loa value north of Hawaii and linearly interpolating between Hawaii and the South pole for the rest of the globe (Keeling et al., 2001). This was the same atmospheric pCO_2 that was used to force the MOM4p1-BLING model simulations. The difference between fluxes calculated with this atmospheric pCO_2 and the atmospheric pCO_2 from (Takahashi et al., 2009a) in the year 2000 are negligible. We also use local sea level pressure to calculate the atmospheric pCO_2 at the sea surface. We assume that the atmospheric CO_2 is zonally homogeneous. Thus, the estimates of the air-sea carbon flux can follow directly from estimates of the surface water pCO_2. Likewise, trends in the air sea carbon flux can be related to the relative trends in pCO_2 in the sea surface and lower atmosphere. We assume a preindustrial air-sea CO_2 flux of 0.4 ± 0.2 PgC yr^{-1} out of the ocean when calculating the global anthropogenic CO_2 uptake as in (Takahashi et al., 2009a).

2.2.4 Defining Inversion Parameters

Each of the parameters (A, B, C, D) in the pCO_2 model in equation 2.1 needs to be supplied with a prior distribution. We assume that the parameters are independent and normally distributed when assigning the prior. For the trend and intercept (A, B), we generate the prior mean and standard deviation using an ensemble of 6 ocean general circulation model simulations that were coupled with biogeochemistry. The physical circulation of the individual models was forced with atmospheric reanalysis products and the ocean-biogeochemistry models were forced with atmospheric CO_2 concentrations. We use the models as different representations of how the ocean biogeochemistry would be expected to respond to the increasing atmospheric concentrations of CO_2 and the climate experienced over 1980-2006. Each of the models was spun-up from pre-industrial conditions with the historical atmospheric CO_2 and forced by a climatological year (monthly averaged values from 1959-1979 with imposed 6-hourly variability) of the atmospheric forcing until the start of the atmospheric reanalysis time period in the 1950s.

We used ordinary least squares to calculate the linear slope and mean value for each model's time series of pCO_2 in the 5x4 degree grid boxes and then calculated the ensemble mean and standard deviation for both parameters to form the prior distributions. The number of samples in this case is small and the sample standard deviation that results is not robust. Thus, we increased the standard deviation of the ensemble by a factor of 3 to define the prior standard deviation of A. This is consistent with setting the standard deviation at the upper range of the confidence interval for the true standard deviation between the 90 and 95% levels. The prior standard deviation for the geographical mean, B, is assumed to be the sample standard deviation from the ensemble. The construction of the SEAS and IAV signals is described in the next paragraphs.

The seasonal variability can be diagnosed from observations for some areas (Takahashi et al., 2009a), but sampling scarcity makes it hard to do so for the global ocean. The seasonal cycle can also be estimated with harmonic functions for boxes of a few degrees (Schuster and Watson, 2007) or basin-scale regions (Fay and McKinley, 2013), but data scarcity is again a problem. Coupled ocean-ecosystem models are attractive because they offer pCO_2 time series without gaps, but the modeled seasonal cycle can be biased (Woloszyn et al., 2011). In our inversion, we use the seasonal cycle from the MOM4.1-BLING simulation and the (Takahashi et al., 2009a) seasonal cycle and compare the results between the two inversions to examine the sensitivity to the imposed seasonal cycle. The modeled seasonal cycle is defined for each month, is set to be a climatology of deviations from the annual mean and is a repeating cycle for the 30 year time period. Likewise, the climatological seasonal cycle based on observations has no variation between years, but it is constructed from interpolated observations from the LDEO2010 database.

In this work, the interannual variability was taken from the MOM4.1-BLING simulations under CORE-II forcing. The CORE-II forced simulation was chosen for the IAV term because of the improved representation of the wind forcing fields in the Southern Ocean and Equatorial Pacific (Large and Yeager, 2009). The interannual term, IAV(x,y,t), is defined for each month as the difference between the MOM4.1-BLING pCO_2 and the ordinary least squares linear fit against the model plus the repeating seasonal cycle from the model. We chose to use the interannual variabilty from the reanalysis forced model because the signals would be 'time-stamped' in the same way as the data in LDEO2010. If the data shows a strong response to the El Niño in 1997-1998, for instance, that response should be adjusted for using the modeled response from the MOM4p1-BLING simulation as the surface forcing reflects the conditions at that time. Since the CORE-II forcing product ends in 2005,

interannual variability after that year is set to zero. The effect of introducing the IAV term from the forced-model simulations is examined in the sensitivity analysis.

The imposed seasonal cycle and interannual variability might be inconsistent with the observations of surface pCO_2 and thus introduce additional bias. Our framework allows for the scaling parameter for each, (C, D) in equation 2.1, to be subject to inversion. In this framework, the imposed signals can be muted or amplified to provide a better fit to the observations. For the prior of the amplitude parameters (C, D), we assume a normal distribution with mean of 1.0 and standard deviation 1.0. This prior was assigned for all grid cells and both time series and assumes a high uncertainty in the imposed signals.

To calculate the likelihood, $L(M|x)$, it is necessary to have an error covariance matrix for the observations in LDEO2010. In this application, the data vector, M, is the array of all of the monthly-averaged pCO_2 measurements from LDEO2010 for each cell. We assume that the errors are unbiased, independent and normally distributed. The standard deviation of the individual distributions is set equal to the monthly sample standard deviation in each grid cell. In cases where the standard deviation is undefined or very small, we set a floor for the error at the instrumental precision of 3.0 μatm (Takahashi et al., 2009a).

2.2.5 Demonstration Study

In this section we use an Observing System Simulation Experiment (OSSE) to demonstrate the benefits of the MCMC method and the importance of including the IAV term for properly calculating to pCO_2 trend. We choose output from the NOAA GFDL ESM2M historical simulation for CMIP5 (Dunne et al., 2012, 2013) for the 'true' pCO_2. Then, the space-time coordinates of the observations in LDEO2010 are used to sample the ESM2M and to infer trends from this subsampling of the model. We add an unbiased normally distributed error term to each synthetic observation

with the same standard deviation that we assign to the measurements in the data-based inversion. The MCMC is initialized with a prior based on an ensemble of 5 CMIP5 historical simulations (for a description see table A.2). The prior was constructed in the same way as the prior for the LDEO2010 inversion, with the climate models in place of the reanalysis forced models. The trends inferred from ordinary least squares and the MCMC inversion applied to this synthetic data base are then compared with the full trend explicitly resolved by ESM2M.

To illustrate the importance of representing the interannual variability for capturing the true slope, we separate the slope calculation into different components. We find A and B by fitting:

$$pCO_2(x,y,t)_{\text{full}} = A_{\text{full}}(x,y) \cdot t + B_{\text{full}}(x,y) \tag{2.6}$$

where A_{full} and B_{full} are the 'true' value for the parameters obtained from the fully sampled model output. We then define the signals SEAS and IAV from the residuals of that fit:

$$pCO_2(x,y,t)_{\text{full}} - \left[A_{\text{full}}(x,y) \cdot t + B_{\text{full}}(x,y))\right] = SEAS(x,y,T) + IAV(x,y,t). \tag{2.7}$$

We now subsample the model output at the LDEO2010 points, correcting for SEAS but not IAV,

$$pCO_2(x,y,t)_{\text{ldeo}} - SEAS(x,y,T) \sim A_{\text{sub}}(x,y,t) \cdot t + B_{\text{sub}}(x,y), \tag{2.8}$$

such that there is potentially a bias imposed by not correcting for the subsampling of the IAV signal. Correcting for that bias is one of the novelties of this work. Since the model output has full resolution, we can directly estimate the bias that results

by fitting a linear model to the subsampled interannual variability,

$$IAV(x,y,t)_{\text{ldeo}} \sim A_{\text{iav}}(x,y,t) \cdot t + B_{\text{iav}}(x,y). \tag{2.9}$$

Figure 2.2(a) shows the fully sampled model trend A_{full} and figure 2.2(c) shows the least squares fit to the seasonally-adjusted synthetic dataset, A_{sub}. The A_{sub} estimates vary significantly from cell to cell and are not representative of the 'true' value from the climate model simulation. Figure 2.2(e) shows the effect of the undersampling of the interannual variability on the least-squares trend estimation, A_{iav}. This is the level by which the trend estimates in figure 2.2(c) are biased by undersampling. Figure 2.2(f) shows that when the bias term is removed, $A_{\text{sub}} - A_{\text{iav}}$, then the true pCO_2 evolution is nearly achieved for the whole globe.

The trend estimates from the MCMC inversion of the synthetic data, A_{mcmc}, are shown in figure 2.2(b), where they compare favorably to the true slope exhibited by ESM2M. After updating with the synthetic database, using the same sampling as described in the Methods and Results sections, the MCMC technique reduces the root mean squared error [RMSE] of the trend estimates by 95% compared to the A_{sub} estimates in figure 2.2(c). The majority of that reduction comes from including the interannual variability terms. The differences between the two estimates, A_{sub} and A_{mcmc}, shows that the MCMC inversion is a practical technique for including the interannual variability and avoiding the bias A_{iav} in the final estimates.

The difference between A_{mcmc}, in figure 2.2(b), and the compensated least squares estimate $A_{\text{sub}} - A_{\text{iav}}$, in figure 2.2(f), shows the potential pitfalls of the MCMC method for trend estimation. For example, the prior slope estimate influences the final slope estimate of the MCMC. When the prior and true slopes are aligned the MCMC returns a reasonable slope, as occurs over much of the Southern Hemisphere in this test. When the prior estimate and true slope are not aligned, the MCMC

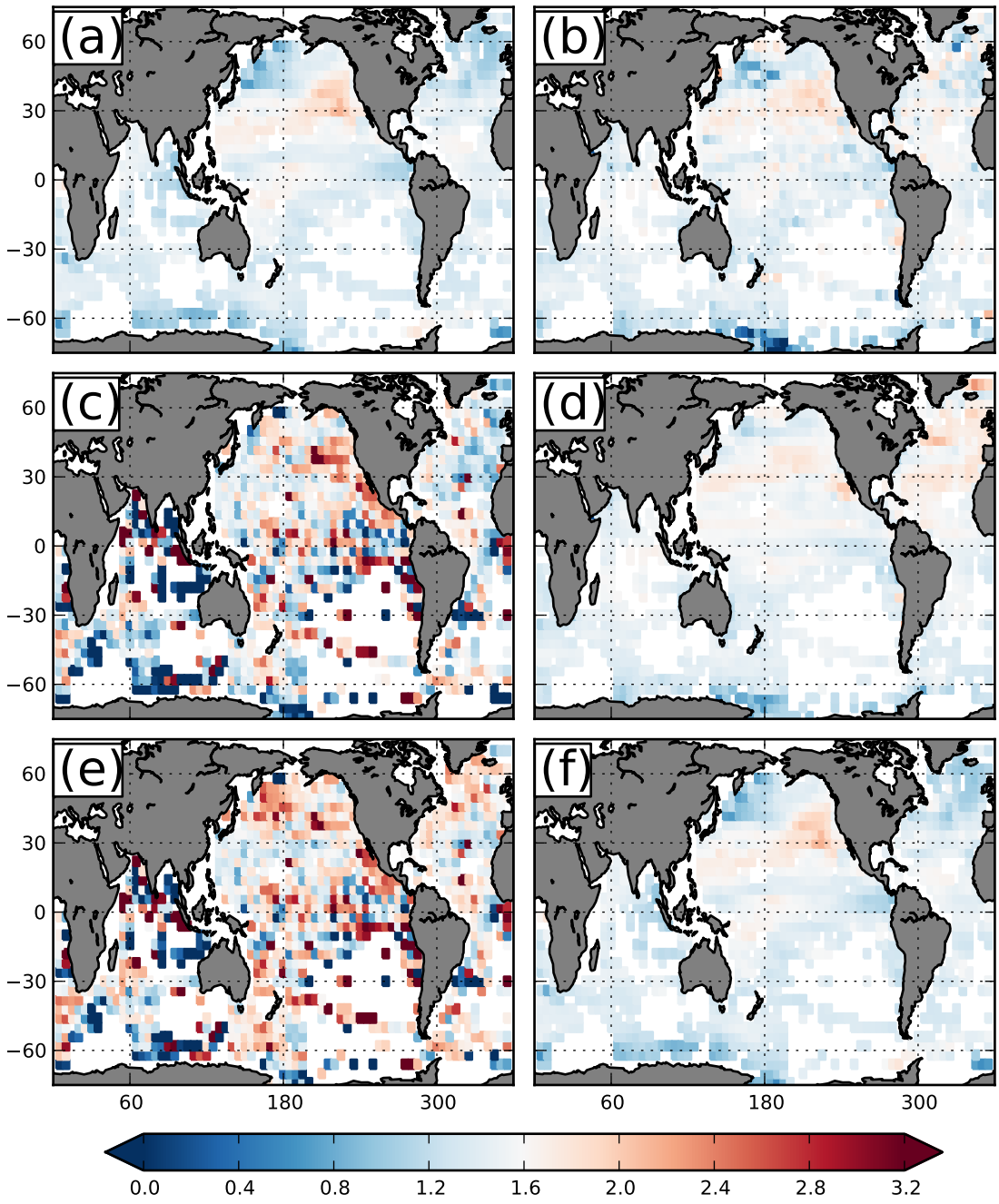

Figure 2.2: This figure shows different pCO_2 slope estimates $\mu atm\ yr^{-1}$ for the GFDL ESM2M verification experiment. The true case, (a), is the slope of the fully-sampled model pCO_2, A_{full}. Panel (b) shows the same slope calculated by MCMC, A_{mcmc}, with the synthetic LDEO2010 measurements. Panel (c) shows the sub-sampled slope A_{sub}, calculated from the synthetic data with ordinary least squares. Panel (d) shows the prior used to initialize the MCMC from (b). Panel (e) shows A_{iav}, the bias in slope that results when subsampling the IAV term. Lastly, panel (f) shows the sum of A_{sub} and A_{iav}.

estimate can only reveal the true slope if the available measurements and imposed variability provide sufficient constraint. In this test case, the mean slope of the prior has a different sign, relative to the atmospheric growth rate, than the true case in substantial areas of the North Pacific and North Atlantic (265 cells). The MCMC inversion with synthetic data decreases these errors by over half (fixing 156 cells), but does not return the correct sign in continuous regions of the Western North Atlantic or Western Subtropical Pacific. Globally however, the MCMC inversion reduces the bias in the prior slope estimate from 0.1 μatm yr^{-1} to 0.04 μatm yr^{-1} and the MCMC-estimated slope distribution captures the true value within the $\pm 2\sigma$ range for 80% of the cells that are updated with data.

The model-based OSSE shows that the sparse nature of the surface pCO_2 data makes local slope estimates sensitive to the effects of subsampling interannual variability. The MCMC inversion is capable of imposing a model-based estimate of the interannual variability and compensating for much of the bias in local slope estimates. However, the MCMC result relies on having a decent prior estimate of the slope parameter and the interannual variability that will be imposed. In this demonstration, the imposed seasonal and interannual variability came from the true modeled case and the prior estimate of slope came from a similar class of models. Thus this demonstration may be advantaged compared to the application of the method to real data, despite the error added to the synthetic observations, and may be thought of as offering a performance ceiling for interpretation of the MCMC results.

2.3 Results

We performed the inversion for the spatial grid used by Takahashi et al. (2009a) to build the pCO_2 climatology. We chose to use the same grid for validation and comparison purposes. For each grid cell, the MCMC was initialized at the prior mean

values for the parameter set (A,B,C,D) and the random walk was iterated for 50,000 steps. We excluded the first 10,000 steps to account for the burn-in of the random walk and allow the MCMC to move away from the prior means. To avoid biasing the samples of the posterior distribution with auto-correlation from the random walk, we use every 10th step in the random walk. This results in 4000 samples of the joint posterior distribution for (A, B, C, D). In this section, we show the resulting posterior distributions for the pCO_2 model parameters and the sensitivity studies to the IAV and SEAS terms.

2.3.1 MCMC output

The global fit of the MCMC pCO_2 estimates to the measurements in LDEO2010 is comparable to what is found with linear regression. The posterior estimate of pCO_2 is shown in appendix A alongside the data from LDEO2010 that was used to invert the model parameters for 4 random grid cells from the following regions: Polar Southern Ocean, Subpolar Southern Ocean, Equatorial Pacific, Subtropical and Subpolar North Pacific and the Subpolar and Subtropical North Atlantic. The global mean residual of the pCO_2 estimates, against the LDEO2010 data, is -0.1 μatm and the root mean squared error is 16.8 μatm. We find that the empirical seasonality fits the observations better than the model-based seasonality and treat the empirical seasonality case as the standard inversion (see section 3.3 below). The results that are reported below are for the MCMC inversion featuring the empirical seasonality and the model-based interannual variability.

The prior and posterior distributions for the pCO_2 model parameters (A, B) are shown in figure 2.3. The slope parameter A undergoes adjustments in many cells throughout the ocean, with particularly large regional changes in the North Pacific, North Atlantic and Equatorial Pacific. These are the same places where the standard deviation of the prior is reduced by the inversion. The distribution of B also under-

goes substantial changes, particularly in the Western Pacific and Subtropical North Atlantic. The uncertainty in the model parameter, B, is reduced throughout much of the ocean where LDEO2010 has observations. The prior and posterior timeseries in figure 2.1(a) show that the MCMC inversion decreases the uncertainty and mean value of A and B in that cell. The slope parameter, A, has a prior mean estimate of 1.3 ± 0.5 μatm yr^{-1} and a posterior mean of 0.7 ± 0.2 μatm yr^{-1} and the intercept parameter B has a prior estimate of 350 ± 6 μatm and a posterior estimate 339 ± 2 μatm. Figure 2.1(b) shows the probability distribution function for the slope parameter A in that cell.

Figure 2.4 shows the posterior distributions of the scaling parameters C and D. The MCMC procedure scales the imposed signals to realize a better fit to the observations. The seasonal scaling, C, is decreased in the Equatorial Pacific and in the Southern Ocean and enhanced in some areas of the North Pacific. The global posterior mean value of C is 0.9 ± 0.5. The IAV term from MOM4p1-BLING is damped by the MCMC sampling though much of the globe. The global posterior mean value of D is 0.6 ± 0.8. The global damping of these two parameters indicates that there is substantial misfit from the data when they are imposed. Figure 2.1(a) provides an example of a region where the posterior seasonal cycle and interannual variability have been decreased such that the residuals from the pCO_2 timeseries is minimized. The posterior estimate for C is 0.8 ± 0.2 and the posterior value for D is 0.3 ± 0.2.

2.3.2 Flux Estimates

The patterns and magnitudes of the time mean fluxes calculated from the MCMC-based pCO_2 timeseries, figure 2.5(a), are comparable to the estimates of (Takahashi et al., 2009a). The difference between the two is shown in figure 2.5(b). The MCMC pCO_2 results in higher ocean uptake of CO_2 in the Subpolar North Atlantic and over much of the Southern Ocean and increased outgassing in the Subpolar North Pacific.

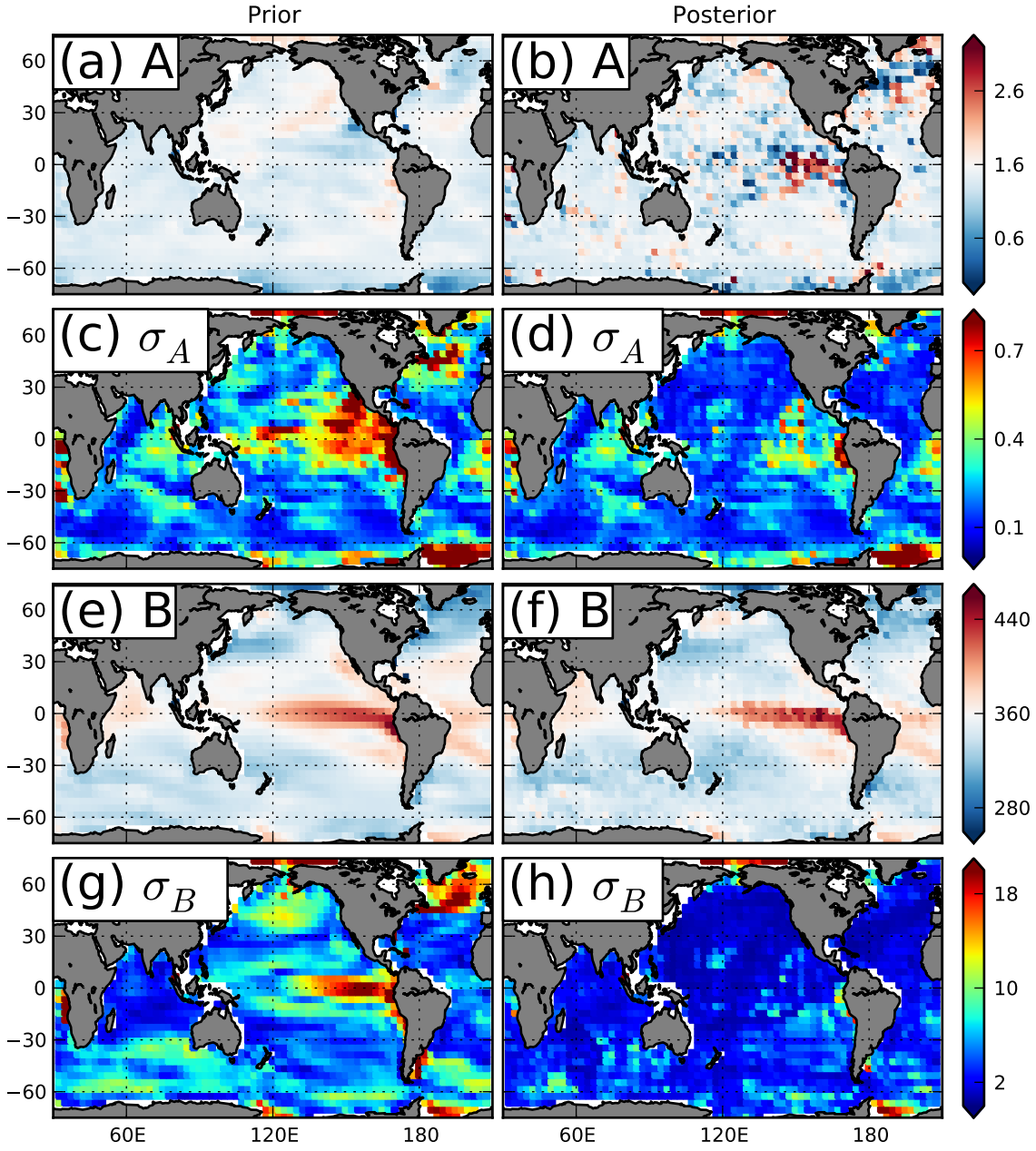

Figure 2.3: The prior and posterior means (a,b) and standard deviations (c&d) for the slope parameter, A, and the intercept term, B, (e,f,g,h) for the MCMC inversion of LDEO2010. The coloring in (a,b) indicates growth with respect to the atmospheric growth rate (blue indicates slower than atmospheric growth) and in (e,f) indicates the 06/1995 value with respect to the atmospheric pCO_2 (blue indicates ocean uptake of CO_2).

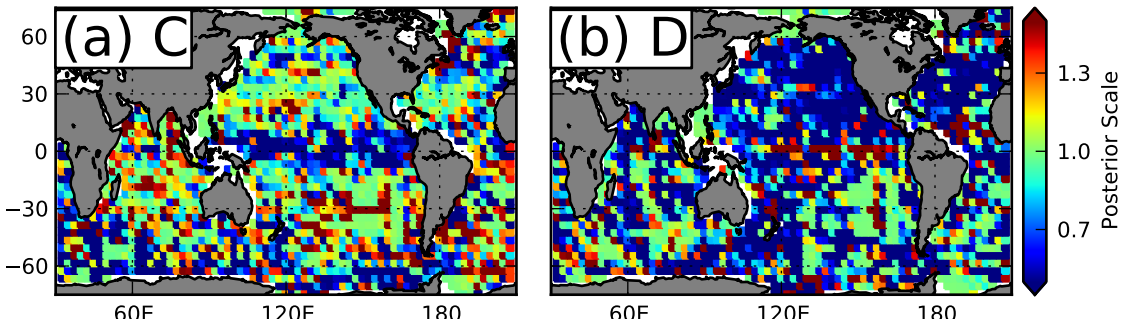

Figure 2.4: The posterior mean estimates for the scaling parameters (a) C and (b) D from the MCMC inversion of LDEO2010. Values smaller than 1 indicate that the amplitude of the imposed variability has been muted by the inversion.

The regional differences in the mean flux of CO_2 integrate to a difference in the global uptake of anthropogenic CO_2, as shown in figure 2.6. This figure shows that in the decade centered on the year 2000, the mean MCMC estimate is higher than that of (Takahashi et al., 2009a) by approximately 0.2 - 0.3 PgC yr^{-1}. This difference is well within the $\pm 1\sigma$ uncertainty estimates from the two products and is principally due to the increased uptake in the Southern Ocean.

The time evolution of the MCMC fluxes is shown in figure 2.6. There, we compare the evolving flux calculated using the MCMC inverted pCO_2 timeseries with a set of other estimates of anthropogenic CO_2 uptake, as compiled by (Gruber et al., 2009). The literature-based estimates of uptake show a generally increasing uptake by the ocean over this time period. Such an increase is consistent with the estimates from the MCMC implementations that make use of the empirical seasonality. The MCMC with interannual variability and empirical seasonality results in a global increase in the CO_2 uptake of 0.4 ± 0.1 PgC yr^{-1} $decade^{-1}$.

2.3.3 Sensitivity Studies

The sensitivity tests, where we exclude the interannual variability term and change the representation of the seasonal cycle, show cell-to-cell and regional differences

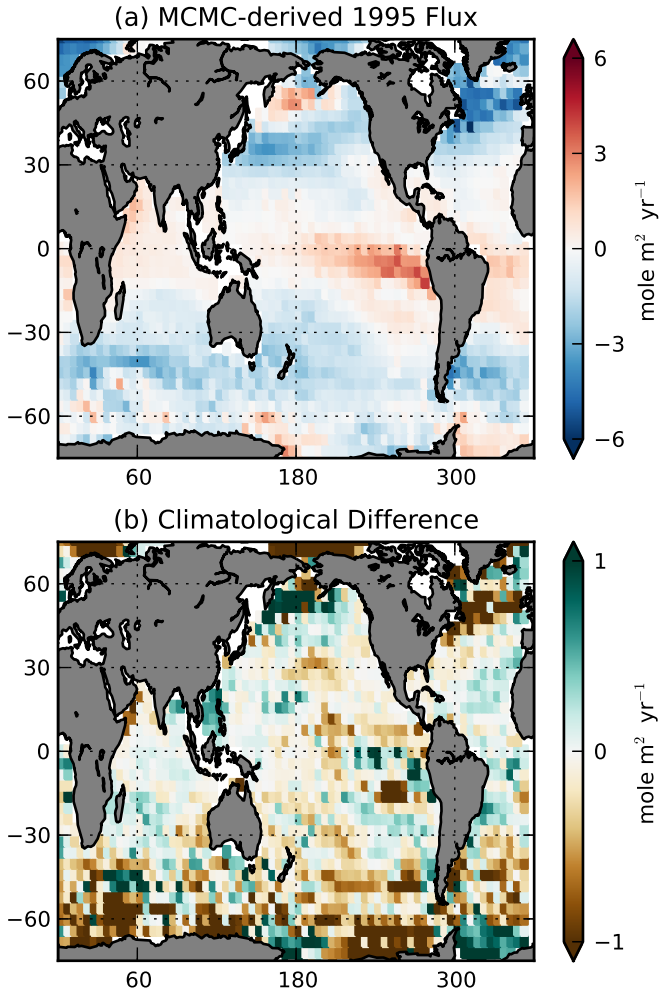

Figure 2.5: The mean flux, 1995-2005, from the MCMC pCO_2 inversion is shown in panel (a). Panel (b) shows the difference between the MCMC-derived flux in (a) and the climatology of (Takahashi et al., 2009a). Positive values mean less uptake in the MCMC-derived estimates.

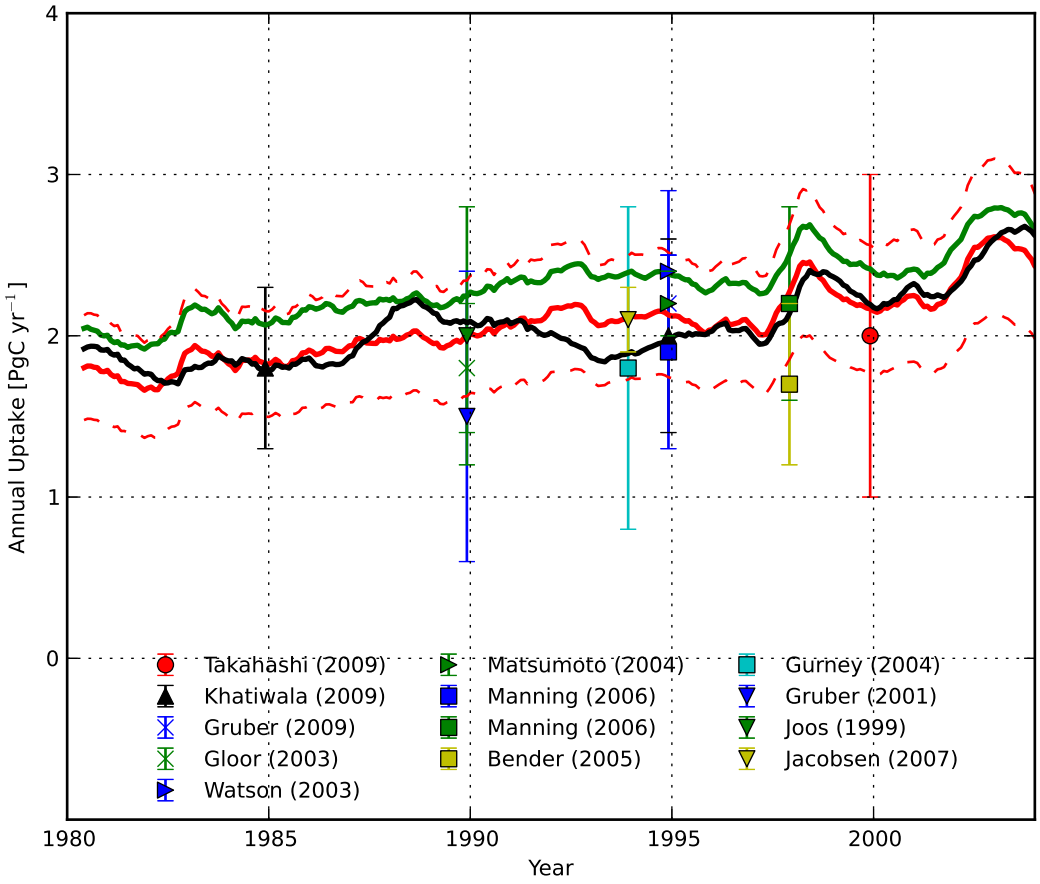

Figure 2.6: The total uptake of anthropogenic CO_2 timeseries, 1980-2009, for the MCMC featuring the MOM4p1-Bling seasonal cycle (green) and the empirical seasonal cycle (red) and the MCMC version with the MOM4p1-Bling seasonal cycle and no interannual variability (black). The dotted lines indicate $\pm$ 1 σ for the global integral, including the uncertainty in gas exchange piston velocity. The red dot and associated error bars represent the anthropogenic uptake calculated by (Takahashi et al., 2009a) of 2.0 $\pm$ 1.0 PgC yr^{-1}. The black triangles show the the decadally-averaged estimates from (Khatiwala et al., 2009). The other box and whisker plots indicate other estimates for anthropogenic CO_2 uptake by the ocean from table 1 in (Gruber et al., 2009).

in both the mean slope estimates and flux estimates but rather small impacts to the global totals. Regional and global breakdowns of the sensitivity for each perturbation for the slope parameter and climatological fluxes are listed fully in the appendix (see tables A.5 and A.6).

The sensitivity case designed to test the impact of including the IAV term on the pCO_2 inversion shows significant regional differences from the standard inversion, where IAV is excluded. Figure 2.7(a) shows the difference in the posterior slope estimate, A, between the standard case and the NOIAV case. We see that adding the interannual variability gives reduced posterior values of A in the Subtropical North Pacific, Western Equatorial Pacific and in the Pacific and Indian sectors of the Southern Ocean. It also gives increasing values of A in the Eastern Equatorial Pacific, the Western Subpolar Atlantic and the Southern Atlantic. The global difference is small, 0.0 ± 0.1 Pg C yr^{-1}, though this is largely a result of compensating changes between regions (c.f. figure 2.7(c)). The global difference in the nominal year 2000 (1995-2005 average) flux is again small, with the IAV term decreasing the mean uptake by 0.017 ± 0.04 Pg C yr^{-1}. The interannual variability in the NOIAV flux time series in figure 2.6 comes from interannual variability in the atmospheric pCO_2 values.

The sensitivity of the inversion results to the representation of the seasonal cycle is larger than that for interannual variability, for both the posterior values of A and the decadal-mean flux about the year 2000 (c.f. figure 2.7 (b) & (d)). Using the empirical seasonality instead of the model-based estimate maintains the global mean value of A. The global difference is $0.0 \pm .3$ μatm yr^{-1}, though there are particularly large decreases in the posterior value of A in the Atlantic and Equatorial Pacific. These decreases are partially compensated by increases in the value of A in the North Pacific. The flux is significantly altered in the North Atlantic and the Southern Ocean, with both regions showing reduced uptake under the empirical seasonal cycle. The global difference in the nominal flux is a decreased uptake of 0.2 ± 0.05 Pg C yr^{-1}. The flux

time series in figure 2.6 shows the combined results of the differences in the mean flux and the evolution of the surface pCO_2. The fluxes calculated from the inversion with the MOM4p1-Bling seasonality show larger uptake than the other inversion cases, but also show less increase in CO_2 uptake of the ocean through time.

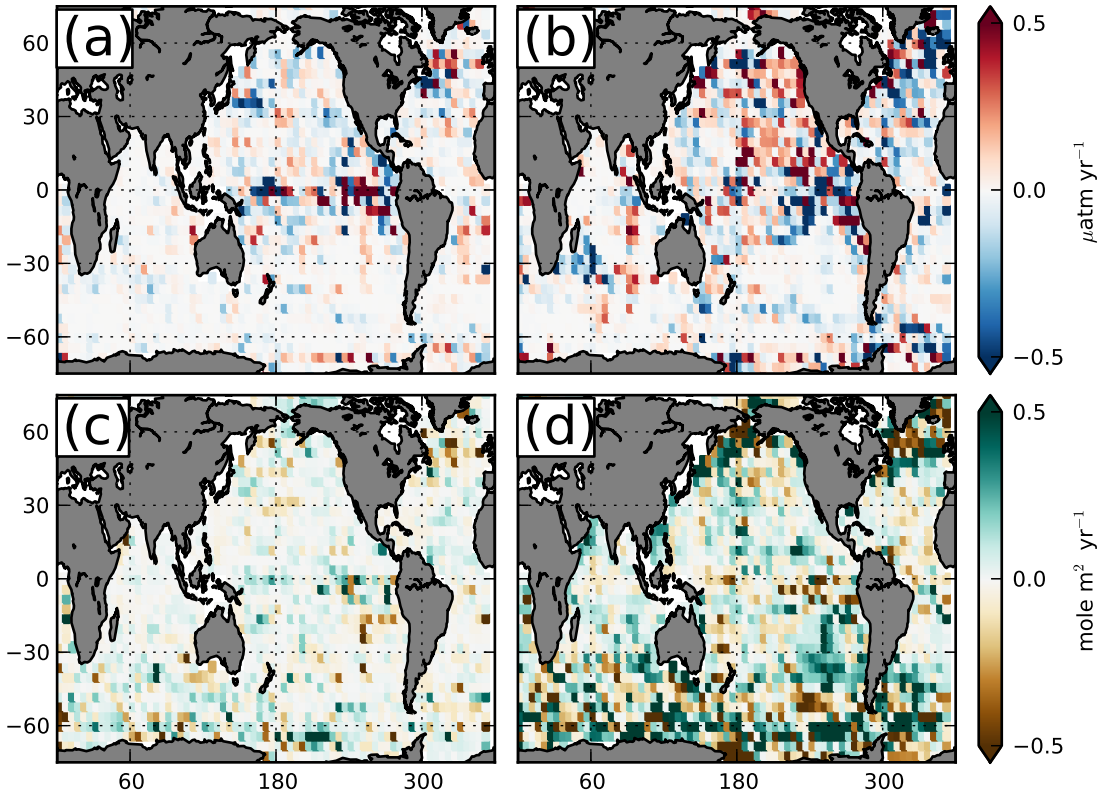

Figure 2.7: Panel (a) shows the difference in the mean of A between the standard MCCM inversion and the run with no interannual variability and panel (b) shows the same between the standard case and the run with the MOM4p1-Bling based seasonality. In both panels, positive values indicate faster growth in the standard case. Panel (c) shows the difference in mean year 2000 flux between the standard and no interannual variability cases and panel (d) shows the same for the seasonal difference. Here positive values indicate more outgassing or less uptake.

2.4 Discussion

In the following subsections we discuss the results of the MCMC-based inversion of surface pCO_2 in light of previous studies. We show how this global analysis is consistent with the results of previous regional analyses of pCO_2. This is an important check, as much of the data that was used in these previous studies is included in LDEO2010. The section ends with an analysis of the Southern Ocean pCO_2 trend, where our trend differs significantly from recently published results.

As a matter of terminology, in this section we often refer to the significance of the posterior trend estimate, A. We refer to the the trend as significantly 'lagging' the atmosphere when the 90th percentile of the posterior distribution for A is less than the atmospheric growth rate of 1.6 μatm yr^{-1}. The trend is significantly 'leading' the atmosphere with the 10th percentile of the posterior distribution for A is greater than the atmospheric growth rate. When results are referred to as not significant, though the mean estimate may be different from 1.6 μatm yr^{-1}, it means that the value of A is cannot be separated from the atmospheric increase at the 10% certainty level in our 1-sided test. A surface pCO_2 trend that lags the atmosphere tends toward more uptake of CO_2 by the ocean and a trend that leads the atmosphere tends toward less uptake.

The MCMC estimates a global mean increase in surface ocean pCO_2 of 1.4 ± 0.5 μatm yr^{-1}. The posterior mean value of A is less than the atmospheric growth rate for 73% of the ocean surface. The difference from the atmospheric value is significant for 42% of the ocean surface, with 34% lagging and 8% leading the atmospheric growth rate. Regionally, we see a significant lagging of the atmospheric pCO_2 through much of the North Pacific, the Subpolar North Atlantic and parts of the Southern Ocean. We calculate a surface pCO_2 growth faster than the atmosphere in parts of the Eastern Equatorial Pacific, Subtropical North Atlantic and Southern Ocean.

For comparison of the time evolution of the fluxes, which is closely related to the time evolution of surface pCO_2, the inverse estimate of Khatiwala et al. (2009) shows an increase of 0.5 PgC yr^{-1} $decade^{-1}$ from the 1980s (1.8 ± 0.5) to the 2000s (2.3 ± 0.6), similar to the growth rate that we find, 0.4 ± 0.1 PgC yr^{-1} $decade^{-1}$. The other estimates of the global ocean CO_2 uptake seem consistent with the decadal increases in the MCMC-derived oceanic uptake (c.f. figure 2.6).

2.4.1 Pacific

In the MCMC result, the Northern Subtropical Pacific shows a slower than atmospheric growth in the surface pCO_2, in agreement with Takahashi et al. (2006). The average slope in the region is 1.5 ± 0.4 μatm yr^{-1} with a small standard error, c.f. table 2.1, which indicates a coherent behavior in the basin. We find that many cells in this regions significantly lag the atmosphere, indicating that the MCMC-derived pCO_2 is estimating a growing flux. The whole North Pacific shows a total increased uptake greater than 0.25 PgC yr^{-1} over the whole period (cf A.3) .

In the Eastern Equatorial Pacific, we found oceanic pCO_2 increasing faster than the atmosphere in the region of upwelling, with a slower than atmospheric growth north of the upwelling. These trends are consistent with the analysis of Feely et al. (2006). In the Western Equatorial Pacific, we see a trend toward increasing ocean uptake as in Ishii et al. (2004). The whole Equatorial Pacific is characterized by strong mean trends (c.f. fig. 2.3(b)), but the uncertainty in the estimates is too large for the slope to be significantly different from the atmospheric one (c.f. fig. 2.3(b)). The high level of uncertainty in the cell-by-cell estimates leads to substantial uncertainty in the mean trends for the region, as in table 2.1.

Table 2.1: pCO_2 Slope Estimates

Region	CT Regions [1]	Area (%)	MCMC Slope [μatm yr^{-1}] (SE) [2]
North Pacific	10-16	12.3	1.4 ± 0.4 (0.0)
Eastern Equatorial Pacific	19	4.8	1.6 ± 0.7 (0.1)
Subpolar North Atlantic	2,3	4.8	1.3 ± 0.5 (0.1)
Subtropical North Atlantic	4	3.9	1.6 ± 0.4 (0.1)
Southern Ocean (<45S)	9,10,25,30	17.3	1.4 ± 0.5 (0.0)
World	All	100.0	1.4 ± 0.6 (0.0)

[1] Regional mapping for CARBONTRACKER Ocean Regions (Peters et al., 2007), map shown in figure A.8.
[2] Uncertainty listed as both the standard deviation and the standard error for the region.

2.4.2 Atlantic

In the MCMC estimate, the subtropical gyre region of the North Atlantic has a regional average trend parameter of 1.6 ± 0.4 μatm yr^{-1} (c.f. table 2.1). Figure 2.3(b) shows that the eastern subtropical gyre has a region of faster than atmospheric growth, which has been identified previously (Schuster and Watson, 2007). A slower than atmospheric growth in the western part of the gyre compensates for the faster than atmospheric growth in our result. Thus, our estimate of the regional average is not significantly different from the atmospheric growth rate because we average over strong lagging and leading signals.

Of note in both the Subtropical and Subpolar North Atlantic is the basin-averaged consistency with the recent results of McKinley et al. (2011). They were the first to show that the regional trends in the North Atlantic were strongly influenced by the time window over which they were reported. They showed that trends in the surface pCO_2 became indistinguishable from the atmospheric growth rate for time series approaching 30 years. This is true in our estimates of the North Atlantic growth rates as well. While our result shows that within each region there are cells with

significantly different growth rates than the atmosphere, that significant difference is lost in regional averaging.

2.4.3 Southern Ocean

The most notable difference between our results and previous studies is in the Southern Ocean (<45S) where we show a slower than atmospheric growth in the mean, 1.4 ± 0.5 μatm yr^{-1}, though not a significant difference from the atmosphere. This result differs from that of Lenton et al. (2012), who showed an increasing trend of 2.2 ± 0.2 μatm yr^{-1} for the period 1995-2008 using ordinary least squares fitting of the measurements in LDEO2010. We can examine the reasons for the disparity by sampling the pCO_2 time series generated by the MCMC inversion and using ordinary least squares fitting to calculate the pCO_2 trends for the whole region as in Lenton et al. (2012). To evaluate the influence of the seasonal cycle and interannual variability, we then apply corrections to the sampled MCMC fields from the SEAS and IAV time series and recalculate the trend.

Table 2.2 shows the slope estimates that result from estimating the pCO_2 trends with the MCMC output where LDEO2010 has values for the full period, 1980-2009, and the shorter period,1995-2008. The slope estimates calculated directly from the MCMC pCO_2 output, sampled where observations exist in LDEO2010, show a faster than atmospheric growth rate, consistent with the one from (Lenton et al., 2012). The table shows that including seasonal and interannual adjustments from the IAV and SEAS terms brings the basin slope estimates closer to the MCMC-based estimate of 1.4 ± 0.5 μatm yr^{-1}. In this case, including the seasonal cycle plays a larger role than the interannual variability, but both decrease the slope estimate in the 1995-2008 time period.

The role of the SEAS and IAV adjustments is lessened by taking the whole period into account, which is shown in the second row of table 2.2. As more samples are

Table 2.2: Alternative pCO_2 estimates

Dates	A^*_{sub}	A_{sub}	$A_{\text{sub}} + A_{\text{iav}}$
07/1995 - 06/2008	2.23 ± 0.31	1.50 ± 0.18	1.45 ± 0.19
01/1980 - 12/2009	1.87 ± 0.09	1.68 ± 0.05	1.64 ± 0.06

[1] The slope calculated by sampling the MCMC output without adjustments A^*_{sub} , with seasonal adjustments A_{sub}, and with seasonal and interannual adjustments (IAV) at LDEO2010 points within 2 time windows.

included, covering a wider time window, the calculated trends come to resemble the mean behavior of the MCMC-based pCO_2 history. This result is consistent with the study of Fay and McKinley (2013), where the authors show that the multi-decadal trend in the Southern Ocean pCO_2 is slower but statistically indistinguishable from that in the atmosphere and that trends calculated from shorter time periods can vary substantially, compared to the atmospheric trend, due to decadal variability.

In order to better understand the pCO_2 trend in the Southern Ocean (<45S), we separated the MCMC-derived pCO_2 into temperature and non-temperature driven components (McKinley et al., 2006), and calculated the trend in each component from 1980-2005 using the monthly values and ordinary least-squares methods. The temperature and non-temperature components of the total trend are shown in figure 2.8. For the temperature record, we used the NOAA monthly SST optimal interpolation product NOAA-OI.v2 (Reynolds et al., 2002). This SST product shows a cooling trend in the surface temperatures south of 45S for the 1980-2005 period. That negative trend in temperature drives a negative trend in the temperature-driven pCO_2, as in figure 2.8(b). A qualitatively similar surface cooling is expressed in the Hadley Center SST product HadISST1 (Rayner et al., 2003), the temperature measurements made co-incidentally with the pCO_2 samples (Fay and McKinley, 2013), and in analyses based on float data (albeit for a shorter period) (Gille, 2008). The negative trend in surface pCO_2 masks a trend in the non-temperature driven pCO_2, shown in figure

2.8(c), that is faster than the atmospheric growth for much of the ocean between 50S-65S, in the region of the ACC. The faster than atmospheric growth is strongest in the Drake Passage and the Southern Atlantic Oceans. The zonal means of the component trends for the Southern Ocean are shown in table 2.3 where it can be seen that the trend in temperature component moderates a faster than atmospheric growth in the non-temperature component between 50S-62S.

Table 2.3: pCO_2 Component Trends

Latitude	Total	Temperature	Non-temperature
44.0	-0.13 ± 0.15	0.06 ± 0.17	-0.18 ± 0.27
48.0	-0.10 ± 0.16	-0.01 ± 0.15	-0.09 ± 0.21
52.0	-0.07 ± 0.18	-0.09 ± 0.12	0.02 ± 0.17
56.0	-0.14 ± 0.12	-0.13 ± 0.14	0.00 ± 0.18
60.0	-0.15 ± 0.24	-0.16 ± 0.13	0.03 ± 0.27
64.0	-0.28 ± 0.40	-0.14 ± 0.14	-0.09 ± 0.40
68.0	-0.36 ± 0.50	-0.03 ± 0.06	-0.26 ± 0.48
72.0	-0.75 ± 0.46	-0.00 ± 0.03	-0.67 ± 0.44

[1] The zonally-averaged trend in surface pCO_2 μatm yr^{-1} and the temperature and non-temperature decompositions. The total and non-temperature trends are shown as deviations from the atmospheric growth rate, where negative indicates slower than atmospheric growth. Since the components are calculated by linearization of carbonate chemistry, the temperature and non-temperature trends do not necessarily complement each other to generate the total trend. The uncertainty listed here is the zonal sample standard deviation of the mean.

The balance between the temperature and non-temperature driven variations in surface pCO_2 in the Southern Ocean points to an interesting set of dynamics, relating to the response of the carbon fluxes in the Southern Ocean to changes in climate and the proposed feedbacks to changes in wind stress (Le Quéré et al., 2007). Over the 1980-2010 period, reanalysis products show a significant increase in the Southern Annular Mode (SAM) index and an intensification of the westerly winds (Swart and

Fyfe, 2012). Surface cooling in the Southern Ocean has previously been associated with positive phases of the SAM index, with the intensification and poleward shift of the westerlies and increased Ekman flow and sea-air interaction playing a significant role in that cooling (Verdy et al., 2006; Ciasto and Thompson, 2008). Likewise, previous modeling studies of the Southern Ocean have proposed that positive deviations of the SAM index can drive enhanced northward transport and upwelling of carbon rich deep water via increases in Ekman flow and the associated meridional overturning (Treguier et al., 2010).

The results of the MCMC pCO_2 inversion seem to be consistent with the model-based process studies of carbon flux, where the circulation-driven pCO_2 has increased in the surface Southern Ocean as the SAM index has increased over the last 30 years, resulting from the net effect of upwelling of carbon rich waters that is not fully compensated by increasing biological production (Lovenduski et al., 2008). We find that this increase was counteracted by a cooling of the surface temperatures, possibly due to the same circulation processes, such that the total outgassing from the Southern Ocean actually reduced, i.e. the uptake of anthropogenic CO_2 increased. How these processes will continue to respond to the projected changes in the annual mean and seasonal SAM indices is an open area of research (Polvani et al., 2011), particularly as some high resolution modeling studies indicate that permanent changes in the SAM index might drive long-term warming of the Southern Ocean SST as eddy heat flues compensate for the increased Ekman flow (Hogg et al., 2008; Screen et al., 2009). Forthcoming modeling studies with high resolution models aim to address how the carbon system responds to changes in SAM at the process-level.

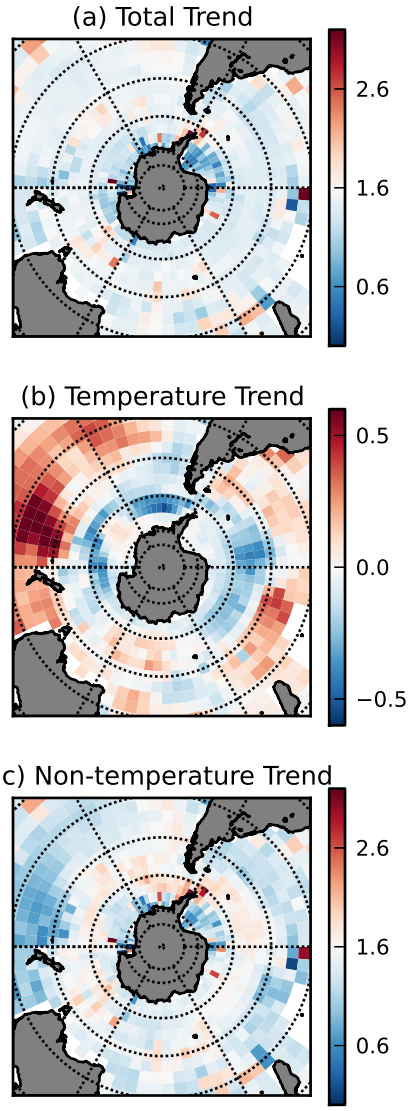

Figure 2.8: Panel (a) shows the MCMC slope estimate for the Southern Ocean in μatm yr^{-1}. Panel (b) is the trend in the temperature-driven component of pCO_2, and (c) shows the non-temperature component trend.

2.5 Conclusions

In this paper, we present the application of MCMC sampling to the estimation of long-term trends in surface pCO_2 and air-sea CO_2 fluxes based on surface pCO_2 data and model-based variability. This method allows us to formally introduce modeled interannual and seasonal variability to the trend estimation problem and reduce biases that result from the sparse nature of our observations of ocean carbon. The results can be thought of as a plausible time history of surface pCO_2, and its trends, that is constrained to data where it is available and is otherwise model-based. The model-based variability incorporates the effects of ocean circulation, biogeochemistry and air-sea interaction on surface pCO_2 as represented by an ocean general circulation model is that forced by atmospheric reanalysis. Thus the variability that we impose is a first step toward estimating surface pCO_2 history while incorporating process-based constraints.

The mean flux estimates generated by the MCMC method are broadly consistent with the canonical estimates of Takahashi et al. (2009a) and other studies based on ocean inversion. For global trends, we found that the ocean exhibits an increasing uptake of CO_2 over the time period 1980-2009, consistent with a global surface pCO_2 that is growing more slowly than the atmospheric value. The MCMC with interannual variability and empirical seasonality results in a global increase in the CO2 uptake of 0.4 ± 0.1 PgC yr^{-1} $decade^{-1}$. This would account for nearly 50% of the global carbon sink increase calculated by Ballantyne et al. (2012).

Some regions show pCO_2 trends that are notably different from the global average. The subtropical North Atlantic and Equatorial Pacific are the two regions that show the fastest growth in surface pCO_2, indicating a decreasing uptake of carbon by the ocean. Some parts of the Southern Ocean also show faster than atmospheric growth in the surface pCO_2, but the region as a whole (south of 45S) is an increasing sink. Interestingly, our results indicate that DIC is increasing throughout the Southern

Ocean, but that surface cooling trends are more than compensating for the growth in DIC such that a slower than atmospheric pCO_2 growth rate and increasing uptake are maintained.

We note that these are regions of high seasonal and interannual variability and that detecting secular trends against the background variations will remain a challenge in the future. Including interannual variability via the MCMC method has a notable effect on local trend estimates and is an important consideration for studies of surface pCO_2, although we found that the effect tended to be smaller when taking regional averages and calculating global trends in the air-sea CO_2 flux.

Proper representation of the seasonal cycle around the global ocean remains a priority. Different estimates of the seasonal cycle lead to substantial differences in the MCMC-based estimates of local and regional pCO_2 trends and mean fluxes. Ultimately the sensitivity to the seasonal cycle drives significant differences in the global CO_2 fluxes. Based on this sensitivity, improved observations and models of the seasonal cycle in surface pCO_2 are a necessity for improving carbon flux estimates based on surface observations and for providing additional constraints on the seasonal variations in surface pCO_2.

The MCMC technique that we present is a promising method for continued investigation of the historical pCO_2. Possible extensions of this work might use the flexibility of the MCMC method to include other types of observation-driven data to improve the pCO_2 estimation. For example, SST observations and ocean color data might help to resolve the seasonal cycle in pCO_2. Likewise, allowing the grid structure of the inversion to be refined by the MCMC where there is sufficient information in the pCO_2 data would benefit the regional veracity of the resulting pCO_2 history and could take advantage of the improved spatial and temporal resolution in updating global databases of surface pCO_2 measurements, such as SOCAT (Pfeil et al., 2012).

Chapter 3

Southern Ocean Carbon Trends: Modeling and Detection

The Southern Ocean plays a central role in shaping the global ocean's circulation and biogeochemical cycling. At latitudes near Drake Passage, the Southern Ocean lacks meridional boundaries, which allows for two closely related phenomena. Firstly, the strong, eastward-flowing Antarctic Circumpolar Current (ACC) connects the Atlantic, Pacific and Indian Ocean basins, allowing for mixing of water masses between the basins. Secondly, the westerly winds drive significant upwelling of old and nutrient rich waters from the deep ocean to the surface, that are almost free of anthropogenic carbon, where they can interact with the atmosphere. Because of these properties, the Southern Ocean closes the overturning circulation of the global ocean (Marshall and Speer, 2012), maintains the nutrient balance of the low latitude oceans (Sarmiento et al., 2004) and sequesters anthropogenic CO_2 and excess heat from the atmosphere (Frölicher et al., 2014).

The processes that control the Southern Ocean's circulation and biogeochemistry, and thus a big part of the global ocean's, remain unresolved. Direct measurements provide valuable but sparse information, because sampling is limited to cruise lines

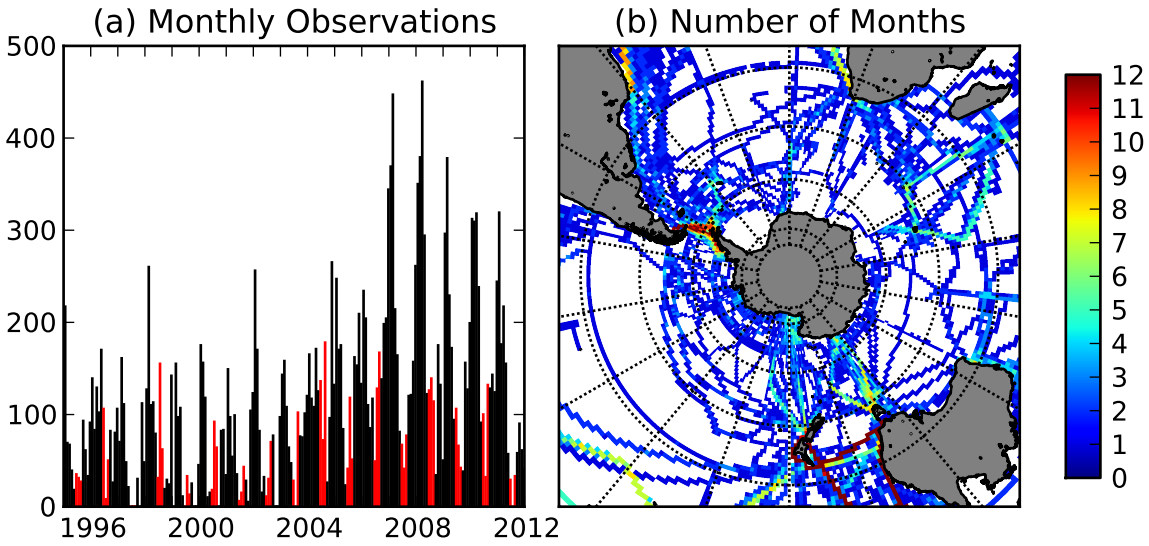

Figure 3.1: The number of surface measurements of pCO_2 in gridded SOCAT v2, between 1995 and 2012. (a) Total monthly observations, south of 30 ° S, with winter months (June-July-August) in red. (b) Calendar months occupied, where twelve indicates full occupation of the seasonal cycle and white indicates no available measurements.

and biased toward summer months. This is particularly the case for biogeochemical observations (Gruber et al., 2009; Takahashi et al., 2009a). For example, the surface pCO_2 measurements that provide critical constraints on the sea-air CO_2 flux leave many months and areas of the Southern Ocean unsampled (c.f. figure 3.1).

In contrast to measurements, general circulation models (GCMs) provide complete information on a model grid. However, current GCMs rely on parameterizations to simulate sub-grid scale processes, such as mesoscale eddy processes. Mesoscale eddies govern much of the Southern Ocean dynamics and the reliance on parameterizations of their effects decreases confidence in model results and projections (Hallberg and Gnanadesikan, 2006). Likewise, biological models are incomplete representations of the ecology and production within the Southern Ocean. Together, the sparsity of the data and the incomplete nature of model simulations create significant opportunity for continued investigation.

The focus of this work is the Southern Ocean CO_2 uptake. Fluxes of anthropogenic CO_2 across the surface of the Southern Ocean are thought to account for up to 50% of the total oceanic uptake (Gruber et al., 2009), yet storage of anthropogenic CO_2 is small in the Southern Ocean compared to the in situ fluxes. A large proportion of the total uptake of CO_2 accumulates in Subantarctic Mode Water and Antarctic Intermediate Water (Sabine et al., 2004) and flows into other ocean basins (Caldeira and Duffy, 2000). The oceanic uptake itself amounts to 25% of annual CO_2 emissions from burning fossil fuels and land use change (Le Quere et al., 2009). The primacy of the Southern Ocean flux to oceanic uptake implies that constraining the Southern Ocean flux is essential to constraining the global oceanic uptake of anthropogenic CO_2. Likewise, understanding the dynamics of the future evolution of the Southern Ocean uptake is essential to understanding the total future oceanic uptake.

Simulations of the future climate show that the Southern Ocean will continue to play a key role in anthropogenic CO_2 uptake and that given continuing emissions of CO_2, the uptake in the region will continue to grow (Roy et al., 2011; Lovenduski and Ito, 2009). The rate of increase, however, will be subject to known processes, such as changes in the Revelle Factor, and unknown processes, including the effects of climate change. Future climatic changes may alter the balance between circulation, stratification and biological production in the Southern Ocean and decrease the future uptake of anthropogenic CO_2 (Sarmiento et al., 1998). In order for us to distinguish interannual and decadal variability from secular trends, we must understand how these processes interact and have sufficient observations to inform our understanding at the process level.

Autonomous floats provide a powerful complement to shipboard measurements by routinely sampling profiles at high temporal density. The Argo program has been a substantial new data source about the global ocean since its deployment, including in the Southern Ocean (Roemmich et al., 2009). Recent advances in float-based

measurement platforms make it possible to equip floats with sensors of pH, nitrate, and oxygen (Johnson et al., 2010). When combined with inverse methods and data assimilation, such floats can provide both improved state estimates and constraints for process-based models of the carbon system and ocean biogeochemistry. In this paper we evaluate how effective such a system might be in resolving the Southern Ocean CO_2 flux for monthly and annual averages, and long-term trends.

Here we will review model and empirical estimates for CO_2 uptake in the Southern Ocean, how it may respond to climate change and the difficulties imposed by the sparse measurements in the region. We use an observational system simulation experiment (OSSE) to discuss float-based sampling benefits and strategies. This experiment complements a previous analysis, which showed that a float-based sampling with 3-monthly sampling of 3x30 degree latitude-longitude resolution could achieve annually averaged Southern Ocean flux estimates with acceptable error (Lenton et al., 2006).

3.1 Review of Southern Ocean CO_2 uptake

The global oceanic uptake of anthropogenic CO_2 and natural CO_2 depends strongly on the uptake that takes place in the Southern Ocean. In this section, we demonstrate that the Southern Ocean is the primary source of uncertainty in the global oceanic uptake for a recent decade (1995-2005) and that the Southern Ocean plays a substantial part in setting the sensitivity of the CO_2 uptake to climate change. We consider examples from the literature and present model results for CO_2 uptake. Model results from the fifth coupled model intercomparison project are included, featuring 12 climate-carbon cycle models forced with historical atmospheric CO_2 concentrations and radiative effects[1]. These simulations were previously analyzed to compare the ability of the current generation coupled climate models to simulate the uptake of

anthropogenic CO_2 and excess heat (Frölicher et al., 2014). For comparison to the CMIP5 historical simulations, ocean-biogeochemistry simulations are included, based on the NOAA-GFDL MOM4p1 model (Griffies et al., 2004), coupled to the biogeochemistry model BLING (Biology, Light, Iron, Nutrient and Gases) (Galbraith et al., 2011). These simulations were forced at the ocean surface with three different atmospheric reanalysis products: NCEP-1 (Kalnay et al., 1996), CORE-II (Large and Yeager, 2009), and ERA-40 (Uppala et al., 2005). The atmospheric reanalysis forcing should reflect the actual climatic variability over our period of interest, in contrast to the CMIP5 models, which exhibit their own states of the climate under forcing.

Each set of simulations has a 'historical' case where the biogeochemical model feels the historical increase in atmospheric CO_2 such that the oceans are a net sink of CO_2 from the atmosphere and a 'preindustrial' case where atmospheric CO_2 concentrations are held constant at preindustrial values. Anthropogenic CO_2 uptake is calculated as the difference between the fluxes from the 'historical' and 'preindustrial' simulations from both the CMIP5 and MOM4p1-BLING ensembles. The flux calculated directly from the 'historical' simulations is called the total or contemporary flux. The contemporary CO_2 flux is the sum of the natural and anthropogenic CO_2 fluxes. For purposes of comparison, we include data-based estimates of the anthropogenic and contemporary CO_2 fluxes. The estimates of the anthropogenic CO_2 uptake come from an inversion of ocean interior measurements (Mikaloff Fletcher et al., 2006). The contemporary uptake estimates come from inversions of surface ocean pCO_2 data. We use both the LDEO climatology (Takahashi et al., 2009a), centered on the year 2000, and a reconstruction of historical pCO_2 from 1980-2009 (MCMC pCO_2 history, see chapter 2).

[1]We include named output from the following modeling groups: MIROC-ESM (Watanabe et al., 2011), IPSL-CM5 (Dufresne et al., 2013), GFDL-ESM2M and GFDL-ESM2G (Dunne et al., 2013). We additionally include output from 13 more models, unnamed, cited in a similar analysis in Frölicher et al. (2014).

3.1.1 Decadal estimates

Recent model simulations indicate that the Southern Ocean (>30 ° S) anthropogenic CO_2 uptake was 0.8 ± 0.1 PgC yr^{-1} (Frölicher et al., 2014), for the decade 1995-2005, with a range defined by the red and blue lines in figure 3.2(a). In that decade, the Southern Ocean uptake constituted 40-50% of the global total in the modeled fluxes. Empirical estimates from oceanic inversion estimate the uptake to be 1.1 PgC yr^{-1} (52% of the global total) for the same region and decade (c.f. black line in figure 3.2(a)) (Mikaloff Fletcher et al., 2006). The reduced uptake in the suite of models is consistent with the whole of the CMIP5 historical simulations, which show less oceanic uptake of CO_2 than empirical studies (Friedlingstein et al., 2013). Poor simulation of the stratification in the Southern Ocean is a suspected source of the underestimated anthropogenic uptake (Frölicher et al., 2014). The proportion of anthropogenic CO_2 that enters through the Southern Ocean appears to be stable through time, with historical estimates of the total uptake indicating about 50% of oceanic anthropogenic CO_2 entered through the Southern Ocean (Khatiwala et al., 2009).

The estimates of the contemporary CO_2 uptake vary across a larger range than the anthropogenic uptake. The estimates of the northward cumulative flux of contemporary CO_2 span 1.1 ± 0.2 Pg C yr^{-1} at 30 ° S (shown in figure 3.2(b)). The total range in estimates is set by the CMIP5 historical simulations (shown in blue lines in figure 3.2(b)). The MOM4p1-BLING simulations show slightly higher uptake, ranging between 1.2 and 1.4 Pg C yr^{-1} (red lines in figure 3.2(b)). The empirical estimate based on the MCMC pCO_2 history gives 1.3 ± 0.3 Pg C yr^{-1} (green line in figure 3.2(b)) and the LDEO climatology gives 1.0 ± 0.2 Pg C yr^{-1} (black line in figure 3.2(b)). The full spread in the CMIP5 estimates of contemporary uptake reveals significant uncertainty in the CO_2 flux as simulated by that ensemble. The Southern Ocean is not a sink of CO_2 south of 45 ° S in some models, which indicates significant

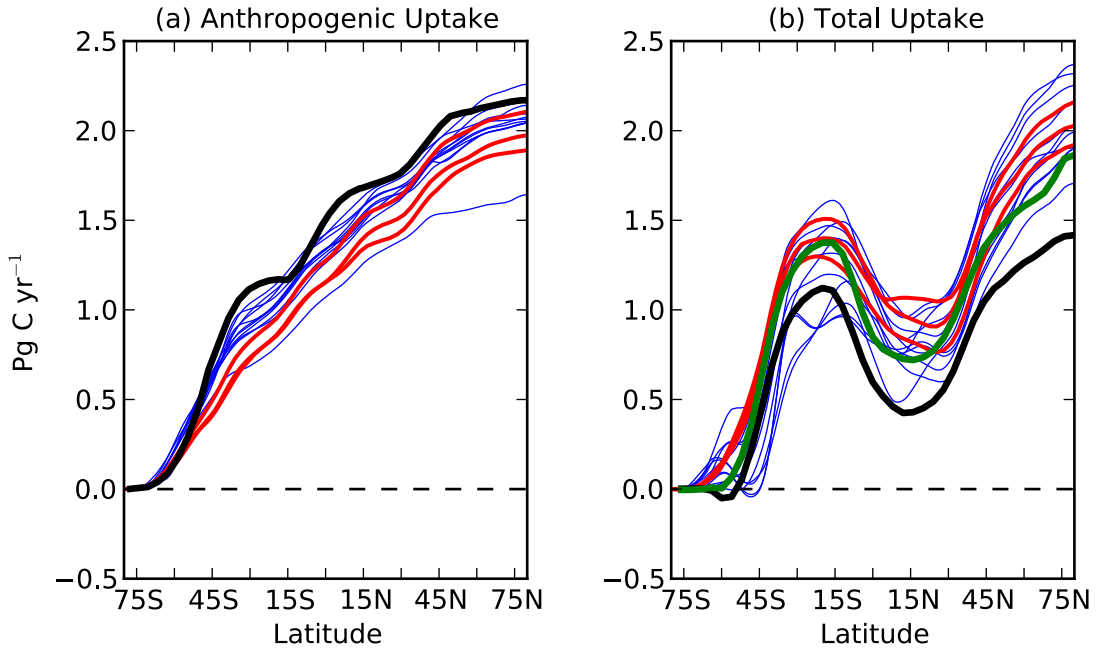

Figure 3.2: The cumulative fluxes integrated from 90°S to 90°N, in PgC yr^{-1}, of (a) anthropogenic CO_2 and (b) total CO_2. Estimates come from forced (red) and coupled (blue) OGCMs averaged over 1995-2005 and show significant spread by 30 °S. The black line in (a) shows the oceanic inversion results from Mikaloff-Fletcher et al. (2007). In (b), the LDEO pCO2 year 2000 climatological flux is in black and the MCMC pCO2 history, averaged over 1995-2005, is in green.

process-level errors in the physical or biogeochemical components of the simulations. The northward cumulative plots in figure 3.2 show that the uncertainty in the total global uptake is established by 30 ° S and thus the Southern Ocean is critical to the estimates of both the global mean and the uncertainty in CO_2 uptake.

The seasonal cycle is considered for uptake south of 45 ° S in figure 3.3. The observationally-derived uptake in the summer and fall is driven by biological uptake and surface stratification. In the winter, deep mixed layers and the associated upwelling CO_2 drive weakened uptake or outgassing (Takahashi et al., 2009a) (c.f. black and green lines in figure 3.3). In CMIP5, the range in monthly estimates is quite large over the annual cycle and those models do not demonstrate a clear seasonal cycle (blue

lines in figure 3.3) (Anav et al., 2013). The MOM4p1-BLING simulations (red lines in figure 3.3) show reasonable agreement with the empirically derived seasonal cycles, though the magnitude of the seasonal cycle is smaller in the model. The CMIP5 models, however, are inconsistent and many vary widely from the observationally based estimates. The seasonal amplitude of the fluxes in the CMIP5 models is particularly large compared to the observationally based estimates, in opposition to what happens with the forced models.

Reproducing the seasonal cycle of CO_2 fluxes in the Southern Ocean clearly poses a particular challenge for models. In forced ocean models, resolving the mixed layer depths, and thus the entrainment and export of Dissolved Inorganic Carbon (DIC) from the surface, is vital to capturing the seasonal cycle in CO_2 fluxes (Lenton et al., 2013). Most forced models miss winter outgassing because of poor mixed layer simulation, including the MOM4p1-BLING simulations. These errors seem enhanced in the CMIP5 models, which have a wide variety of mixed layer characteristics but are generally too shallow (Sallée et al., 2013). However, the relative contributions of biological processes are yet to be determined, as the parameterization of co-limitation by temperature, light and micronutrients can have a significant impact on the seasonal cycle as well (Galbraith et al., 2010; Geiderl et al., 1998; Li et al., 2010).

The paucity of measurements makes empirical analysis of the seasonal cycle difficult. Analysis of surface pCO_2 measurements provides the most information about the seasonal flux of CO_2 over several decades. The sampling that is available for surface pCO_2 in the newly release SOCAT database (Pfeil et al., 2012; Sabine et al., 2012), similar in nature to that which was used to make the climatology (Takahashi et al., 2009a), is shown in figure 3.1. It shows that the seasonal cycle is resolved only in limited parts of the Southern Ocean and that there is a strong bias toward summer sampling. The lack of measurements limits the ability of the data to constrain the seasonal fluxes. For instance, the two pCO_2 data products shown in figures 3.2(b)

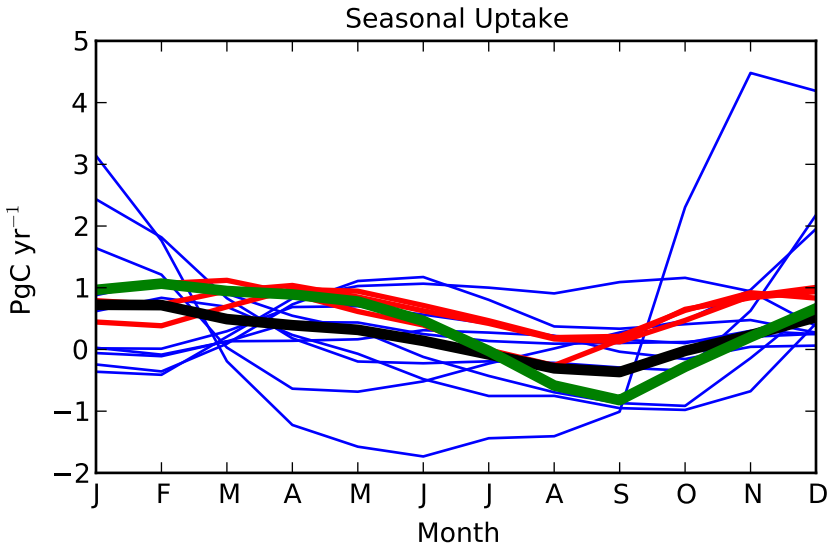

Figure 3.3: The seasonal cycle of CO_2 uptake into the Southern Ocean, south of 45° S, in Pg C yr^{-1}. The CMIP5 models are shown in blue, MOM4p1-BLING models in red, and the LDEO pCO_2 climatology in black and the MCMC pCO_2 history in green. The area south of 45°S was chosen to avoid contaminating the seasonal cycle with subtropical signals.

and 3.3 use the same surface pCO_2 dataset (Takahashi et al., 2009b) to calculate the air-sea CO_2 flux, yet the fluxes from the MCMC pCO_2 history express a higher amplitude seasonal cycle than the LDEO climatology. Meanwhile, they are not distinguishable with the observations, with root mean squared error (RMSE) against the data of 20.6 (MCMC history) and 23.7 (climatology). The disagreement between the two occurs in regions and months where there is little or no data, and is created by differences in the spatial interpolation schemes, representation of the seasonal cycle and interannual variability (Majkut et al., 2014a). The difference between the estimates projects into the overall carbon budget, where the available measurements cannot separate estimates of the CO_2 flux that differ by 0.3 PgC yr^{-1} or nearly 30% of the total Southern Ocean uptake.

3.1.2 Southern Ocean carbon-climate feedbacks

Ocean circulation and mixing changes induced by global warming might affect the CO_2 uptake through several mechanisms. Wind-driven increased upwelling of deep waters rich in CO_2 may result in increased outgassing of natural CO_2 if biological production does not balance the increased supply of DIC (Lovenduski et al., 2007). These wind-driven changes are closely related to changes in the Southern Annular Mode (SAM) (Lenton and Matear, 2007). However, increases in stratification due to changes in sea ice or precipitation at high latitudes may oppose the wind-driven changes via a reduction of natural outgassing south of the ACC (Sarmiento et al., 1998). In addition, thermal solubility effects may reduce the ability of the surface to capture CO_2 from the atmosphere (Sarmiento et al., 1998). The potential impact of climate change on the Southern Ocean CO_2 uptake is difficult to anticipate, because of the varying balances between biology and ocean circulation that govern the Southern Ocean CO_2 uptake.

The impact of climate is estimated by calculating the difference in the CO_2 uptake between model runs with and without climate change, but with increasing atmospheric CO_2 concentrations. Current coupled modeling efforts indicate that the Southern Ocean CO_2 flux may have already decreased due to changes in the climate, relative to model simulations where climate is held constant, but that the impact is currently small (Frölicher et al., 2014). Northward cumulative climate impacts indicate that climate signals decreased the modeled CO_2 uptake in the Southern Ocean between 1970-2005 by 2 to 3 PgC (c.f. figure 3.4(b)). That decrease in uptake holds in 5 of the 7 simulations.

The picture of reduced uptake in the past few decades, relative to what might be expected in the absence of climate change, holds across forced and coupled models and the empirical estimates. Figure 3.4(b) shows the northward cumulative climate impact from the CMIP5 and MOM4p1-BLING models integrated from 1970 to 2005.

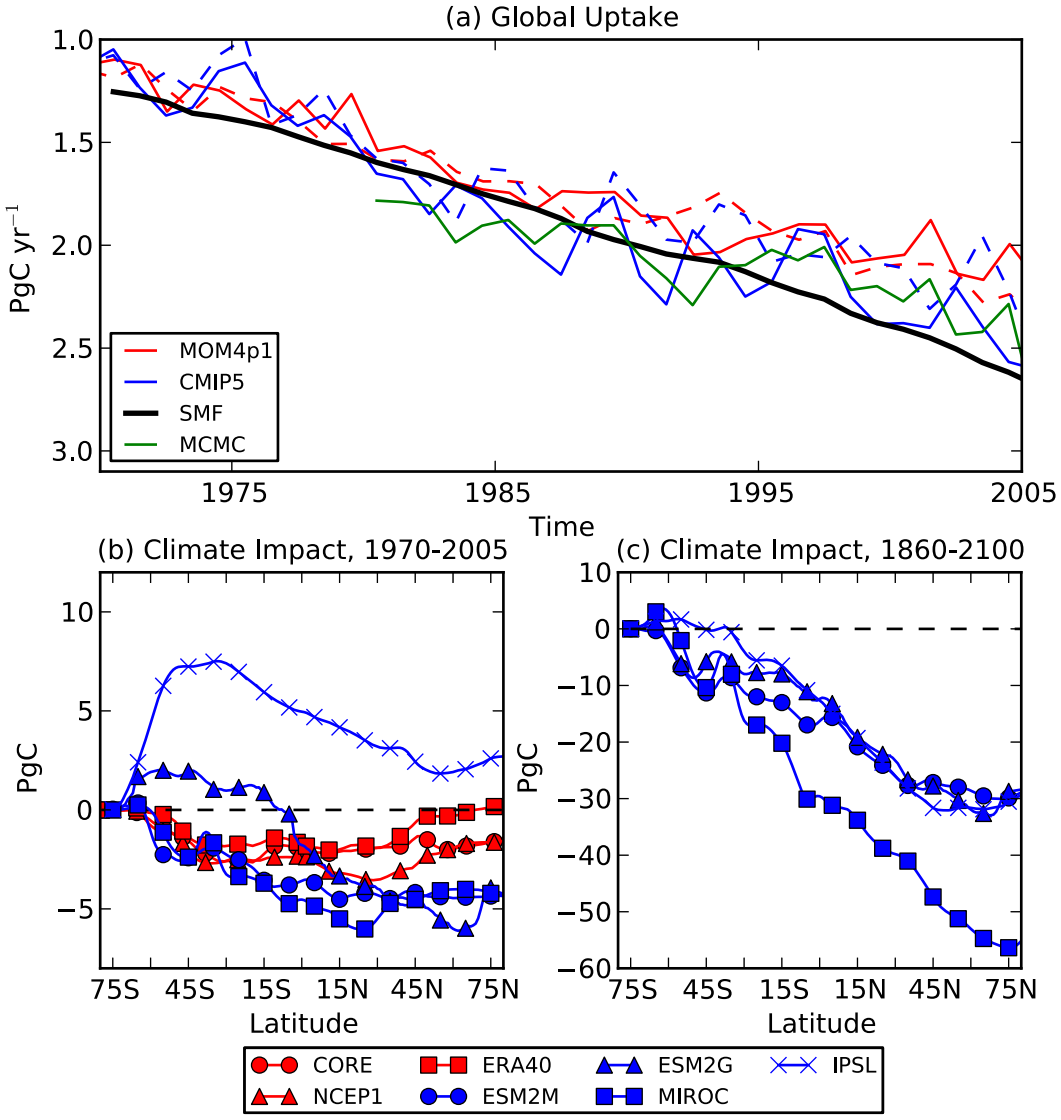

Figure 3.4: (a) The impact of climate change on the total global ocean CO_2 uptake between 1970-2005. The time series show the uptake of CO_2, with (dashed) and without (solid) climate variability, by the ocean from CMIP5 (blue) and MOM4p1-BLING simulations (red). The MCMC uptake is shown in green and an extrapolation of the Mikaloff-Fletcher inversion is shown in solid black. (b) The climate impact on CO_2 uptake, in PgC, integrated over 1970-2005 and northward from 90°S for each model. (c) The climate impact on CO_2 uptake, in PgC, integrated over 1860-2100 and northward from 90°S for the RCP4.5 simulations

A negative value in the cumulative plots indicates where the effect of climate has been to decrease the oceanic sink. The preponderance of negative values at 30°S illustrates the role of the Southern Ocean in establishing the climate impacts from figure 3.4(a).

Recent joint studies of ocean model simulations and atmospheric inversions introduced the hypothesis that changes in the Southern Ocean CO_2 uptake are already occurring (Le Quéré et al., 2007). They proposed that increases in the wind stress (positive SAM) over the Southern Ocean had decreased the uptake of CO_2 into the Southern Ocean by -0.08 Pg C yr^{-1} $decade^{-1}$ between 1981-2004 ($\sim$ -2 PgC total) relative to what the uptake would have been had there been no change to the ocean circulation. In situ observations support the hypothesis that surface carbon has been increasing (Metzl, 2009), though it is unclear whether that has been expressed as a decreasing flux (Majkut et al., 2014a). Evidence from CFC measurements suggests that the Southern Ocean has recently displayed substantial ventilation increases (Waugh et al., 2013).

Ocean biogeochemical models support the hypothesis that increasing winds have decreased CO_2 uptake, but show to varying extents that the mechanism is reduced by alkalinity driven solubility changes (Lovenduski et al., 2008) and enhanced biology (Dufour et al., 2013; Hauck et al., 2013) responding to increased upwelled nutrient levels (Le Quéré et al., 2010). Also, the coarse resolution used in these ocean modeling studies means that the predicted reduction of the carbon uptake may have been overestimated compared to models with improved eddy representation (or what we might expect in the real ocean) (Morrison and Hogg, 2012; Lovenduski et al., 2013; Dufour et al., 2013).

3.2 Float-based sampling experiment

Increased observational density in space and time should enhance our ability to monitor the Southern Ocean CO_2 uptake and constrain models of the processes that drive uptake and its response of global warming. A simple observational system simulation experiment (OSSE) is used here to evaluate the effectiveness of a float-based sampling program for estimating the basin-scale CO_2 flux in the Southern Ocean (>30°S) and monitoring it for trends and changes. The OSSE generates a synthetic sampling from model output and attempts to reconstruct the modeled fields from the simulated data.

The GFDL-ESM2M 'historical' simulation (years 1995-2000) (Dunne et al., 2012) is used as the 'true' case from which the synthetic sampling is produced. The sampling points are randomly distributed across the area of the Southern Ocean, south of 30°S (c.f. figure 3.5). The simulated floats do not move horizontally and sample the surface CO_2 flux from the model grid cell that they occupy monthly. The lack of horizontal movement, which should occur passively with the flow, may add some bias to the reconstruction, but the effect of movement in reconstructing physical parameters in other OSSEs has been quantified (Kamenkovich et al., 2011). The monthly sampling produces a set of 60 individual samples, X_i^{model}, for each of the N floats. N is 200 in the base case, as shown in figure 3.5, but a range of values from 100 to 500 is explored.

Random fluctuations are added to the direct samples, X_i^{model}, to model instrumental error and because the coarse resolution of the model grid and the monthly sampling do not represent the variability present in real point surface measurements. The sources of likely variability include: effects of mesoscale eddies, synoptic variability in the surface fields, analytical error in inverting the carbon system and instrumental error. The error is imposed by adding deviations to the sampled model values. The deviations are modeled as uncorrelated normal random variables with

standard deviations equal to a percentage of the true value, i.e. $std(X_i') = \epsilon X_i^{\text{model}}$. The synthetic samples include this fractional error, such that $X_i = X_i^{\text{model}} + X_i'$.

The scale of the error term, ϵ, that would be expected in real observations is not known. Estimates of the air-sea CO_2 flux from float data must involve an inversion of the surface carbonate chemistry to pCO_2, from two of pH, DIC and Alkalinity. Alkalinity can be estimated from diagnostic relationships with salinity, temperature and depth with reasonable precision ($\pm 8.4 \mu$mol kg^{-1}) (Lee et al., 2006). Low-power pH sensors, for deployment on floats and moorings, are currently in development (Johnson et al., 2009). Mooring-based instruments for pH have achieved estimates of pCO2, inverted using salinity-estimated alkalinity and pH measurements, of $\pm 13 \mu$atm over 2 month deployments, but suffer some drift (Cullison Gray et al., 2011). This work assumes that pH-instrumented floats will be available with similar precision and drift-correction in the near future. Given the coarse resolution of the model field, eddy effects would also need to be taken into account, though along track pCO_2 observations indicate that this is a small effect and adds an error of about 3 μatm (Lenton et al., 2006). While these sources of error should not be discounted, it is assumed that the gas exchange parameterization error will be dominant in achieving local flux estimates from point measurements. The expected precision of inverted pCO_2 and the effects of eddies would be between 1-3 % of an average Southern Ocean pCO_2 of 340 μatm; smaller than the uncertainties associated with gas exchange piston velocity (Takahashi et al., 2009a). Thus, a fractional sampling error of 20% is assumed for the base case presented here, which is the error associated with the parameterization associated with gas exchange. This level of error assumes that the other error sources are small and potentially compensating, but a range of percentage errors from 0 to 50% are explored to examine the robustness of the results to a range of inversion precisions.

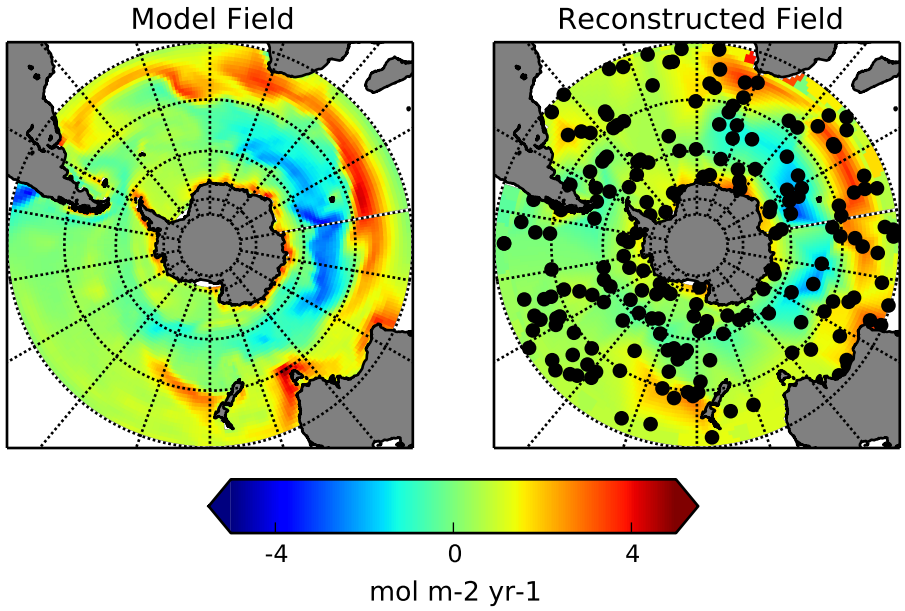

Figure 3.5: The modeled annual flux, in mole m^{-2} yr^{-1}, from the ESM2M historical simulation is shown as calculated (a) directly on the fully sampled model grid and (b) using 200 randomly distributed and stationary floats with a 20% sampling error. The true flux for the year was 0.79 PgC and the reconstruction shown here results in a flux of 0.76 PgC.

The simulated samples X_i are projected back onto the model grid using simple objective mapping with inverse distance scaling. The gridded values then constitute the reconstructed CO_2 flux for each month (c.f. figure 3.5(b)). The error induced by the mapping and carried though from the error added to the samples negatively affects the accuracy of the reconstructed CO_2 flux. The error in the basin-scale CO_2 uptake estimate is estimated via bootstrapping from a Monte Carlo simulation for each combination of (N, ϵ). The Monte Carlo simulation consists of 1000 simulated samplings, each with an individual distribution of the simulated floats. The error in the reconstructions is estimated using the standard deviation across the 1000 samplings.

The ability of the sampling strategies to capture trends in the basin-scale CO_2 flux is assessed using the bootstrapped error estimates and the autocorrelation in the time series of the modeled uptake. The calculation of the minimum amplitude detectable is carried out according to the relationship in equation 3.1 (Weatherhead et al., 1998), between the number of years of monthly estimates n, the error in the monthly estimates σ, and the lag-1 monthly autocorrelation in the time series ϕ.

$$\min|A| = \frac{3.3\sigma_N}{n^{3/2}}\sqrt{\frac{1+\phi}{1-\phi}} \tag{3.1}$$

This equation shows that the minimum detectable trend increases with the size of the noise in the data and with the level of monthly autocorrelation in the time series. The dependence on autocorrelation is quite important to this analysis, as it increases the time necessary to detect a trend of a certain magnitude. For a fixed period of observation, a moderate autocorrelation of $\phi = 0.5$ will increase the size of the minimum detectable trend by a factor of 1.73. The GFDL-ESM2M 'historical' simulation's Southern Ocean CO_2 annual uptake has an autocorrelation of 0.5. Thus, it plays an important part in evaluating the ability of the repeated observation to detect a trend. The bootstrapped error in the monthly reconstructions is also an important input for the trend detection.

3.2.1 Estimates

The reconstructed fluxes capture the total Southern Ocean uptake (south of 30° S) and the large-scale structures in the flux field. One example of the reconstructed flux, averaged for the year 2000, is shown in figure 3.5 for the base case sampling with 200 floats. While the sampling in the base case is still sparse, the reconstruction is capable of resolving many features of the flux field because of the zonal nature of the Southern Ocean and the large-scale features in the coarse-model flux field (Lenton et al., 2006).

In this subsection, we assess the skill of the reconstructed fluxes to capture the total uptake of CO_2 at the basin scale and the patterns of variability within the Southern Ocean.

Capturing the total uptake of CO_2 with high precision is an important task for constraining the global carbon budget. In the example shown in figure 3.5, the total uptake is 0.79 PgC yr^{-1}, which differs by 0.03 PgC yr^{-1} error from the true modeled value of 0.76 PgC yr^{-1}. Monte Carlo simulation provides context to the error in that instance. In a simulation with 1000 arrangements of the 200 floats, the bootstrapped error of the year-to-year estimates (measured by standard deviation) is 0.07 PgC yr^{-1}. The total uptake in the example is thus consistent with the true flux within the bootstrapped error estimate.

We find that the reconstructed fluxes capture the true value of the annual uptake within the bootstrapped precision for the 5 years of the considered simulation. The annual flux for the 5 years of reconstruction and the model are shown in figure 3.6(a). There, the $\pm 1\sigma$ range of the mean estimates (blue lines) contains the true annual values (black lines) from the model and separate the higher uptake in model years 1999 and 2000 from the earlier years. Thus, the base case sampling is capable of capturing the year-to-year Southern Ocean CO_2 uptake with enough precision to resolve interannual variability and constrain and monitor Southern Ocean CO_2 uptake.

The monthly estimates of the total CO_2 uptake from the float-based sampling also constrain the seasonal cycle in total uptake. The estimated error for the month to month fluxes is 0.1 PgC yr^{-1} and monthly reconstructions are also successful in capturing the monthly flux, within the $\pm 1\sigma$ bands, of the mean estimate from the Monte Carlo simulation (c.f. figure 3.6(b)). Note that the seasonal cycle in uptake south of 30° S, as shown in figure 3.6(b), is different from the region south of 45° S as was shown in figure 3.3. Though the simulated sampling retrieves the seasonal cycle in the smaller domain as well.

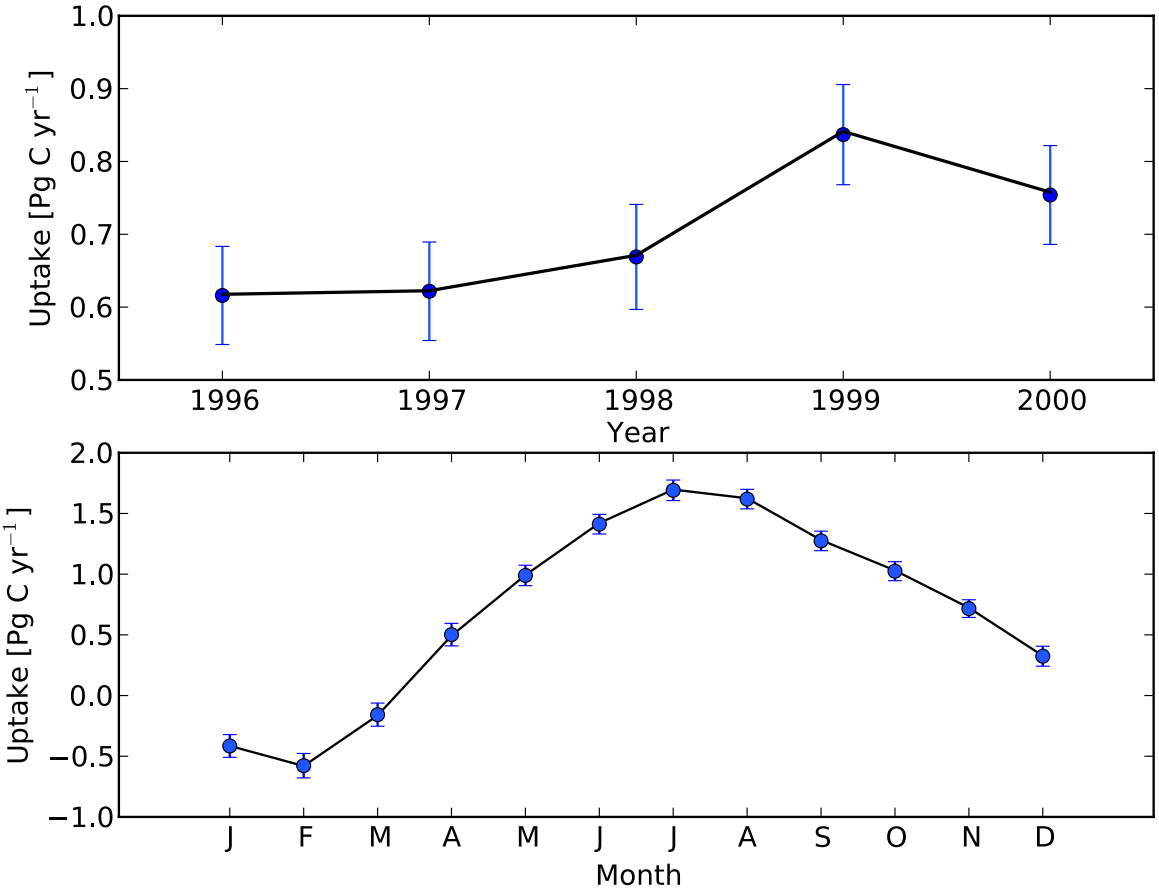

Figure 3.6: The annual reconstruction of the Southern Ocean CO_2 uptake, in PgC yr^{-1}, from the ESM2M historical simulation years over the period from 1996 to 2000 (top) and the averaged monthly uptake values for the 5 year reconstruction (bottom). The black line connects the true values of the flux. The blue bars show the $\pm 1\sigma$ uncertainty for each estimate, based on a 1000 member Monte Carlo simulation of 200 floats with 20% fractional sampling error.

3.2.2 Trend detection

The bootstrapped error for the monthly uptake estimate contributes to the calculation of the minimum detectable trend via equation 3.1. The calculation also relies on the lag-1 autocorrelation in the CO_2 uptake from the ESM2M simulation. The autocorrelation is set at the modeled value of 0.5 and the monthly error in the uptake estimate is 0.07 PgC yr^{-1}. The magnitude of the minimum detectable trend (90% significance level) is shown in figure 3.7. The magnitude of the minimum detectable trend decreases quickly with the number of years of continuous monthly observations and asymptotes toward very small trends after 40 years.

The detection of the trends associated with the continued uptake of CO_2 in the Southern Ocean and the response of the circulation to climate change from models is important. Based on the scenario projections from the CMIP5 simulations discussed in section 2, we can calculate that the uptake of continued CO_2 emissions to the atmosphere will drive an increasing trend in the Southern Ocean CO_2 uptake of 0.2 Pg C yr^{-1} $decade^{-1}$. Changes to that background trend, due to the potential impacts of climate change, have an unknown magnitude. Thus we focus on detecting a trend magnitude of the same size as the one associated with recent saturation of the Southern Ocean CO_2 sink, which is equivalent to a decadal change of -0.08 Pg C yr^{-1} $decade^{-1}$ (Le Quéré et al., 2007). Inverting the detection limits in figure 3.7, we find that the trend from continued growth of the Southern Ocean CO_2 sink would take 13 years to detect and the reduction due to climate would require 24 years of continuous monthly measurements.

3.2.3 Sensitivity Studies

The robustness of the reconstructions to the size of the sampling array and the error associated with the individual measurements is assessed via a sensitivity study. Here, the number of floats is varied between (50,500) and the percentage sampling error

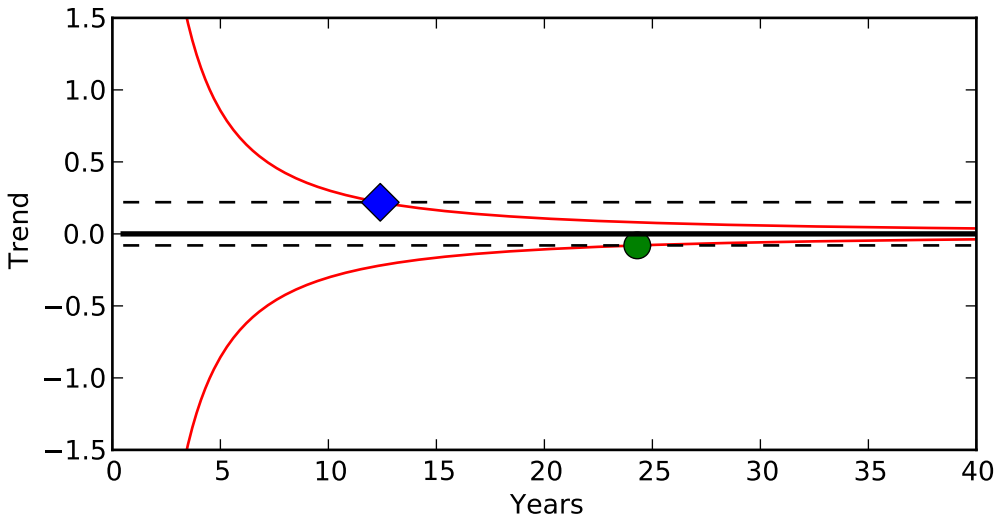

Figure 3.7: Minimum detectable trend (red lines), in Pg C yr^{-1} $decade^{-1}$, is a function of the number of years of monthly sampling, the error in the monthly estimates and the autocorrelation in the timeseries of uptake. Fifteen years of continuous monthly sampling are required to capture the historical trend associated with the uptake of anthropogenic CO_2 in the southern ocean (blue diamond, 0.2 Pg C yr^{-1} $decade^{-1}$). More than 20 years are required to capture a trend with the magnitude expected from changes in the overturning circulation (green circle, -0.08 Pg C yr^{-1} $decade^{-1}$).

varies over (0,50%). For each pair of parameters, we use the same method of simulating the observations as previously outlined and use a 1000 member Monte Carlo simulation to estimate the errors associated with the reconstruction process. The reconstructions are examined for both the total integral error, associated with uptake estimates for the Southern Ocean, and resolution of the local fluxes. For the latter, we measure the percent of reconstructed cells, on the GFDL ESM2M model grid, where the bootstrapped error estimate is larger than a threshold value of 1 mole m^{-2} yr^{-1}. The threshold level of 1 mole m^{-2} yr^{-1} is small enough to resolve the local seasonal cycle over 99% of the Southern Ocean area in the ESM2M simulation. The two measures evaluate the potential contribution of varying sampling arrays to monitoring Southern Ocean uptake and the flux variability within the Southern Ocean.

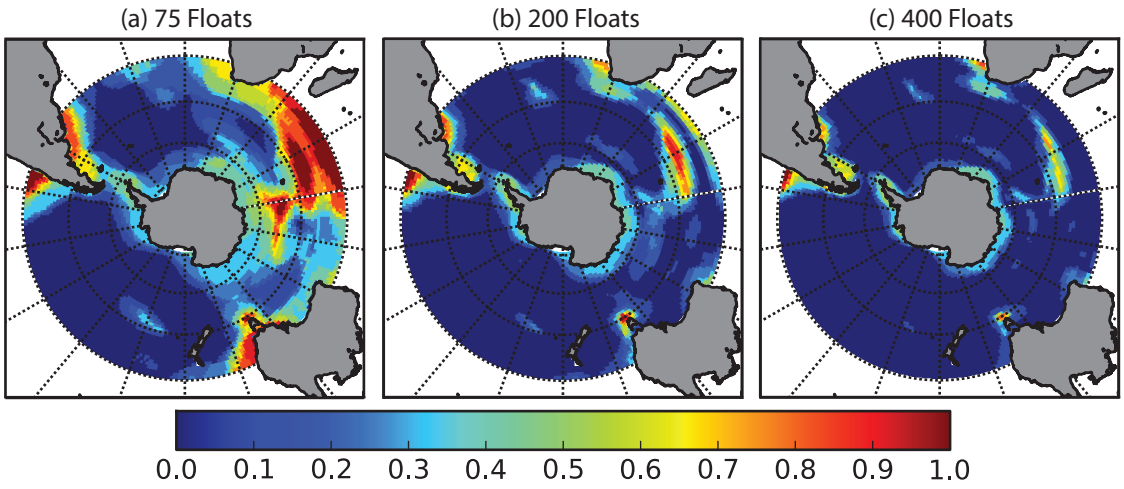

Figure 3.8: The proportion of months for which the bootstrapped error estimate is larger than the threshold value of 1 mole m^{-2} yr^{-1}. The area of exceedance decreases from samplings with 75 (top), 200 (middle) and 400 (bottom) floats. The bootstrapped errors come from the 1000 member Monte Carlo simulation for each number of floats.

We chose the percentage of exceedance as a metric of the fidelity of the reconstructions because it provides a basin-wide estimate of the ability of the reconstructed fluxes to recreate the spatio-temporal variability of the Southern Ocean CO_2 uptake. The fidelity of the reconstructions at the local scale will define their usefulness for examining the process-based questions which result in the high degree of uncertainty in the uptake estimates and projections. Examples of the exceedance percentage for float arrays with 75, 200 and 400 samplers indicate that large areas within the Southern Ocean will be resolved for the more moderate sampling (c.f. figure 3.8). Nevertheless, higher numbers of floats decreases the areas with error exceeding the threshold by nearly 20% of the Southern Ocean area. The high sampling cases leave only coastal and boundary regions where the precision of the reconstruction is above this threshold throughout the year.

The number of floats strongly influences the ability of the float-based sampling to capture both the integral error and the local fluxes with high precision. The estimated

error of the monthly basin uptake goes from more than 0.2 PgC yr^{-1} to less than 0.05 PgC yr^{-1} between 50 and 500 floats, with a strong drop off in the error estimate occurring before 200 floats (c.f figure 3.9). The same drop off is present in the percent area of exceedance. For the fractional sampling error of 20%, the area of exceedance falls from 34% to 9% between 50 and 200 floats. It falls to 4% with 500 floats. Again, the precent exceedance asymptotes with more floats such that there are diminishing returns for numbers of floats increasing beyond 200.

The sensitivity of the percent of exceedance to the scale of the sampling error is much larger than that for the total uptake. The curves in figure 3.9 show the integral error and percent exceedance against the number of floats. The low-high estimates for the percent exceedance are (30%,50%) for simulations with 50 floats and (4%,18%) for simulations with 500 floats (c.f. figure 3.9) for the fractional sampling errors that vary from 0 to 50% imposed error. In the case of integral error, the error estimates vary little with the scale of the sampling error compared to the difference across the number of floats. In contrast, the percentage area of exceedance is as sensitive to the fractional sampling error as it is to the number of floats over the ranges tested for each. The integral error is less sensitive to the fractional sampling error because the integral calculation sums over at least 50 samples of a normal random variable with zero mean, such that the summed error tends toward zero. The area of exceedance is harder to achieve with high fractional error because it is a summed measure of local error.

3.3 Discussion

The results from the OSSE presented here indicate that a float-based measurement system should be able to resolve the Southern Ocean CO_2 flux with a greater level of certainty than current methods. Current measurement density allows for a substantial

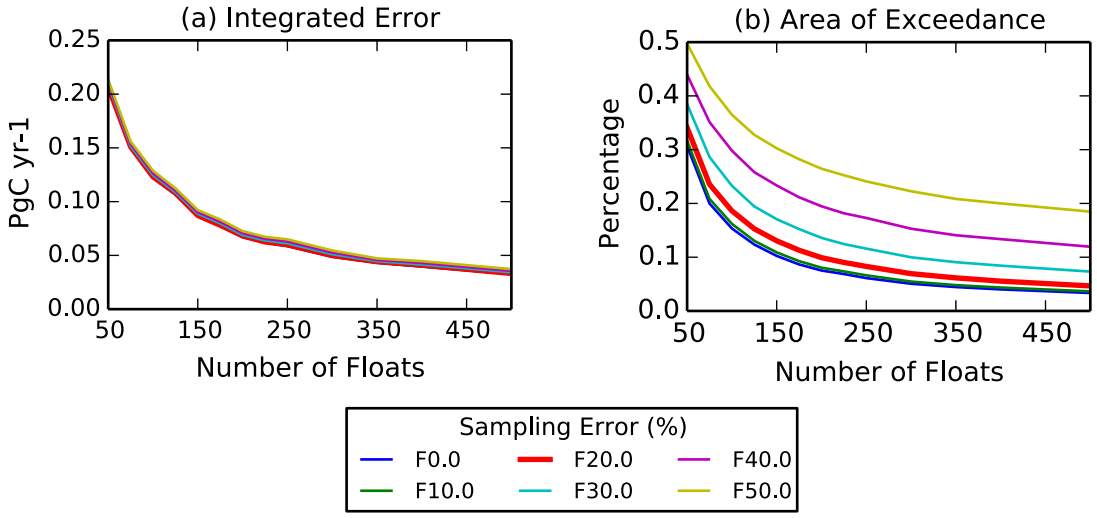

Figure 3.9: Error estimates for the annual reconstruction of the Southern Ocean CO_2 uptake, in PgC, for varying number of floats (left). The error estimates are calculated as the standard deviation of the basin-integrated annual CO_2 flux from the reconstructed fields and the true model. The percentage of the Southern Ocean, south of 30° S, where the monthly error estimate is larger than the threshold value of 1 mole m^{-2} yr^{-1} (right). In both plots, different lines reflect reconstructions with varying levels of sampling error. The error in the estimate of total uptake is less sensitive to the sampling error than the percentage of exceedance.

difference in decadal empirical estimates of the CO_2 uptake, 0.3 PgC yr^{-1}, with an even larger spread in model behavior (c.f. figure 3.2). Reducing the empirical uncertainty in the monthly and annual CO_2 flux to 0.07 and 0.1 PgC yr^{-1} should be possible with a float-based sampling at a scale of 150-200 floats. Such a system would be able to represent both the seasonal cycle and the annual mean uptake, which would provide a major constraint for atmospheric inversions (Lenton et al., 2013) and studies of the ocean's role in the global carbon cycle (Wanninkhof et al., 2013).

Previous studies have considered the number of surface measurements that are necessary to capture the CO_2 flux at monthly and annual scales. Samplings with a density of 3° latitude and 30° longitude have been proposed as sufficient to resolve the annual Southern Ocean uptake (Lenton et al., 2006). Such a sampling density is similar to the base case that we investigated, with a density of 1 float per 95 square

degrees on the ESM2M model grid. This study shows that even when the floats are randomly distributed, the monthly uptake is largely resolved with between 150-200 samplers with continued improvements for ever more floats. This is most likely a result of the average decorrelation length scale in the coarse resolution models being resolved with 150-200 samplers (Lenton et al., 2006). It is still unknown how well the coarse ocean model that forms the basis of this study resolves the statistics and dependencies of the CO_2 flux from the real ocean. Similar studies with high resolution models might provide some additional information about the scales of variability that the floats must sample to generate suitable flux reconstructions. Future studies with high resolution models might also give some indication of the actual size of the fractional sampling error due to variability that is not resolved by the 1 degree model that we employed and provide benchmarks for the statistical upscaling of sub-grid scale variability.

The ability to capture trends in the CO_2 uptake in the Southern Ocean is limited by the error in the monthly estimates of the uptake, the month-to-month variability and the autocorrelation in the time series of uptake. The increased uptake from increasing atmospheric CO_2 will take a decade or slightly more to detect. The time to capture departures from such an expected trend, from changes associated with climate change, for instance, will take decades or more. Directly detecting changes in the Southern Ocean CO_2 uptake, like the decrease of -0.08 PgC yr^{-1} $decade^{-1}$ associated with changes in wind stress (Le Quéré et al., 2007), will take up to 3 decades. The smaller changes expected from reduced future uptake in the CMIP5-type models (-0.02 PgC yr^{-1} $decade^{-1}$, c.f. figure 3.4(c)) will require 60 or more years of continuous observations. While the changes to the carbon uptake that are currently projected are hard to detect, mainly due to the effects of monthly autocorrelation and variability, an updating flux estimate will provide some ability to measure large,

unexpected, changes to the CO_2 uptake at the decadal scale (up to 0.3 PgC yr^{-1} $decade^{-1}$ or half of the current uptake).

The synthetic sampling that we present here is an idealized case, which was meant to show how many measurements and what precision of measurement was needed to understand seasonal and year-to-year variations in the Southern Ocean CO_2 uptake. Continued effort should be expended to evaluate float-based sampling strategies within data assimilation frameworks and OSSEs such as this one. Critically, transport of the floats by the mean flow and eddies may affect the basin-scale monitoring of CO_2 uptake and may invalidate the assumption of a random distribution that we have used. In a high-resolution OSSE, the strong currents of the Southern Ocean affected the sampling distribution of floats in the Indian Ocean (Vecchi and Harrison, 2007). While eddies enforce a more uniform sampling distribution (Kamenkovich et al., 2011), strategies for float release, parking depth, time between profiles and ice-avoidance will need to be critically evaluated for how they impact the information provided by the whole sampling array and target undersampled regions.

3.4 Conclusions

Empirical and model estimates indicate that the flux of CO_2 in the Southern Ocean is critical to the global carbon budget. Up to 50% of the anthropogenic CO_2 that is absorbed by the ocean is captured within the Southern Ocean. Moreover, a significant portion of the uncertainty in estimates of the global oceanic CO_2 uptake originates in the Southern Ocean, south of 30° S. This is true for both empirical and model-based estimates, where empirical estimates are limited by the lack of available data in the Southern Ocean and model estimates show significant differences across models at the process level. Increased observational density is necessary to resolve the uncertainty in

the Southern Ocean CO_2 uptake and the process-level understanding of the dynamics which govern the Southern Ocean CO_2 flux.

We have shown that an observational program based on 150-200 vertically profiling floats that could estimate surface CO_2 flux, would offer significantly more information about the Southern Ocean CO_2 uptake than is currently available on monthly, annual and interannual timescales. Such a system would provide annual estimates of the Southern Ocean uptake with an error of less than 0.1 PgC yr^{-1} or less than 20% of the current uptake in the Southern Ocean or 5% of global oceanic uptake. This would be an important tool for monitoring the uptake of anthropogenic CO_2 by the ocean and understanding and monitoring the global carbon budget. This is particularly important for the Southern Ocean, where changes in the flux due to the effects of climate change could be a significant portion of the carbon cycle's response to climate change.

Moreover, an observational program featuring 150-200 sampling floats would provide much higher resolution of the CO_2 flux at local and monthly scales. For an assumed threshold of 1 mole m^{-2} yr^{-1} (to capture more than 90% of the seasonal cycle), this system will offer resolution of the CO_2 flux over 90% of the Southern Ocean every year. This resolution will provide an opportunity to dramatically improve process-based understanding of the Southern Ocean CO_2 flux to help address the balances between gas exchange, biological uptake, upwelling and entrainment and detrainment at the base of the mixed layer. By offering dense information at the ocean surface, it would provide an important complement to monitoring strategies based on repeat hydrographic monitoring of carbon accumulation in the ocean interior. Those studies could provide a benchmark against which the carbon uptake inferred from the float array measurements could be evaluated.

This study has focused on the uncertainty in and constraints for the Southern Ocean CO_2 flux. The array network considered here could serve as a critical com-

ponent of a larger integrated network, wherein the floats could be equipped to measure nutrients, temperature, salinity and other biogeochemically important quantities. Profiling floats are specifically valuable because they measure the water column to 2000 meters and provide information for subsurface studies. The spatially diffuse and temporally consistent measurements from these floats could provide a bridge between sparse, high precision, hydrographic measurements and very high resolution satellite products to develop an integrated understanding of Southern Ocean biogeochemistry at many time scales. Ongoing work is devoted toward achieving such a monitoring system(Meredith et al., 2013; Rintoul et al., 2012). In the same way that 150-200 floats measuring surface CO_2 could dramatically improve our understanding of the CO_2 flux, these measurements could contribute to understanding and monitoring other aspects of the biogeochemical system in the Southern Ocean, which is critical to the global cycling of nutrients and the capture of excess heat due to climate change by the ocean. Much more than being a tool for CO_2 monitoring, measurements of this scale and nature would offer significant opportunity to monitor and understand the Southern Ocean's role in an evolving ocean.

Chapter 4

Carbon System Feedbacks and Climate Policy

4.1 Introduction

The development of the modern economy has changed the earth's climate system. Economic development has added CO_2 to the atmosphere, primarily by burning fossil fuels for energy and clearing land for agriculture (Le Quéré et al., 2014). Additional CO_2 positively increases the radiative balance of the atmosphere and drives global warming (Callendar, 1938). Social planners and economists expect this warming will result in negative health, environmental and economic consequences (Tol, 2011). The negative consequences associated with warming – present and future – have spurred policymakers and analysts to develop strategies to reduce CO_2 emissions in the 21st century.

One tool for designing policies to manage the risks of climate change is an integrated assessment model (IAM), a model framework coupling representations of the earth system, economic growth and social well-being. IAMs can be used to understand the time-lagged damages of CO_2 emissions on present and future well-being.

For example, IAMs are commonly used to estimate the expected economic damages from a marginal tonne of CO_2 emissions, a quantity known as the Social Cost of Carbon (SCC). Such costs are presently included in regulatory analysis in the United States (EPA, 2014). IAMs can also use a price model for emissions reductions to develop mitigation strategies which optimize the balance between the present costs of mitigation and reduced future damages (Nordhaus, 1992).

The predicted costs of climate change within an IAM depends on the joint parameterization of the physical and economic systems. The SCC or optimal mitigation is sensitive to the assumptions made about social preferences for social discounting (Stern et al., 2006; Nordhaus, 2007), intragenerational equity (Anthoff et al., 2011), economic damages as a function of warming (Kopp et al., 2012), and risk aversion (Dietz, 2012). So too, the costs of CO_2 emissions and benefits of mitigation depend on physical parameterizations of atmospheric radiative balance and the global carbon cycle's response to emissions (Hof et al., 2012). Where damages and social factors are held constant, a stronger or more prolonged warming response to emissions will raise the SCC and increase optimal levels of mitigation.

Studies across IAMs with difference climate and carbon cycle parameterizations have shown that the representation of the climate and carbon systems significantly affects estimates of the SCC and mitigation benefits (van Vuuren et al., 2011; Hof et al., 2012). Across IAMs, there is a larger dependence on the parameterization of the physical climate than the carbon cycle (van Vuuren et al., 2011). However, we focus this study on the parameterization of the carbon cycle. Both are important inputs to decision making, but the effects of the parameterization of climate sensitivity have been more thoroughly studied and are already included in some regulatory considerations (Interagency Working Group on the Social Cost of Carbon, 2010). This study is motivated by the significant uncertainty in model predictions of the global carbon cycle with the most advanced versions of earth system models, for example

those included in the CMIP5 set of simulations (Friedlingstein et al., 2013), and recent indications that the efficiency of the natural carbon sinks may be changing under the effects of climate change (Raupach et al., 2013).

Currently, the land biosphere and oceans remove an amount of excess CO_2 from that atmosphere equivalent to about 50% of annual emissions from anthropogenic activity (Le Quéré et al., 2014). The percentage of annual emissions taken up by the natural carbon sinks is expected to decrease in the future, because of changes to biochemistry and ocean chemistry under higher atmospheric CO_2 and changes in atmospheric and oceanic temperatures (Raupach, 2013). Those changes are referred to as concentration-carbon and climate-carbon feedbacks; they add substantial uncertainty to model predictions of climate change due to CO_2 emissions. In emissions scenario simulations performed with earth system models, carbon cycle feedbacks add up to 1°C of additional warming under high CO_2 forcing (Friedlingstein et al., 2006). Under the high emissions scenario RCP8.5, the carbon cycle feedbacks in earth system models add 100 ppm to uncertainties in predicted atmospheric CO_2 concentrations (Friedlingstein et al., 2013). In earth system models, the largest uncertainties in the carbon cycle feedbacks are the extent to which increased atmospheric CO_2 will enhance growth and carbon storage in the land biosphere, how the land carbon stocks will respond to warming and the rate at which CO_2 is absorbed by the ocean (Arora et al., 2013). Understanding the implications for these uncertain feedbacks in an integrated assessment framework is our primary goal.

We adopt a simple model of the atmosphere-land-ocean carbon balance that permits us to examine the uncertainty in the carbon cycle feedbacks by treating select model parameters as uncertain in Monte Carlo simulations. We define probability distributions for these parameters to emulate the range of carbon cycle feedbacks present in earth system models (Arora et al., 2013). We then use Bayesian inversion to estimate distributions for the model parameters that are consistent with currently

available measurements of the global carbon cycle. In particular, we show how the assumed history of CO_2 emissions from land use change (LUC) critically impacts estimates of the strength of the land CO_2 sink via CO_2 fertilzation (Shevliakova et al., 2013). By using two distinct estimates of LUC emissions, we develop two parameterizations of the carbon system, where one has a much more robust CO_2 fertilization effect and significantly lower predictions of atmospheric CO_2 for a given emissions pathway. We compare the IAM outcomes conditional on the LUC case and combine the parameter sets to report a measure of total uncertainty in future CO_2 predictions.

Previous studies have used similar data-constrained carbon models to assess the impact of carbon cycle uncertainty on CO_2 emissions pathways necessary to stabilize atmospheric CO_2 (Ricciuto et al., 2008) or to make probabilistic predictions of CO_2 concentrations and warming under fixed emissions scenarios (Bodman et al., 2013). This study builds on these previous efforts by assessing the impacts of carbon cycle uncertainty on the output of an IAM and considering the impact that reductions in uncertainty might have on the efficiency of optimal policies. We simulate the narrowing of uncertainty in future predictions by conditioning our projections on LUC history. Where previous studies have looked at the effect of carbon cycle parameterization across IAMs (van Vuuren et al., 2011; Hof et al., 2012), examining the effect of parameter uncertainty in one model allows us to look at the impacts of physical processes on IAM outcomes and particularly highlight the importance of CO_2 fertilization of the land-biosphere.

4.2 Model Formulation

To design climate policy, the decision maker needs an IAM that couples credible models of (1) the carbon cycle, (2) the energy balance of the atmosphere and ocean, and (3) economic growth. In the following sections, we describe the model that we

use to study the range of possible carbon cycle feedbacks to climate change. The carbon cycle model derivation closely follows that of the Simple Carbon Climate Model (SCCM) (Raupach et al., 2011; Raupach, 2013) and is functionally similar to other globally aggregated models of the atmosphere-land-ocean carbon balance such as the BERN carbon cycle model (Joos et al., 1996) or MAGICC-6 (Meinshausen et al., 2011a). Differences from the SCCM are highlighted, but most notably, the SCCM is a more complete model that includes forcing terms from greenhouse gases other than CO_2 and its own energy balance model. We vary select parameters in this carbon model in Monte Carlo simulations to represent parametric uncertainty and simulate learning. We also couple the simple carbon model to the economic and energy balance models from the 2013-R vintage of the classic IAM, DICE (Nordhaus, 2014).

4.2.1 Carbon Cycle Model

The atmospheric inventory of CO_2 above preindustrial C_a is controlled by the emissions of fossil fuel carbon E, emissions associated with land use change E_{luc} and the air-land f_l and air-sea f_o fluxes.

$$\frac{d}{dt}C_a = E + E_{\text{luc}} + f_l + f_o \tag{4.1}$$

Emissions are prescribed from historical records or by the economic module from DICE, while the flux terms are calculated endogenously. The stocks of carbon are in units of GtC. All fluxes are rates in GtC yr^{-1} and signed such that positive fluxes contribute to increasing atmospheric CO_2. Parameter values from the literature are shown in table 4.6.

Ocean Uptake

The ocean uptake flux is calculated using a pulse response model, where excess anthropogenic CO_2 enters the surface ocean from the atmosphere and is then exported into the deep ocean over multiple timescales. This is an approximation to models of CO_2 uptake that explicitly simulate the ocean circulation (Maier-Reimer and Hasselmann, 1987). The sea-air flux f_o is a function of the disequilibrium between the partial pressure in the atmosphere pCO_2^a and the surface ocean pCO_2^o and a gas exchange piston velocity k_g.

$$f_o = k_g(pCO_2^o - pCO_2^a) \tag{4.2}$$

The flux at the air-sea interface is partitioned into four carbon stocks within the surface ocean C_{mi} and then exported to the deep ocean stock C_d. The four carbon stocks do not mix. The export rates k_{mi} are fit, along with the fractionation α_{mi} constants, to reflect the response of more advanced models (Joos et al., 1996). The fractionation within the surface ocean carbon stocks is complete, $\sum \alpha_{mi} = 1$, and all export from the surface accumulates in the deep ocean stock.

$$\frac{d}{dt}C_{mi} = -\alpha_{mi} f_o - k_{mi} C_{mi} \tag{4.3}$$

$$\frac{d}{dt}C_d = \sum_i k_{mi} C_{mi} \tag{4.4}$$

The total dissolved inorganic carbon at the surface is calculated as the sum of the preindustrial value and the total perturbation carbon in the four surface stocks. The total DIC is then used to calculate the surface partial pressure for the flux calculation. The partial pressure of CO_2 in the ocean is approximated from the absolute oceanic surface temperature and the perturbation of the mixed layer carbon

content using a high-order polynomial approximation of the surface ocean carbonate chemistry (Harman et al., 2011).

Land Carbon

The land carbon system represents the carbon stock in the terrestrial biosphere and the exchange of CO_2 between the atmosphere and land via photosynthesis, respiration and exogenous land use change. Total land carbon is represented by two stocks C_{Li}. The annual accumulation of carbon in the land stocks is modeled as net primary production, NPP. NPP is distributed between the land stocks fractionally α_{Li} and completely, such that $\sum_i \alpha_{Li} = 1$. Each land carbon stock respires to the atmosphere with a temperature-dependent rate constant k_{Li}.

$$\frac{d}{dt}C_{L1} = \alpha_{L1}NPP - k_{L1}C_{L1} \tag{4.5}$$

$$\frac{d}{dt}C_{L2} = \alpha_{L2}NPP - k_{L2}C_{L2} - E_{\text{luc}} \tag{4.6}$$

The respiration rates k_{Li} depend on a q_{10} relationship with temperature above the preindustrial mean, $k_{Li} = q_{10}^{\Delta T/10} k_{Li}^0$. The base respiration rates of the two stocks differ by two orders of magnitude (cf table 4.6) giving a small and fast response stock C_{L1} (leaves and grasses) and a large and slow response stock C_{L2} (trees and soils). Deforestation removes carbon from the slow respiration stock.

The net primary production NPP is a function of excess atmospheric CO_2 and a volcanic aerosol index VAI (Ammann et al., 2003).

$$NPP = NPP_0 \left(1 + (m_{NPP} - 1)\frac{C_a}{(C_a^p + C_{NPP}^p)^{1/p}}\right)(1 + 0.5 * VAI) \tag{4.7}$$

The functional dependence of NPP on excess atmospheric CO_2 concentration C_a provides the CO_2 fertilization effect. In this model, NPP grows with increases of atmospheric CO_2 and saturates at a multiplicative factor m_{NPP}, where $m_{NPP} \geq 1$.

The rate of increase toward saturation is set by two shape parameters p and C_{NPP}. For small perturbations of atmospheric CO_2, the fertilization factor is approximately linear $\sim (C_a/C_{NPP})$, where $C_{NPP} = 687$ GtC. The value of $p = 2.5$ determines how quickly the CO_2 fertilization factor approaches the saturation level. These factors are held at their prescribed values from the SCCM, where they were set to fit present day conditions. While NPP has been shown to have some temperature dependence regionally, NPP is not clearly related to temperature at the global aggregate scale or across the range of temperatures that we will simulate in future conditions (Piao et al., 2013; Ricciuto et al., 2008; Friedlingstein et al., 2006). We omit temperature dependence of NPP in this global aggregate model.

The volcanic aerosol index, VAI, is an important consideration for historical runs as volcanic activity has been shown to have a significant impact on land CO_2 uptake rates from 1959-2012 (Raupach et al., 2013). Large volcanic eruptions serve to temporarily increase CO_2 uptake by the land. Some of the increase comes from reduced tropical respiration with post-eruption cooling, but increasing diffusion of solar irradiance can increase productivity (Jones and Cox, 2001). The effect of recent large volcanic eruptions (e.g. El Chichon and Pinatubo) on atmospheric CO_2 can bias the statistical significance of inferred trends in the land sink (Frölicher et al., 2013). Thus we include the stimulation of production by volcanic aerosols in our hindcasts and parameter estimations.

4.2.2 Energy Balance

Future temperature changes are calculated with the energy balance model from DICE2013. It employs a two-box model for the energy balance of the joint atmosphere-upper ocean and the deep ocean, with respective temperature increases T and T_o in °C above preindustrial. Excess CO_2 increases radiative forcing following

a logarithmic function.

$$C\frac{d}{dt}T = F - \gamma T - \beta(T - T_o) \tag{4.8}$$

$$C_o\frac{d}{dt}T_o = \beta(T - T_o) \tag{4.9}$$

$$F = 5.35\log\left(\frac{C_a + C_a^0}{C_a^0}\right) \tag{4.10}$$

This model is primarily parameterized in terms of the equilibrium climate sensitivity, the warming that occurs with a doubling of preindustrial atmospheric CO_2, $T_{2x} = F_{2x}/\gamma$. This model is set to an equilibrium climate sensitivity of 2.9°C, inferred from the IPCC's 5th assessment report. The transfer coefficient β and the heat capacities of the upper and lower ocean C and C_o are inferred from simulations with global climate models (Nordhaus, 2014).

4.2.3 Economic Factors

DICE represents a single decision maker evaluating the costs of climate change and mitigation efforts for the next 300 years using a globally aggregated model of economic growth and damages. Within DICE, economic growth is modeled using a Ramsey growth model (Ramsey, 1928), that uses a Cobbs-Douglas production equation to convert capital resources and labor (population) into economic output, Y in 2005 \$ yr^{-1}, and then divides that output into consumption of economic goods and reinvestment into the capital resources with savings rate s, (Investment, $I = sY$; Consumption, $C = (1 - s)Y$). Many of the factors that go into the economic model are exogenous, including population growth. (Nordhaus, 2014). In this section, time is in years and discrete and variable dependence on time is subscript t.

In DICE, economic activity generates CO_2 emissions. The emissions rate is proportional to the gross output and includes a carbon output factor σ, that decreases exogenously with time, and the emissions control rate m which is the fraction of emis-

sions for which the decision maker is willing to pay to prevent. The cost to prevent emissions starts high and decreases with time.

$$E_t = \sigma(1 - m_t)Y_t + E_{\text{land},t} \tag{4.11}$$

The CO_2 emissions generated by economic output, and land use change, are input to the carbon cycle model. The land use change emissions in DICE2013 are specified as 3.3 GtC yr−1 in 2010 and decrease at a rate of 20% per decade in the standard DICE scenario.

The climate warming due to emissions decreases economic output by a fractional damage factor, which goes as a power of degrees of temperature change.

$$D \sim d_1 T^{d_2} \tag{4.12}$$

The damage function is transformed to avoid damages larger than output, such that the net output is decreased by a factor $\Omega = (1 - D/(1 + D))$. In the standard version of DICE2013, $d_2 = 2$ and $d_1 = 0.27\%^{\circ}C^{-2}$, such that damages equal 2.4% of economic output at 3° C of warming. We additionally report values for a cubic damage function ($d_1 = 0.09\%$ °C^{-3}, $d_2 = 3$). The cubic damage coefficient is calibrated to harmonize the two damage functions at 1.5 °C. We include the cubic damage function in the calculations because the shape of the damage function at high temperatures is a significant uncertainty for impact analysis, with several authors advocating higher powers for the temperature dependence of damages (Kopp et al., 2012), and previous work has shown that SCC values are more sensitive to carbon cycle feedbacks at higher damage scalings (Kopp and Mignone, 2013).

The decision maker controls the savings rate and the emissions mitigation rate to maximize the expected welfare of the world. Given a policy decision m, the social welfare function in DICE is the sum of a time-discounted instantaneous social utility

function of per capita consumption, c_t, the population L_t and ρ the pure rate of time preference, a discounting rate on units of social utility.

$$W = \max_m \sum_t U[c_t(m)]L_t(1+\rho)^{-t}. \tag{4.13}$$

The utility function is a function of per capita consumption, $U \sim c_t^{1-\eta}/(1-\eta)$, where η is the elasticity of marginal consumption. Since warming decreases economic output, welfare depends on the evolution of the carbon cycle and atmospheric energy balance under a given policy or emissions path. Given our interest in uncertainty, we consider policies that maximize the expected welfare over the possible states of the world λ_i given a probability distribution represented by probabilities $p(\lambda)$ (for the remainder of the chapter, λ is used to symbolize a generic set of model parameters). In this case, the policy m should maximize the expected welfare given the uncertainty in the state of the world.

$$EW[\cdot|p(\lambda)] = \max_m \sum_i p(\lambda_i) \sum_t U[c_t(m,\lambda_i)]L_t(1+\rho)^{-t}. \tag{4.14}$$

A key question for our analysis is how the different representations of the uncertainty in the carbon cycle feedbacks affect the expected welfare in the future and the policy decision, m, that maximizes the expected welfare under present levels of uncertainty. As a specific example, we consider how the level of belief in each of the LUC cases would affect the choice of policy and the expected welfare for the decision maker.

In addition to the parameters of the energy balance and carbon cycle models, welfare depends on two social parameters, ρ and η. These parameters represent the social judgements of the decision maker toward discounting utility and equivalent levels of consumption through time. These parameters strongly affect the expected welfare of any given decision, because changes to the climate are lagged with respect to emissions and benefits from mitigation are accrued after the costs of mitigation

are borne. DICE2013-R uses $\rho = 0.015$ and $\eta = 1.45$ as its central case. This set of parameters gives an average discount rate on consumption of approximately 4.5% through 2100, which reflects a globally aggregated return rate on capital investments (Nordhaus, 2014). The positive η also introduces some risk aversion, a preference to avoid the worst possible outcomes (for a discussion on risk avoidance in a Ramsey Growth Model, see refs. Kopp and Mignone (2012) and Kousky et al. (2011)). The pure rate of time preference will be varied in some experiments to show how the social preferences of the decision maker affect the implications of the carbon cycle feedbacks.

4.3 Parameter Estimation via MCMC

The parameters of our simple carbon model can be varied systematically to simulate the uncertainty in the carbon cycle feedbacks for a larger set of models earth system models, such as the those in CMIP5. In this section, we adopt the Bayesian framework for learning about a small set of parameters for our carbon model, using data-based estimates of the global CO_2 balance to constrain their joint probability distribution function. We perform the inversion using Markov Chain Monte Carlo (MCMC) sampling with a Metropolis-Hastings decision criteria (Hastings, 1970; Metropolis et al., 1953). This method has previously been used to constrain carbon cycle models similar to the one under consideration here, with different observational constraints and assumptions (Ricciuto et al., 2008; Bodman et al., 2013). This study differs from previous work by adding a time history of ocean uptake flux as an observational constraint (Majkut et al., 2014a), using prior distributional estimates inverted from the CMIP5 suite of Earth System Models and assuming two land use emissions histories.

4.3.1 Emulating Earth System Models

There is always an ambiguity in selecting appropriate model parameters and the associated prior probability distributions for bayesian inversions such as this one. Here, we selected four parameters from the carbon model to treat as uncertain and invert with observations, (m_{NPP},q_{10},k_{m2},k_{m3}). This choice allows us to keep the number of parameters subject to uncertainty to a minimum and still emulate the range of carbon cycle feedbacks that are present in earth system models.

The prior probability distribution functions for each invertible parameter were designed to fit the linear carbon-concentration and carbon-climate feedback metrics from the CMIP5 suite of earth system models (Arora et al., 2013). The linear feedback metrics measure the response of the land and ocean sinks to increasing atmospheric CO_2 and to increasing atmospheric temperature separately, using sensitivity simulations. In these simulations, the carbon system is initially in equilibrium, with atmospheric CO_2 at the preindustrial value of 278 ppm. Atmospheric CO_2 concentration then increases at 1% per year until the preindustrial value is quadrupled.

In one simulation, the increasing atmospheric CO_2 affects the land and ocean carbon sinks but does not affect the radiative balance of the atmosphere. This biogeochemically-coupled simulation allows us to estimate the linear carbon-concentration feedback parameters (β_L,β_O) as the quotient of the land and ocean carbon uptake at the end of the simulation (ΔC_L,ΔC_O in GtC) and the change in atmospheric CO_2 in ppm. The concentration-carbon feedback parameter has units GtC ppm^{-1}, with higher values for model parameterizations with high uptake and low climate sensitivity to CO_2 emissions. We calculate the feedback parameters from the cumulative flux difference at the end of the simulation as in Friedlingstein et al.

(2006).

$$\beta_L = \Delta C_L/(2.13\Delta C_a) \tag{4.15}$$

$$\beta_O = \Delta C_O/(2.13\Delta C_a) \tag{4.16}$$

The concentration-carbon feedback on land β_L is controlled by m_{NPP} in our model. We assign a right-shifted prior probability distribution for $m_{NPP} \sim 1 + W(2.4, 0.58)$, where $W(\alpha, \beta)$ is the Weibull distribution with shape parameter α and scale parameter β. Under this prior, the statistics of β_L in the simple model match those calculated for the CMIP5 models (Arora et al., 2013), shown in table 4.1. The right-shifted distribution ensures $m_{NPP} > 1$.

The concentration-carbon feedback for the ocean β_O depends jointly on the ocean export timescales, k_{m1} and k_{m2}. These are positive by definition, so we assign them Weibull prior distributions, $k_{m1} \sim W(2.8, 0.31)$ and $k_{m2} \sim W(2.8, 0.013)$. The prior distributions are *a priori* independent and under sampling recreate the statistics of β_O from the CMIP5 models (see table 4.1). With the different prior scale parameters, the values of k_{m1} are an order of magnitude larger than k_{m2}, such that they respectively control uptake on sub-decadal and multi-decadal timescales.

In a second simulation, the increasing atmospheric CO_2 increases atmospheric temperature, but the NPP and ocean flux calculations are forced with the preindustrial CO_2 concentration. Thus, changes in the land and ocean carbon stocks at the end of the warming run (ΔC_L^T,ΔC_O^T in GtC) show the sensitivity of the carbon cycle to temperature increases, normalized by the increase in atmospheric temperature at 4x preindustrial CO_2, ΔT. The carbon-climate feedback parameters (γ_L,γ_O) have units GtC $^\circ C^{-1}$, with negative values indicating a positive feedback for climate

change.

$$\gamma_L = \Delta C_L^T / \Delta T \tag{4.17}$$

$$\gamma_O = \Delta C_O^T / \Delta T \tag{4.18}$$

The carbon-climate feedback on land in controlled by q_{10} in our model. We assign the prior $q_{10} \sim 1 + W(1.79, 0.76)$ to recreate the statistics of γ_L from CMIP5 (see table 4.1). The right-shifted distribution reflects our assumption that increasing atmospheric temperature will increase the respiration rate from the land carbon stocks. The model that we use does not permit uncertainty in the ocean climate-carbon feedback, as it cannot represent changes to ocean circulation or the depth of the mixed layer, like the CMIP5 earth system models (Arora et al., 2013). Instead, the warming of the mixed layer decreases CO_2 solubility in our model and drives flux from ocean to atmosphere, leading to a negative carbon-climate feedback. The ocean carbon-climate feedback in our simple model is stronger than the mean from the CMIP5 earth system models (see table 4.1) (Arora et al., 2013), but is similar to the previous generation of earth system models Friedlingstein et al. (2006).

4.3.2 MCMC Inversion

We use four sources of information to constrain the parameters of the uncertain carbon model. They are either direct observations or observationally-based estimates of: (1) the annually-averaged atmospheric CO_2 concentration measured at the Mauna Loa CO_2 observatory from 1959-2012 (Keeling et al. (2001),download: www.esrl.noaa.gov/gmd/ccgg/trends/) , (2) the estimated atmospheric concentration of CO_2 from the Law Dome Ice Cores from 1860-1959 (Etheridge et al., 1998) (3) the ocean uptake flux of anthropogenic CO_2 from 1980-2009, estimated from surface pCO_2 inversion (Majkut et al., 2014a), and (4) the oceanic inventory of anthropogenic CO_2

from 1995 estimated from hydrographic measurements (Sabine et al., 2004; Khatiwala et al., 2009).

The MCMC generates a sampling of the posterior distribution of (m_{NPP},q_{10},k_{m2},k_{m3}) by iteratively occupying points in parameter space and then accepting randomly generated proposal steps by applying the metropolis rule. The metropolis rule says that from a given point in parameter space λ, the proposed step $\Delta\lambda$ will be accepted with probability α based on the ratio of the likelihood and prior probability for the current position and the proposed step.

$$\alpha = \min\left\{1, \frac{L[\mathbf{y}|\lambda+\Delta\lambda]p(\lambda+\Delta\lambda)}{L[\mathbf{y}|\lambda]p(\lambda)}\right\} \tag{4.19}$$

If the product of the likelihood and prior probability associated with the new position, $\lambda+\Delta\lambda$, is greater than the product at the current position, then the step is accepted. If the product is less than at the current position, meaning less likely considering the constraints or less likely in the prior estimate, then the step is accepted with probability α. Under this decision criterion, the random walk moves toward areas of the parameter space that are likely in the prior estimate and constant with the observational constraints. Under the Metropolis-Hastings decision criteria, the positions of the random walk eventually converge to a sampling of the posterior distribution for the parameters given the observational constraints.

Since the MCMC sampling depends on calculating the relative likelihood between different points in parameter space, the treatment of the error associated with the observational constraints is critical to the final estimates. The error for the Law Dome CO_2 estimates and the two estimates of the oceanic inventory of anthropogenic CO_2 are treated as normal and independently distributed random variables. Each Law Dome measurement is assigned an error with standard deviation of 10 ppm, higher than the estimates associated with the analytical technique (Etheridge et al.,

1998). This high level of uncertainty reflects our impression that the age model associated with the measurements provides substantial uncertainty to the rate of change of atmospheric CO_2 between successive points in the record and that the atmospheric CO_2 shown by the Law Dome record has variations that the simple model cannot fit, such as the measurements between 1910 and 1945. Each estimate of the ocean inventory was assigned an error with standard deviation taken from its documentation. Though the two oceanic inventory estimates are based on similar sets of hydrographic measurements, we treated them as having independent error because they feature substantially different assumptions about the definition of anthropogenic carbon and the role of isopycnal diffusion in controlling anthropogenic CO_2 transport in the interior.

The error in the time series of ocean flux and Mauna Loa measurements is considered differently from the Law Dome and ocean inventory point estimates, because each features autocorrelated variability in the timeseries. This autocorrelation reflects climatic and process variations that the simple model does not resolve, but can confound parameter estimations. In estimation, this autocorrelation can be eliminated by taking decadal-averages (Bodman et al., 2013) or by introducing noise parameterizations to the estimation procedure (Ricciuto et al., 2008). We choose the latter as the sub-decadal variability should provide information about the posterior distribution of the model parameters so long as the autocorrelation is treated properly.

Noise parameters ρ and σ were added to the likelihood calculations for both the atmospheric CO_2 and ocean flux time series and subjected to inversion along with the other carbon cycle parameters (following the methods of Ricciuto et al. (2008)) . This assumption allows for the dominant noise process separating the model estimate at given time $M(\lambda, t)$ from the observational constraint at that time $y(t)$ to follow a

lag-1 autoregressive noise process,

$$y(t) = M(\lambda, t) + u(t) \tag{4.20}$$

$$u(t) = \rho \cdot u(t-1) + \sigma W(t) \tag{4.21}$$

where $W(t)$ is a standard normal random variable independently sampled for each year t. In the case that there is no autocorrelation in the time series, then the posterior value of ρ will be zero. The noise parameters for the Mauna Loa CO_2 time series are (ρ_a, σ_a) and for the ocean flux series noise parameters are (ρ_o, σ_o).

4.3.3 Model Forcing

For the parameter estimation, the carbon model is initialized in 1860 with atmospheric CO_2 concentration of 286 ppm. It is then integrated through 2012, forced by the historical emissions of CO_2 from fossil fuel burning from the RCP scenarios (Meinshausen et al., 2011b). Through 2010, the total fossil fuel emissions are 363 GtC (cf figure 4.1). Global temperature is constant before 1850 and then follows the NASA GISS annual global surface temperature anomaly prescribed without uncertainty (Hansen et al., 2010). At years when the atmospheric CO_2 concentration, ocean flux and ocean inventory are applied as a constraint, we take the modeled value and use it to calculate the likelihood given the observational constraints.

We chose to perform inversions under two representations of the historical fluxes of CO_2 from land use change. This is a coarse and initial investigation into the effect of the large uncertainty in the historical LUC emissions for model parameterization and climate policy. The cumulative LUC emissions differ by 60 GtC in 1960 and 75 GtC by 2010 in the two estimates, BOOK and ISAM (c.f. figure 4.1). The BOOK case uses the emissions estimates from the bookkeeping method, which is considered a benchmark product and is included in the budget analysis of the Global

Carbon Project (Houghton et al., 2012; Le Quéré et al., 2013). The ISAM case uses the estimates made with the Integrated Science Assessment Model (Jain et al., 2013).The ISAM model has been used to estimate emissions histories from multiple land use change histories. We take the estimate based on a regional downscaling of the history used to create the BOOK estimate. The choice of this LU history, from the set of ISAM estimates, is meant to emphasize the contribution of the assumed forest model to the uncertainty in total LUC emissions estimates.

4.4 Results

This section describes the results from our calculations in two parts. First, we describe the results of the MCMC sampling under the different assumptions of land use change. The first section contrasts the results for the parameters of the carbon model and the carbon system feedbacks. Second, we consider the posterior carbon model within the DICE framework and evaluate the effects of the carbon cycle feedbacks on the social cost of carbon and efficient policymaking.

4.4.1 Sampling Results

The MCMC sampling chain was run for 100000 iterations, starting from a high likelihood point in state space found with gradient line search. We use this point to initialize the sampling in a region of high likelihood to speed convergence. The total number of iterations was selected using the Raftery-Lewis test to achieve high precision estimates of the 5th and 95th quantiles of the model parameters (Raftery and Lewis, 1996). Visual inspection of the sampling chain and Geweke tests failed to detect significant drift in the distribution statistics, which is consistent with, but cannot prove, a convergent sampling (Geweke, 1991). Independent sampling chains initialized at different points showed similar results. We saved every hundredth iteration

of the chain, because the initial parts of the chain showed substantial autocorrelation between subsequent iterations. Thinning the chain can help to avoid autocorrelation and build the posterior distribution from independent samples. This conservative thinning factor left us with 1000 samples of the joint posterior probability distribution for the model parameters with no significant autocorrelation between samples. Existing for each LUC case, these 1000 samples form the basis of the following discussion of the parameter estimates, hindcasts and DICE projections. The statistics and correlation structures for each LUC case are shown in tables 4.2 and 4.3.

The median hindcasts for both LUC cases show reasonable fit to the imposed atmospheric data constraints (c.f. figure 4.2a) and a similar level of error. The median hindcasts for both LUC cases underestimate the Law Dome CO_2 measurements from 1900-1940, though are within the assumed error for those measurements. The level of autocorrelation in the residuals with the Mauna Loa time series is significant, with median estimates of ρ_a of 0.84 for ISAM and 0.99 for BOOK. The lower value of ρ_a from the ISAM case indicates a better fit to the Mauna Loa observations. The higher value in the BOOK case indicates that most samples in the MCMC chain have persistent errors compared to the Mauna Loa data. The standard error against the MLO data is comparable between the two cases (σ_a, ISAM: 0.5, BOOK: 0.5 ppm). The residual statistics for the ocean flux time history show moderate autocorrelation (ISAM: 0.15, BOOK: 0.14) and an absolute error estimate close to the stated uncertainty from the flux history product (0.5 GtC yr^{-1}). The ocean uptake in both cases is well within the imposed constraint (cf figure 4.2b). The ISAM estimates of total ocean uptake in 1995 are higher than those in the BOOK case (ISAM: 124 ± 5, BOOK: 115 ± 4).

Parameter Estimates

The posterior distributions of the parameters of the carbon model are significantly different between the two LUC cases (c.f. figure 4.3). The two sample Kolmogorov-Smirnov test (KS) confirms that the marginal distributions for m_{NPP}, q_{10}, k_{m1} and k_{m2} are significantly different ($p \ll 1e-3$) between the two LUC cases, though the mean estimates of the marginal distributions can be indistinguishable given the sample variance. The correlation structure of the carbon parameters are similar in the two cases.

The CO_2 fertilization factor m_{NPP} estimates are higher under ISAM than BOOK LUC emissions (c.f. figure 4.3). The mean values for the two cases (ISAM: 1.6 ± 0.05,BOOK: 1.29 ± 0.03) are separated by 2 standard deviations from either case. This result is consistent with the higher LUC emissions under ISAM, which require a stronger sink. It is natural to see this parameter compensate for the higher emissions, since the land carbon sink is constrained by mass balance.

The increased CO_2 fertilization factor under ISAM LUC emissions requires a larger q_{10} parameter for the land respiration sensitivity to temperature (cf figure 4.3), because the two parameters are positively correlated. The distance between the mean estimates (ISAM: 1.96 ± 0.41, BOOK:1.21 ± 0.15) is significantly larger than the standard deviation for either.

The difference in the LUC cases significantly impacts the slower export timescale k_{m2}. The marginal distributions are significantly different by the KS test ($p \ll 1e-3$) and the central estimates (ISAM: $0.019 \pm 2.7e-3$, BOOK: $0.014 \pm 2.3e-3$) are distinct.

Inversion Discussion

The largest difference in the posterior parameterizations of the carbon model is the strength of the CO_2 fertilization effect. This is an expected result of our choice in the two LUC histories, as the CO_2 fertilization effect necessary to balance emissions is

closely tied to the amount of historical emissions. The scale of the CO_2 fertilization effect is difficult to quantify independently. Evidence for its existence and potential for carbon storage in the face of nutrient limitation and drought is debated (Norby and Zak, 2011; Shevliakova et al., 2013). The deep uncertainty around the existence, scale and future of CO_2 fertilization provides significant uncertainty to future predictions of land CO_2 uptake, which we coarsely represent with the two parameterizations based on LUC history.

The two LUC cases give comparable probable estimates of present-day NPP (BOOK: 44±0.4, ISAM: 48±0.6 GtC yr^{-1}), which are less than the MODIS satellite based estimates of 53.5 GtC yr^{1-} (no error provided) (Zhao and Running, 2010), with meta-estimates of present-day NPP estimating a precision of ± 14 GtC yr^{-1}(Ito, 2011). In situ studies of four temperate forest areas demonstrated that at elevated ambient CO_2 (550 ppm), ecosystem NPP increased by a factor of 23±2 % and that there was a increase in net carbon storage (Norby et al., 2005). The estimated increase is higher than the observations in the ISAM estimate 42±3%, but similar in the BOOK case 19±2%.

The estimates of q_{10} we found are substantially different, conditioned on LUC emissions. In situ studies in terrestrial and wetland ecosystems have provided a meta-estimate of the q_10 parameter for soil respiration of 2.4 with a range of 1.3 to 3.3 (Raich and Schlesinger, 1992). The central estimate from the ISAM case is comparable to the meta-estimate, while the central estimate from the BOOK case is substantially lower.

The different land parameterizations between the LUC cases require different net change in the total land carbon stock, defined as the net land uptake (cf figure 4.2c). In the median ISAM hindcast, the land uptake switches from a source to a sink in the 1960s, a decade earlier than the median BOOK case. Data-based budgeting exercises estimate the net land uptake in 2005 to be -11 ± 47 GtC (Arora et al., 2011). In

2005, the net land uptake is higher in the ISAM case (-29 ± 6 GtC) than the BOOK case (-36 ± 6), putting both LUC cases in the lower half of net land uptake estimates. The similarity in the 2005 estimates of net land use change is gone at the end of the historical simulations in 2012 (ISAM: -12±7, BOOK:-29±7 GtC).

The posterior carbon model can be compared to the CMIP5 models and the prior distribution using the linear feedback metrics (cf table 4.1). The ISAM case has strong land carbon-concentration and carbon-climate feedbacks relative to the prior. While the BOOK case has weaker land carbon feedbacks to both increasing CO_2 and temperature. It is notable that the β_l feedback parameter in the BOOK case (0.5±0.06 GtC ppm^{-1}) is higher than the feedback in models with nitrogen-limited photosynthesis in the CMIP5 ensemble (NorESM-ME: 0.22, CESM-BGC: 0.24 GtC ppm^{-1}) (Tjiputra et al., 2012; Lindsay et al., 2013). The ISAM case, however, exhibits a central estimate of β_l that falls amongst the CMIP5 models with moderate CO_2 fertilization (Arora et al., 2013).

The land carbon-climate feedback metrics for the two LUC cases also divide the feedbacks exhibited by the CMIP5 models. In the BOOK case, the weak temperature feedback is similar to the smallest feedbacks in the CMIP5 models. These again happen to be in the nitrogen cycling models from CMIP5, because soil temperature increases make more nitrogen available for photosynthesis in those models (NorESM-ME: -16, CESM-BGC: -21 GtC $°C^{-1}$) (Arora et al., 2013). The carbon balance in the BOOK estimates is consistent with such a balance. In contrast to the BOOK case, the ISAM carbon-climate feedback on land is amongst the largest in the group of CMIP5 models, reflecting the balance with high CO_2 fertilization.

Under inversion, the carbon-concentration metric for the ocean increases from the CMIP5 prior (CMIP5: 0.8±0.07, BOOK: 0.9±0.1, ISAM: 1.0 ± 0.1 GtC ppm^{-1}). This upward revision reflects the generally low oceanic uptake of CO_2 in the CMIP5 ESMs compared to the observational constraints (Friedlingstein et al., 2013).

We are left with two parameter sets for the simple carbon model, individually conditioned on LUC history. The BOOK case is qualitatively similar to the CMIP5 earth system models with nitrogen cycling in the land biosphere. It is less sensitive to increasing CO_2 and temperatures, with the scale of the CO_2 fertilization effect similar to that observed in temperature forest ecosystems. The ISAM case is analogous to CMIP5 earth system models with high sensitivity to increasing CO_2 concentrations and atmospheric temperatures, has q_{10} estimates consistent with observations and fits the Mauna Loa CO_2 record better than the BOOK case. To make predictions under the total uncertainty implied by our two LUC histories, we assume the LUC histories are equally likely and combine the associated to parameter sets to create a combined posterior parameter distribution. Going forward, we present forecasts of the global CO_2 budget from the combined and conditional parameterizations, with the conditional cases referred to as the BOOK and ISAM LUC cases.

4.4.2 Integrated Assessment

In this section, we describe the impact of the uncertainty in the carbon cycle feedbacks on projections of the global CO_2 balance and policy outcomes. We consider cases with both business as usual and efficiently controlled CO_2 emissions. In the business as usual (BAU) case, mitigation effort proceeds under current policies and is eventually applied to compensate for diminishing fossil fuel resources (capped at 6000 GtC) (Nordhaus, 2014). In the efficient case, mitigation effort is undertaken after 2015 to maximize expected welfare, over the combined posterior parameter set from the LUC cases, in a cost-benefit optimization. The efficient case makes use to the marginal abatement curves (cost of reducing emissions) from DICE2013. We initialize the model in 2010 with the mean carbon stocks from the combined BOOK and ISAM cases and with atmospheric temperature 0.8 °C over preindustrial.

The different policy cases exhibit significantly different levels of cumulative CO_2 emissions. Under BAU, post-2010 cumulative emissions exceed 540 GtC by 2050, 1700 GtC by 2100 and eventually total over 4000 GtC. The post-2010 efficient emissions are much lower. For the quadratic damage function, they are 410 GtC by 2050 and 950 GtC by 2100 and total under 1100 GtC. Under these two emissions scenarios, the predicted climate shows substantially different climatic outcomes in predicted atmospheric CO_2, temperature and economic damages and significant uncertainty arising from the carbon cycle.

Under all the BAU and efficient policies, future atmospheric CO_2 grows with time (cf figure 4.4). By 2100 in the combined parameterization, the median atmospheric CO_2 in the BAU policy is 870 ppm (800-920) (5-95th percentile ranges in this section and associated figures) and in the quadratic efficient policy case it is 580 ppm (540-620). The difference between those estimates indicates the critical role of the chosen policy in controlling atmospheric CO_2 beyond 2050, even with uncertainty in the carbon cycle feedbacks.

In both the BAU and efficient policies, the projections for the ISAM parameters show less atmospheric CO_2 accumulation than the BOOK projections (cf figure 4.4a,c). Taken individually, the parameter conditioned on the ISAM LUC case occupy the lower half of the total uncertainty range in predicted CO_2, while the parameters for the BOOK LUC case occupy the upper half of the total uncertainty range. Under the BAU policy, the median atmospheric CO_2 concentration in 2100 is 70 ppm higher in the BOOK case than the ISAM case. In the efficient policy, the median atmospheric CO_2 in 2100 is 40 ppm higher in the BOOK case.

In both policies, the median difference between atmospheric CO_2 in the two LUC cases is almost entirely represented by differences in net land uptake (cf table 4.4). Oceanic uptake does not demonstrate large differences between the two LUC cases, differing by less than 5% in 2100. Though there is substantial uncertainty in the

probable range of oceanic uptake, up to 80 GtC by 2100, the uncertainty in future oceanic uptake is only about half that of the future net land uptake.

Uncertainty in the the future concentrations of CO_2 drives uncertainty in future temperature. The model predicts temperature increase of 3.8 °C (3.6-4.0) over preindustrial for the BAU policy and 3.0 °C (2.8-3.1) in the efficient policy. Again, the two LUC cases define the range in predicted temperatures, with the higher CO_2 concentrations in the ISAM case leading to higher temperatures.

Under the cubic damage function, the efficient policy emissions are 340 GtC by 2050, 530 GtC by 2100 and total almost 700 GtC. At this lower level of emissions, the year 2100 atmospheric CO_2 in the combined parameterization is 460 ppm (440-470) and temperature increase at 2100 is limited to 2.4 °C (2.3-2.6). The relationship between the two LUC cases holds under the cubic damage policy. The total uncertainty in the predicted temperature and the difference conditioned on LUC motivate an investigation into the damages predicted for each outcome in the DICE framework and the implications for carbon pricing.

Social Cost of Carbon

The social cost of carbon (SCC) is defined as the change in expected welfare that results from a unit of additional emissions in a given year, normalized to the change in welfare that results from a unit change in consumption in the same year (Newbold et al., 2010). Unitized as dollars per ton of CO_2, it is a measure of the marginal damages that could be expected from emitting an additional ton of CO_2 against a background emissions pathway.

$$SCC(t) = -\frac{dEW}{dE(t)} / \frac{dEW}{dC(t)} \tag{4.22}$$

Here we discuss the expected change in welfare across the carbon system parameters from the inversion. We report values for the combined posterior distribution as well as the distributions conditional on either LUC history (cf figure 4.5a). To reflect uncertainty in the SCC estimate, we also show the SCC calculated for each individual set of parameters within the posterior samplings, known as the deterministic SCC. The range in deterministic SCC is shown as an error bar in figure 4.5.

The SCC calculated for the quadratic damage function and against the BAU emissions pathway provides a baseline case for examining the SCC under carbon cycle feedbacks. The baseline SCC for our model with joint parameters is \$18 per ton of CO_2 in 2015 and grows to \$55 per ton in 2050, an average growth rate of 3.2% per year (cf figure 4.5a). With cubic damages, the SCC values for the BAU policy are much larger, starting at \$65 per ton in 2015 and growing to \$263 in 2050, a growth rate of 4.1% per year.

The role of temperature and ocean carbonate feedbacks on the carbon cycle is particularly evident in the difference in SCC between our model and the DICE2013 carbon cycle between the two policy cases. In the BAU case, with significantly more warming in the late 21st and 22nd century, the SCC in our model grows faster than for the DICE carbon model. By 2050, the value is 20% higher for quadratic damages and 40% higher for cubic damages. The higher initial value and growth rate in our model is attributable to the increased CO_2 and rapid warming in the BAU case, which activates the positive climate-carbon feedbacks in our model. This difference is not evident in the efficient case, where the SCC estimates for our model are close to those from DICE through 2050.

The SCC estimates consistently represent the differences between the carbon cycle parameters conditional on the LUC cases. The SCC for the BOOK LUC case is consistently larger than that of the ISAM case. In the BAU case, the difference between the two decreases in time. For quadratic damages, the difference decreases

from 10% in 2015 to 3% in 2050. The corresponding decrease for cubic damages is 13% to 5%. The decreasing difference is a result of the stronger increase in land respiration in the ISAM case. The same trend is not present in the efficient policy cases, where the BOOK SCC is consistently 16% higher for quadratic damages and 30% higher for cubic damages, because the temperature change is not sufficient to overpower the difference in land sink between the LUC cases.

The differences between the growth of the SCC in the two LUC cases, and from the DICE carbon cycle model, show that the importance of the carbon-climate feedbacks and dependence on temperature compensate for the difference in the land carbon sink efficiency in the BAU case. The difference between the estimates conditioned on LUC decreases with time, and increasing temperature, such that total uncertainty in the SCC proportionally decreases. Under controlled emissions and less warming in the efficient case, the strength of the land carbon sink controls the value of the SCC through 2100.

Learning and Policy Transitions

In this section, we calculate the expected consumption benefit that would result from reducing uncertainty about the future carbon cycle response to emissions. Since the two parameterizations of the carbon model conditioned on LUC yield substantially different outcomes under the efficient policy, which maximized welfare over their combined parameter distribution, they provide a test case to consider the possible benefits to policy outcomes from reducing uncertainty in future predictions of the carbon system. The potential benefit is easy to understand from the SCC results, where the SCC is high under BOOK LUC, low for ISAM LUC and intermediate for the combined distribution. If the parameters conditioned on BOOK represent the true state of the world, then the optimal mitigation effort will be larger than for the combined case. In the reverse, if the ISAM parameters are true, then the optimal

mitigation will be less intense than the combined case. This policy divergence is confirmed when we calculate policies that maximize expected welfare for the carbon system parameters conditioned on either LUC case (c.f. figure 4.6). We find that the model conditioned on BOOK LUC calls for an increase in the initial carbon tax of \$1.2 per ton CO_2, growing to \$3.4 by 2050 and \$7.9 by 2100, which corresponds to the mitigation of an additional 3-5% of emissions over the effort in the efficient case.

To evaluate the effect of learning, we calculated pathways to optimize the total expected welfare when the decision maker is constrained to make decisions under the joint distribution until time t_l, when the truer of the two LUC cases can be distinguished and set policy thereafter to maximize expected welfare under the true case. Thus we pose the learning problem as a binary one, where at some point in time in the next five decades the decision maker is able to distinguish between the LUC cases and thereafter make policy conditional on the posterior parameters associated with either LUC case.

We calculated the expected consumption benefit from the change in the expected welfare before and after learning using value of information calculations. The value of information VOI is the amount of consumption that could be sacrificed, from the expected outcome of the post-learning policy, before the expected utility after learning is equal to the expected welfare at the present state of knowledge. For possible carbon parameter sets λ_i, let the combined posterior distribution for the two LUC cases $\mathrm{p}(\lambda_i)$ be the current state of knowledge, with the probability distributions over the two LUC cases and the respective optimal policies represented by subscripts, $\mathrm{p}_j(\lambda_i)$ and m_j. When the decision maker expects to distinguish between the LUC cases at time t_l, then the VOI can be defined implicitly by the following:

$$\max_m \sum_i p(\lambda_i) W[c_t(m|\lambda_i)] = \max_{m_b, t=0\ldots t_l} \sum_{p_j(\lambda_i)} \max_{m_j, t=t_l+1,\ldots} \sum_i p_j(\lambda_i) W(c_t(m_j|\lambda_i) - VOI). \tag{4.23}$$

The expected welfare on the left hand side is for the combined distribution and assumes the decision maker never learns which LUC case, or set of parameters, better reflects the true state of the world. The expected welfare on the right hand side assumes the decision maker can change policy immediately after distinguishing between the two LUC parameterizations, where they are equally likely *a priori*. If the value of VOI were zero, then the right hand side would be greater than or equal to the left hand side, but VOI is defined as the reduction in consumption necessary to make the two sides equal. Calculating the value of information in this way means that a rational decision maker would be willing to forgo consumption in an amount up to the VOI to be able to distinguish between the land use cases at time t_l. We calculate the VOI as a fixed percentage of consumption sacrificed from all time intervals, following the methodology of (Newbold and Marten, 2014). We also express VOI as that same percentage of the sum of future consumption, discounted to net present value (NPV). Both expressions of VOI are shown in table 4.5

The benefits to learning about the carbon system parameters for policy outcomes are substantial, but small compared to the overall benefits of adopting the efficient policy over BAU. The expected VOI for distinguishing immediately between the two LUC cases is $31 billion NPV. The expected benefit decreases by about $3 billion NPV for every decade that the learning is delayed (cf table 4.5, column 1). As a comparison, the expected value of adopting the efficient policy instead of the BAU policy is $25 trillion NPV. Thus improvements in knowledge of the carbon system would only be expected to increase the efficiency of mitigation policy by 0.1 percent.

We repeated the VOI calculation for the cubic damage function to test the dependence of the VOI on the assumed damage function. The VOI increases in that case significantly, with an benefit of instantaneous learning of $163 billion (cf table 4.5, column 2). Under cubic damages, the VOI decreases by about $10 billion NPV per decade. The VOI also increases as a proportion of the total benefit of policy, where

the efficient policy for cubic damages is valued at about 11 $ trillion NPV. Though the benefits of learning about the carbon system are still only about 1.5% of the total value of the climate policy.

As a last test, we again repeated the VOI calculations for a different set of social parameters. We calculated optimal pathways with the DICE2013 quadratic damage function, but with a lower pure rate of time preference, $\rho' = 0.001$ and same marginal elasticity of consumption $\eta = 1.4$. Decreasing ρ' from 0.015 to 0.001 decreases the average discount rate and increases the weight of damages beyond 2100 in the expected welfare calculation. This lower pure rate of time preference represents a plausible set of parameters within climate economics literature (Stern et al., 2006). As expected, this increases the VOI associated with resolving the uncertainty in the carbon system, where immediate learning is valued at 396 $ billion NPV with decadal decreases of approximately 30 $ billion. The VOI as a proportion of the total value of the policy, however, is approximately 0.1 percent as in the case for the standard DICE2013 social and damages parameters.

4.4.3 Policy Implications

The results of our SCC and optimal mitigation calculations indicate that uncertainty in the evolution of the carbon system, as represented in the data-constrained simple model, has a modest effect on the outcomes of an integrated assessment model. This is especially true when damages are quadratic with temperature increases. In the quadratic case, the uncertainty in carbon cycle feedbacks imposes a small uncertainty on the 2015 baseline SCC of 19 $ per ton CO_2, with a 90-percent probability range of $17 to 21 . Other studies have shown that uncertainty in the equilibrium climate sensitivity drives much larger ranges in estimated SCC, though for different model parameterizations and social parameters than we used here. It is not unreasonable to expect that physical uncertainty, as represented by uncertainty in the equilibrium

climate sensitivity (Roe and Baker, 2007), will result in a range of SCC values an order of magnitude larger (i.e. 5-50 $ per ton CO_2 in 2015) than the range we estimate from our carbon model (Interagency Working Group on the Social Cost of Carbon, 2010). Even larger uncertainties in the SCC come from varying the specifications of damage and social parameters (Kopp et al., 2012).

The relatively small impact of the carbon cycle uncertainty on the SCC directly impacts how much benefit can be expected by learning about the range of potential feedbacks. Compared to the total value of imposing a policy, we find modest gains in expected welfare for reductions in uncertainty. However, we simulate a fairly coarse measure of learning by conditioning on LUC emissions. Conditioned on either LUC case, the uncertainty in the predictions of future CO_2 decreases by about half, when uncertainty is measured by the 5-95th percentile range in predicted CO_2 concentrations. VOI studies for equilibrium climate sensitivity have shown significant increases in VOI with increasing reductions in uncertainty (Newbold and Marten, 2014) and the same may hold for carbon cycle uncertainty.

One policy consideration that could strongly impact VOI calculations for the carbon system would be the imposition of a temperature threshold policy instead of a cost-benefit optimization, such as the 2°C warming target expressed by the 2009 UN Copenhagen Accord. Though the 2°C target will likely require negative emissions in the future (Arora et al., 2011). The presence of a temperature threshold dramatically increases the value of information and policy implications of learning when applied to the equilibrium climate sensitivity (Webster et al., 2008). However, the numerical challenges to calculating policy for climate thresholds are nontrivial (Keller et al., 2004) and we defer to later study, but a brief example can demonstrate how the presence of a threshold may impact the value of learning about the carbon system.

We can approximate the difference in mitigation costs of a temperature threshold policy by scaling the optimal mitigation pathways for each LUC case, such that the

probability of exceeding a temperature threshold of 2.5°C was 10 percent. The mitigation effort necessary to achieve that temperature threshold is significantly different between the LUC cases, as shown in figure 4.7 by the cumulative emissions and future mitigation burden for each LUC case. The future mitigation burden is the cumulative sum of future mitigation costs NPV. Since the temperature change is upper-bounded, the mitigation effort necessary to meet the threshold is determined by the upper range of predicted atmospheric CO_2 for each LUC case. Thus the bounded policy for carbon parameters conditioned on the BOOK LUC case is similar to the combined parameterization. The difference in mitigation burden between the LUC cases is substantial, amounting to almost $7 trillion NPV. Here a decision maker learning between the two LUC cases could reap substantial benefit from learning that the ISAM model was the truer state of world, in terms of a reduced mitigation burden through 2080.

4.5 Conclusions

In this study, we examined how uncertainty in projections of the carbon cycle affects carbon prices and climate policy outcomes. As previous studies had looked at this question with longitudinal studies across different integrated assessment models, we chose to use a single model of the carbon cycle. The parameters of the model were varied in Monte Carlo simulations to simulate uncertainty. Data constraints on the uncertain parameters were imposed using Bayesian techniques. The results of the study have scientific and policy implications.

We found a significant dependence of the parameters of the data-constrained model on the assumed history of land use change emissions. The uncertainty in historical land use change emissions is significant (quoted as being up to 50% of the cumulative total estimates). That uncertainty impacted our estimates of the strength of CO_2 fertilization of NPP on land, because land NPP controls the net land uptake

and it only constrained by mass balance in our study. Other studies relying on mass balance to obtain formal estimates of CO_2 fertilization factors will be sensitive to this effect. The improved quality of fit to the Mauna Loa time series, for this model, in the higher emissions case (ISAM) prompts future study into the use of such a model combined with data constraints to constrain historical LUC emissions.

The two LUC cases provided a framework for us to examine the implications of a substantial uncertainty in the carbon cycle model on the outcomes of a DICE-like integrated assessment model. We found that the estimates of the social cost of carbon do not display the same significant difference that we observed in the physical outcomes from the model. We are also able to attribute an additional growth, \$10 per ton of CO_2 by 2050, in the baseline SCC to temperature feedbacks within the carbon system. These feedbacks are not present in the standard DICE IAM.

Resolving the difference in the LUC cases, which amounts to learning about the strength of CO_2 fertilization and substantially reducing the uncertainty in predicted CO_2 concentrations for an emissions pathway, has a small effect on the efficiency of the optimal climate policies set by DICE. However, the expected value of information that would allow one to distinguish between the two cases measures in the \$10-100 billions NPV under varying damage and discounting assumptions. The value of information would likely be higher for policies which set an express temperature warming threshold, which we leave as an interesting avenue for future research into the policy implications of carbon cycle science.

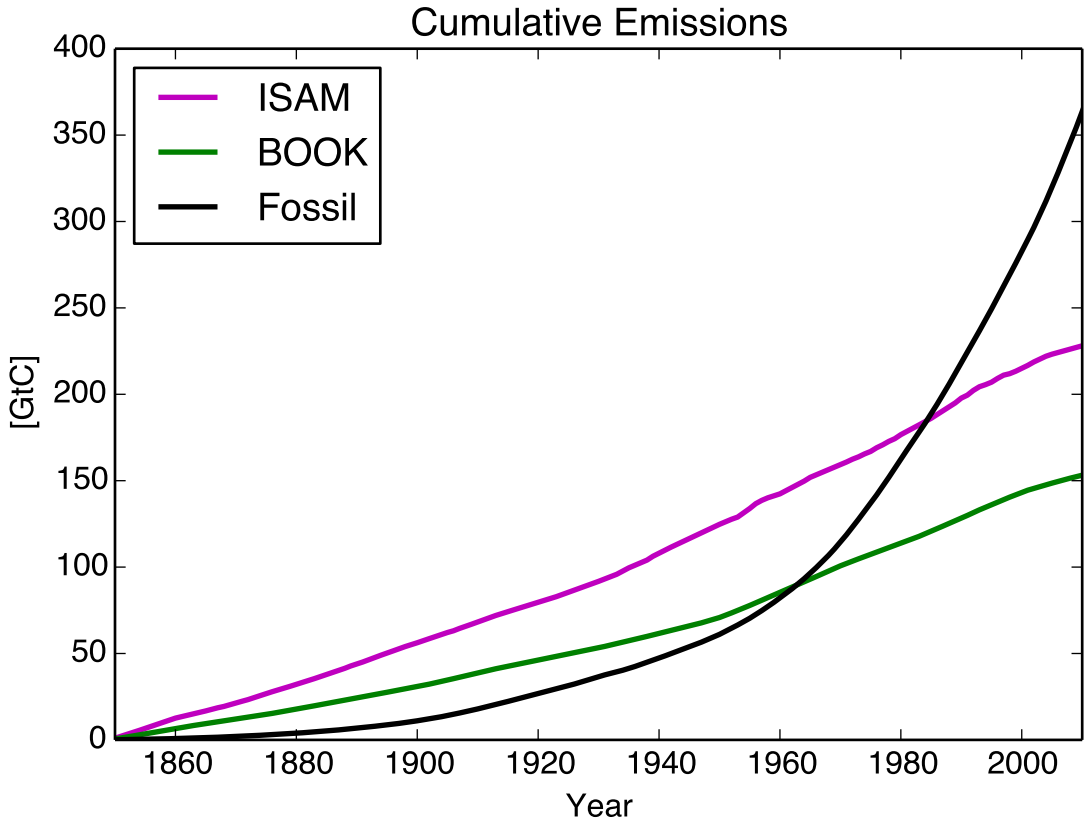

Figure 4.1: The cumulative annual emissions of CO_2 [GtC] from 1850 to present day. The cumulative emissions plots show the substantial difference in the estimates of LUC emissions rates before 1960.

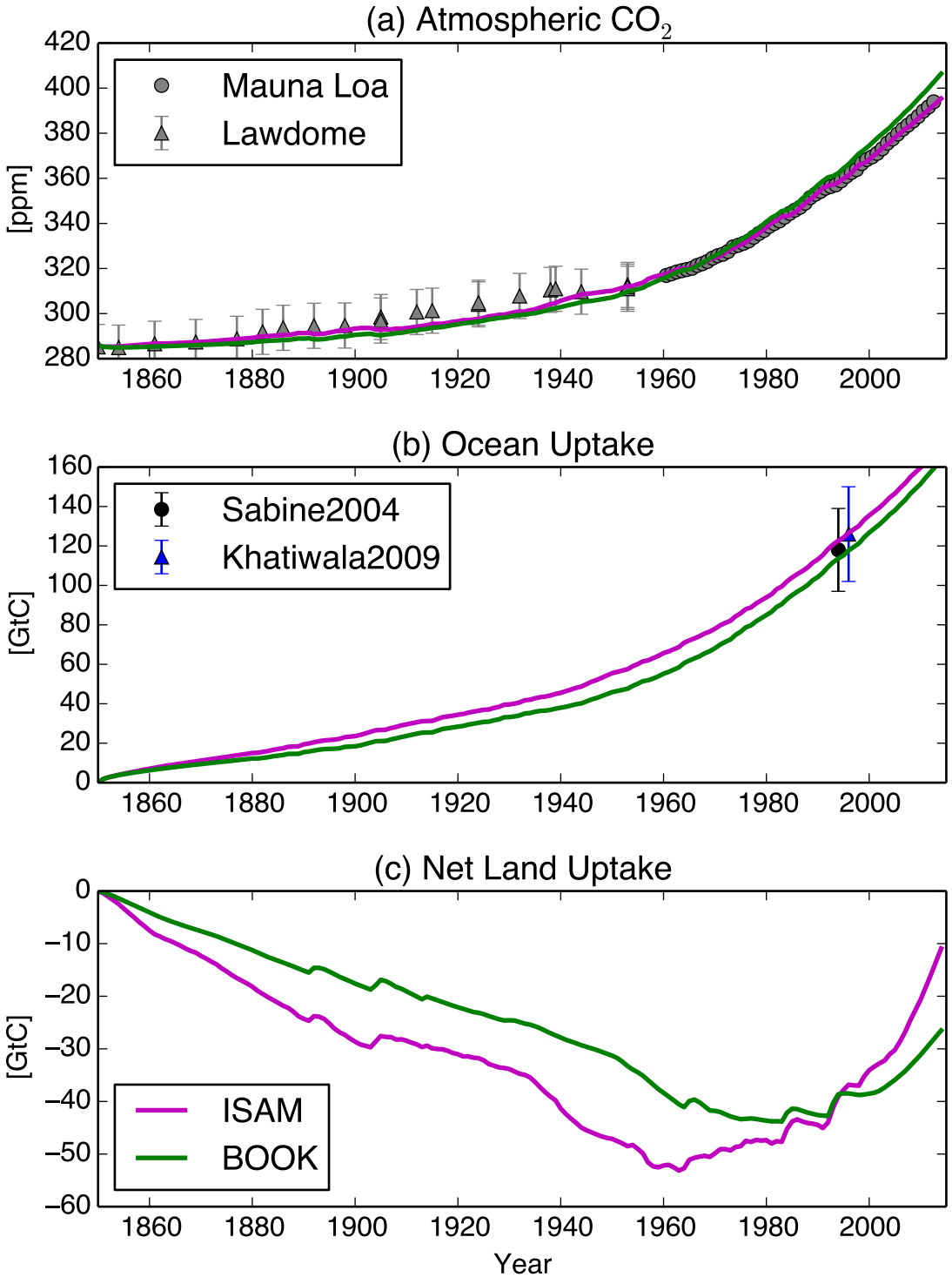

Figure 4.2: Hindcasts of the CO_2 budget shown as atmospheric CO_2 concentration [ppm], total oceanic uptake [GtC] and net land uptake [GtC] for historical simulations under the BOOK and ISAM LUC cases.

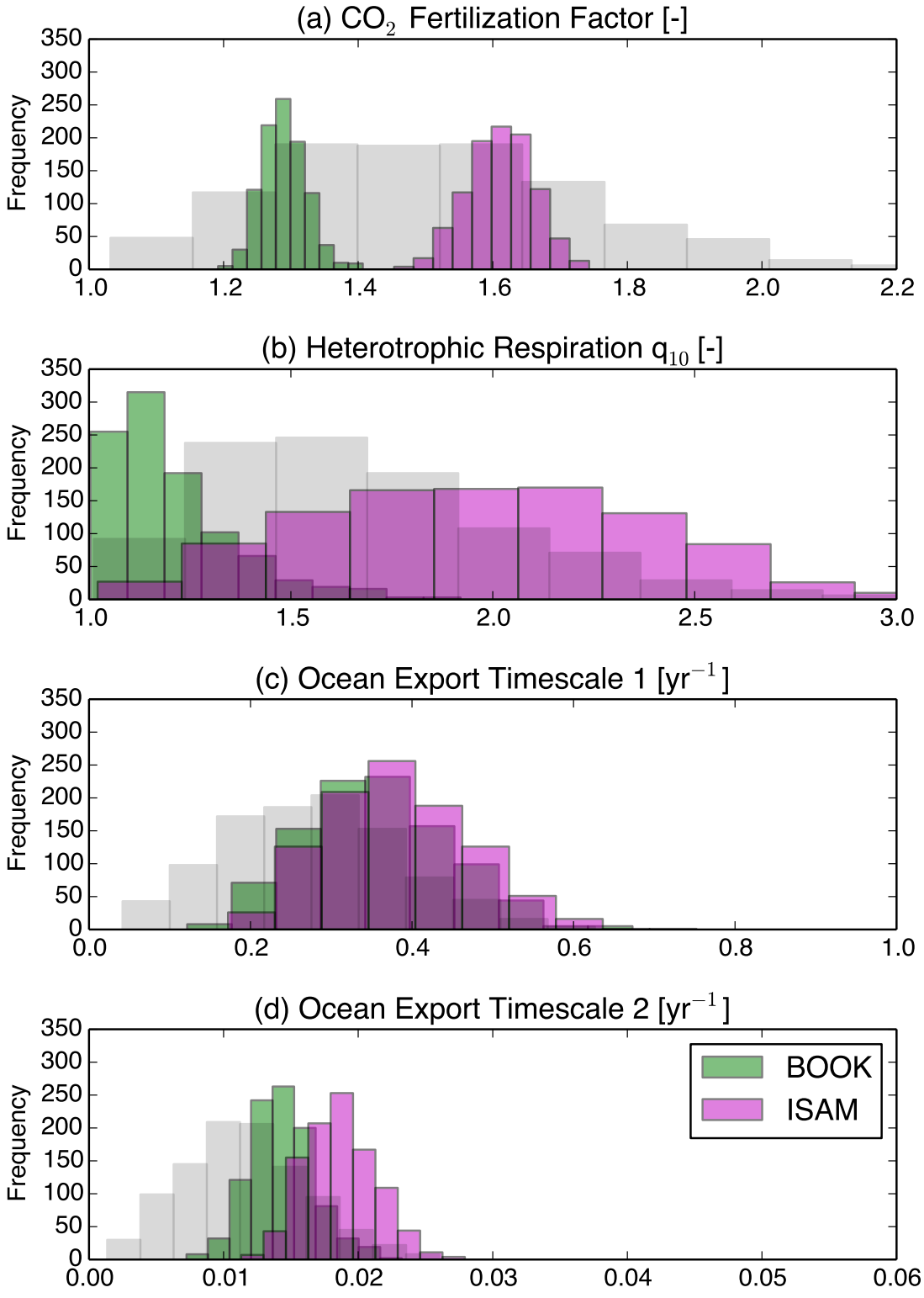

Figure 4.3: Histograms of 1000 samples from the MCMC chains for the carbon cycle parameters (a) m_{NPP} [-], (b) q_{10} [-], (c) k_{m1} [yr^{-1}] and (d) k_{m2} [yr^{-1}]. Prior distributions are shown in grey.

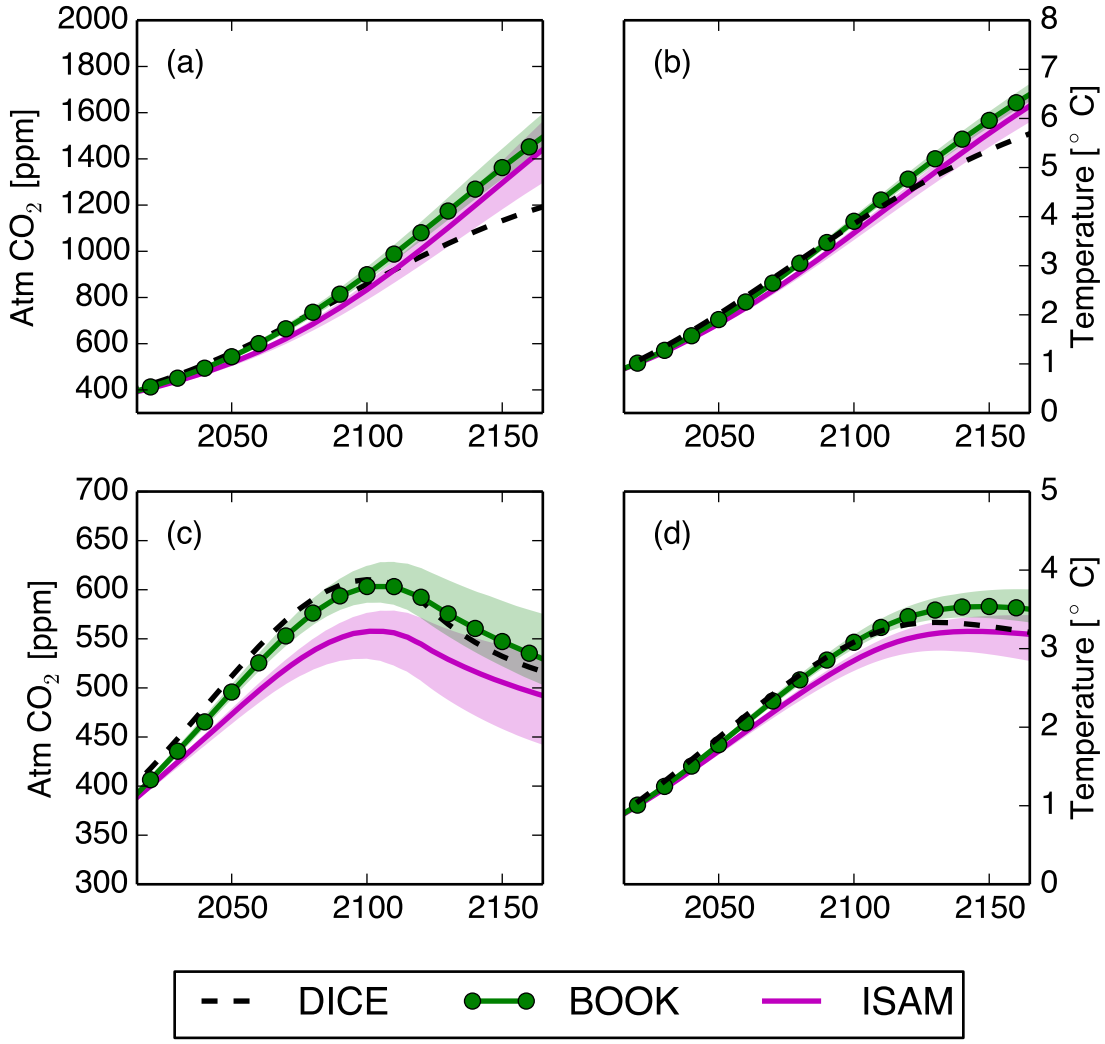

Figure 4.4: Projections of atmospheric CO_2 [ppm] and temperature warming [°C] for business as usual (BAU) and efficient policies: (a) Atmospheric CO_2 under BAU, (b) Temperature change under BAU, (c) Atmospheric CO_2 under efficient policy, and (d) Temperature change under efficient policy. The credible confidence range (5-95th percentile) is shown separately for the BOOK and ISAM LUC posterior parameters. The thin dashed line shows results for the DICE2013 prediction of atmospheric CO_2.

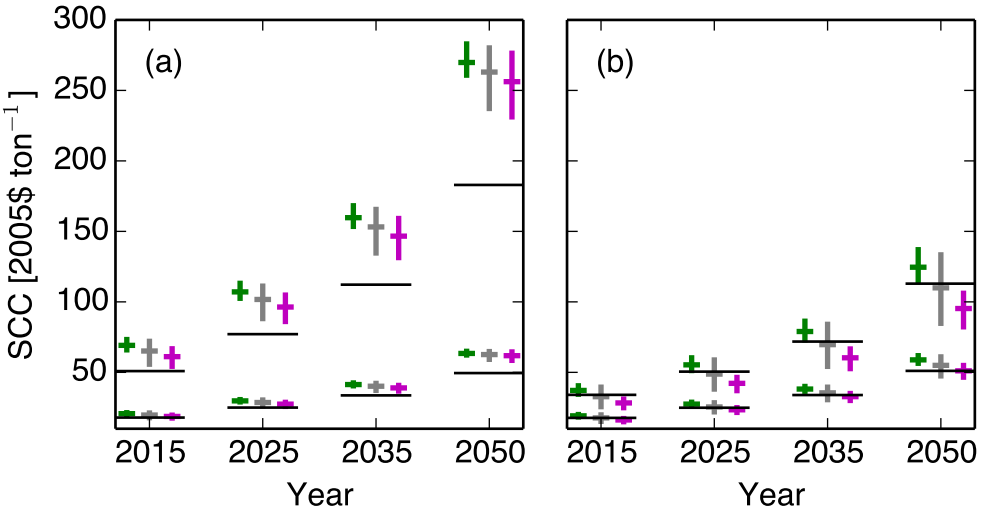

Figure 4.5: The social cost of carbon [SCC, \$ ton^{-1}] under different damage functions (upper values: cubic, lower values: quadratic) and different policy scenarios: (a) business as usual and (b) efficient policies. Crosses show the SCC calculated with uncertainty in the carbon system; the horizontal hatch mark shows the SCC and the vertical line shows the range in SCC estimates for each case. Values are shown for the combined (grey, center), BOOK (green, left) and ISAM (magenta, right) LUC cases. The long horizontal lines are the coincident SCC values calculated with the DICE2013 carbon cycle.

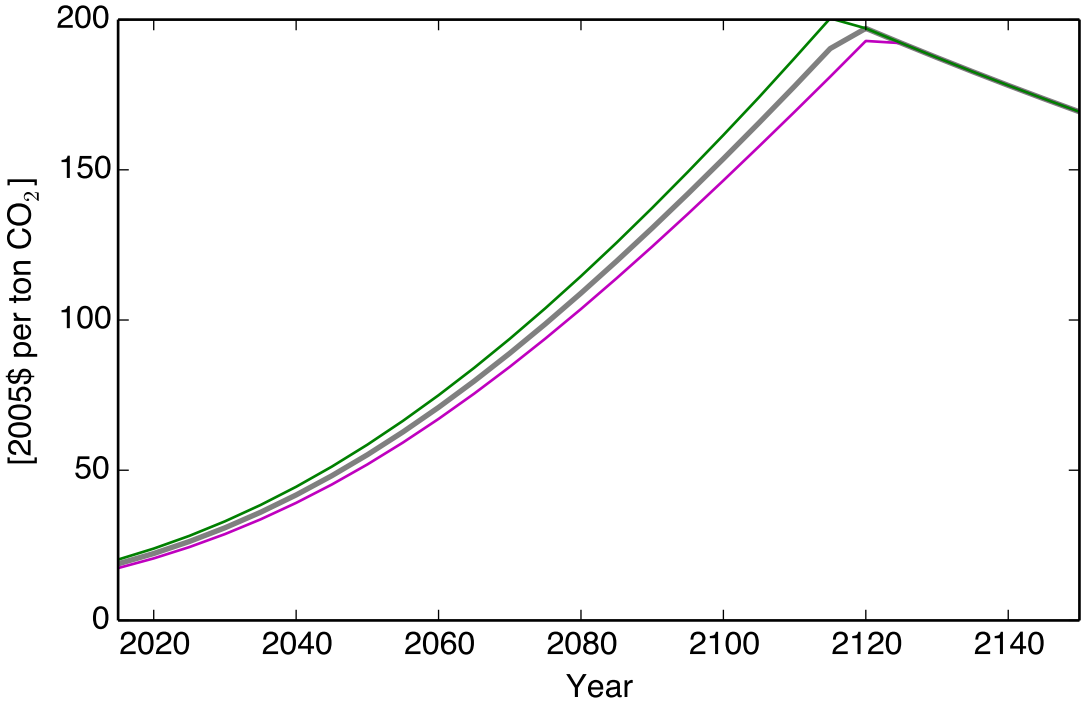

Figure 4.6: The optimal carbon tax [\$ ton^{-1}] under different parameterizations of the carbon system (combined, grey; BOOK, green; ISAM, magenta).

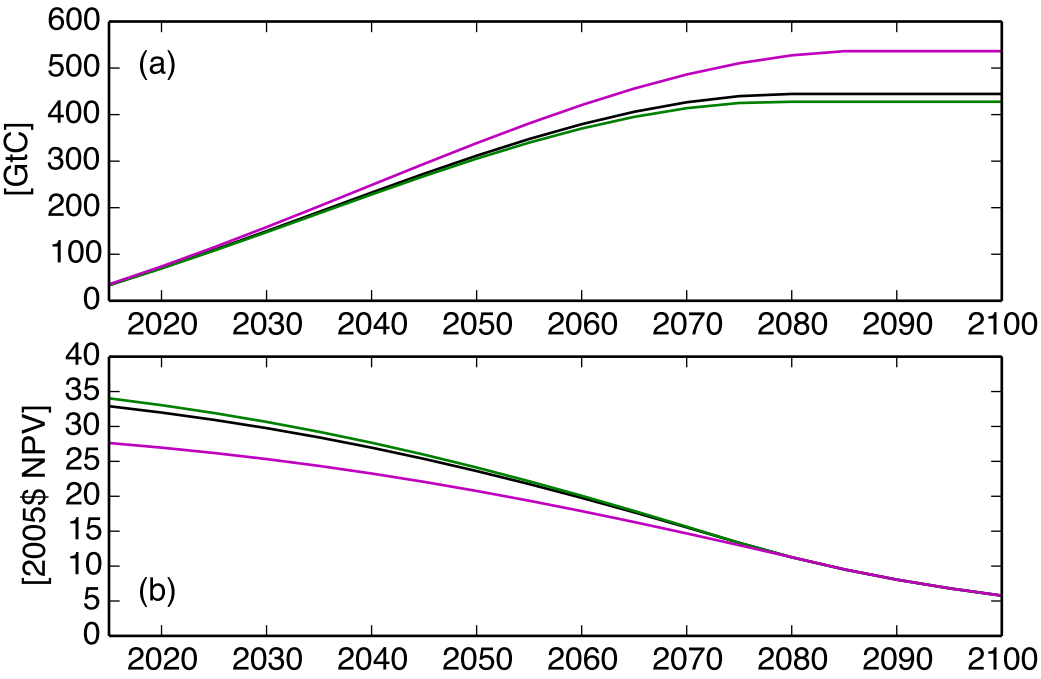

Figure 4.7: The mitigation effort necessary to limit warming to a threshold of 2.5° C under the different LUC cases in our model (combined, grey; BOOK, green; ISAM, magenta), shown as (a) cumulative emissions post-2010 [GtC] and (b) total mitigation burden [2005$ NPV].

Table 4.1: Linear feedback parameters the simple carbon model and earth system models

	Carbon-Concentration feedback GtC ppm^{-1}		Carbon-Climate feedback GtC $°C^{-1}$	
Parameters	Land: β_l	Ocean: β_o	Land: γ_l	Ocean: γ_o
C^4MIP[1]	1.35 (0.61)	1.13 (0.26)	-78.6 (45.8)	-30.9 (16.3)
CMIP5[2]	0.92 (0.44)	0.80 (0.07)	-58.4 (28.5)	-7.8 (2.9)
Prior	0.9 (0.4)	0.8 (0.1)	-60 (28)	-28 (6)
ISAM	1.1 (0.1)	0.99 (0.04)	-82 (28)	–
BOOK	0.5 (0.06)	0.88 (0.04)	-22 (15)	–

[1] See Friedlingstein et al. (2006)

[2] See Arora et al. (2013) for description of calculations. We present FEA-type calculations here.

Table 4.2: Carbon cycle model parameter estimates

	ISAM		BOOK	
	mean (std)	5-95 percentiles	mean (std)	5-95 percentiles
Model Parameters				
m_{NPP}	1.61 (0.05)	(1.53,1.68)	1.29 (0.03)	(1.24,1.34)
q_{10}	1.96 (0.41)	(1.29,2.62)	1.21 (0.15)	(1.0,1.53)
k_{m1}	0.38 (0.08)	(0.24,0.53)	0.36 (0.09)	(0.21,0.51)
k_{m2}	0.019 (2.7e-3)	(0.014,0.023)	0.014 (2.3e-3)	(0.011,0.018)
Noise Parameters				
ρ_a	0.84 (0.15)	(0.58,0.99)	0.99 (0.01)	(0.97,0.99)
σ_a	0.51 (0.05)	(0.42,0.60)	0.50 (0.05)	(0.42,0.59)
ρ_o	0.15 (0.11)	(7.9e-3,0.38)	0.14 (0.12)	(0.01,0.36)
σ_o	0.47 (0.07)	(0.37, 0.57)	0.45 (0.06)	(0.36,0.56)

Table 4.3: Carbon cycle model parameter correlation

	ISAM				BOOK			
	m_{NPP}	q_{10}	k_{m1}	k_{m2}	m_{NPP}	q_{10}	k_{m1}	k_{m2}
m_{NPP}	1				1			
q_{10}	0.86	1			0.61	1		
k_{m1}	-0.08	-0.01	1		-0.1	-0.04	1	
k_{m2}	-0.45	-0.2	-0.44	1	-0.37	-0.1	-0.5	1

Table 4.4: Excess atmospheric CO_2 and net land uptake under BAU and efficient policies in 2025, 2050 and 2100. Median values are shown as the estimate with the 5-95% confidence range.

Year	BAU		Efficient	
2025				
Atmosphere (GtC)	306 (300-310)	326 (321-332)	285 (280-289)	304 (299-309)
Land (GtC)	40 (36-47)	19 (13-25)	38 (33-45)	17 (12-23)
Ocean (GtC)	191 (187-196)	193 (187-197)	187 (182-191)	188 (183-192)
2050				
Atmosphere (GtC)	508 (490-516)	564 (552-577)	415 (398-424)	463 (452-475)
Land (GtC)	126 (110-148)	66 (47-83)	108 (94-129)	56 (39-73)
Ocean (GtC)	298 (286-309)	301 (289-312)	273 (262-283)	276 (265-286)
2100				
Atmosphere (GtC)	1179 (1099-1231)	1317 (1276-1371)	594 (538-631)	691 (659-733)
Land (GtC)	357 (292-449)	227 (164-282)	289 (238-361)	191 (138-236)
Ocean (GtC)	582 (546-617)	572 (540-608)	439 (408-467)	440 (412-468)

Table 4.5: Expected consumption benefit of distinguishing LUC case, shown as net present value [NPV, 2005$ billion] and as a fixed percentage of consumption from 2010-2310 [%]

Learning time	Default Damages		Cubic Damages		Low Discount	
t_l	NPV	%	NVP	%	NVP	%
2015	31	1.2e-3	163	6.1e-3	396	5.4e-3
2025	29	1.1e-3	153	5.7e-3	369	5.0e-3
2035	26	1.0e-3	140	5.2e-3	331	4.5e-3
2050	7	8.5e-4	113	4.2e-3	245	3.3e-3

Table 4.6: Key of carbon model parameters, based on SCCM Raupach (2013); Harman et al. (2011)

	Value	Notes
Land Parameters		
NPP_0	40.	[GtC yr^{-1}]: Preindustrial Net Primary Production (NPP)
m_{NPP} †	1.5	*No units*: CO_2 fertilization factor of NPP at saturation.
p	2.5	*No units*: Rate of saturation parameter for CO_2 fertilization of NPP
C_{NPP}	687	GtC; Slope parameter for CO_2 fertilization of NPP
α_{L1}, α_{L2}	(0.5,0.5)	*No units*: Partitioning of NPP into land carbon stocks (C_{L1}, C_{L2})
VAI		*No units*: Volcanic Aerosol Index time series 1890-2000 Ammann et al. (2003)
q_{10} †	2	*No units*: q_{10} factor for increased land respiration with warming
k_{L1}, k_{L2}	(1/2.5,1/250)	yr^{-1}: Land carbon stock respiration timescales
Ocean Parameters		
α_m^i	(0.512934, 0.320278, 0.142183, 0.024605)	*No units*: Partitioning of sea-air CO_2 flux into mixed layer stocks C_{mi} Raupach et al. (2011)
k_{m_i} †	(5.22893, 0.356532, 0.0194692, 0.0)	yr^{-1} : Mixed layer carbon stock export timescales
ν	1/312	$molkg^{-1}GtC^{-1}$: Conversion factor for carbon stock to concentration in 40m mixed layer
k_g	8.76^{-1}	yr^{-1}: Gas exchange piston velocity.

† This parameter is subject to inversion and treated as uncertain ($i = 2, 3$ only for ocean mixed layer export). The value listed here corresponds to the original SCCM documentation Raupach (2013); Harman et al. (2011).

Appendix A

Ocean Flux Supplement

A.1 Model Information

Table A.1: Coupled ocean-biogeochemistry models[1] and reanalysis forcings[2]

Model	Forcing	Resolution	Dates
MOM4p1-Bling	CORE-II	3°	1980-2006
	CORE-II-NY[3]	3°	1960-1980
	NCEP-1	3°	1980-2006
	ERA-40	3°	1980-2003
OPA-PISCES (A)	DRAKKAR	2°	1980-2006
OPA-PISCES (B) [4]	DRAKKAR	2°	1980-2006

[1] Models: See references Griffies et al. (2004); Galbraith et al. (2011); Aumont and Bopp (2006)

[2] Reanalysis Products: See references Large and Yeager (2009); Kalnay et al. (1996); Uppala et al. (2005); Brodeau et al. (2010)

[3] This simulation was run with the atmospheric CO_2 from 1980-2006, but with the climatological forcing of the ocean circulation.

[4] The two versions of the OPA-PISCES model use different parameterizations of mixed layer turbulence Rodgers et al. (2013).

Table A.2: Coupled CMIP5 ocean-atmosphere-biogeochemistry models[1]

Model	simulation	resolution °(lat,lon)
HadGEM2-CC	r1i1p1	1.9x1.3
HadGEM2-CC	r2i1p1	1.9x1.3
HADGEM2-ES	r1i1p1	1.9x1.3
GISS-E2-R	r1i1p1	1.0x1.3
GFDL-ESM2M	r1i1p1	1.0x1.0

[1] See references Bellouin et al. (2011); Schmidt et al. (2006); Dunne et al. (2013)

A.2 Timeseries

Verification of the individual cells in the MCMC inversion of LDEO2010 is a lengthy process. In this section, we show maps of the root mean squared error and some example posterior pCO_2 timeseries (green) and the LDEO2010 values (red) for major ocean regions. We focus our attention on the Southern Ocean south of 45S (c.f. fig. A.1), the Southern Ocean between 45S and 30S (c.f. fig. A.2), the Indian Ocean (c.f. fig. A.3), the Equatorial Pacific (c.f. fig. A.4), the North Pacific (c.f. fig. A.5), the Subpolar North Atlantic (c.f. fig. A.6) and the Subtropical North Atlantic (c.f. fig. A.7).

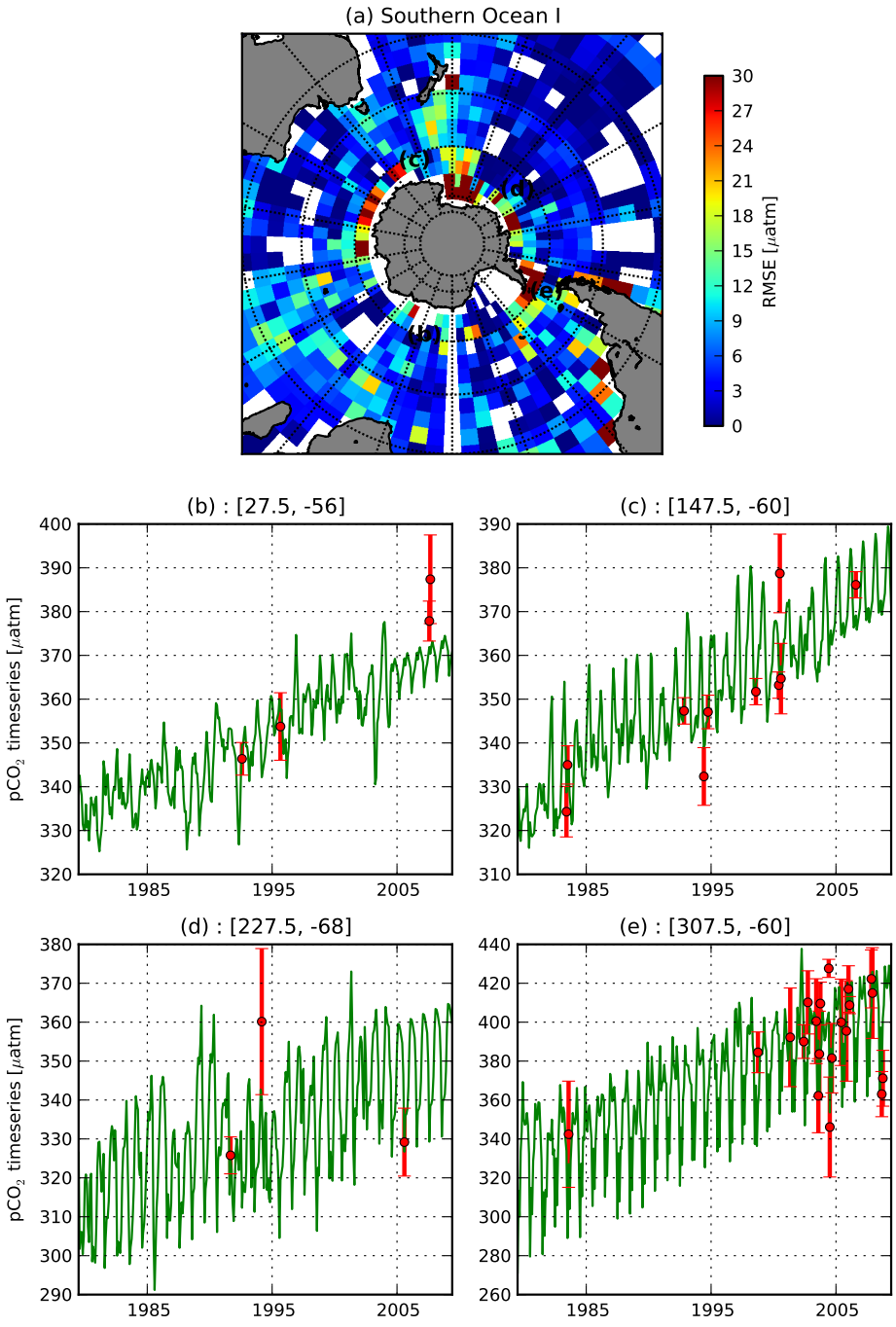

Figure A.1: Southern Ocean Results, < 45S: RMSE in region and 4 example timeseries

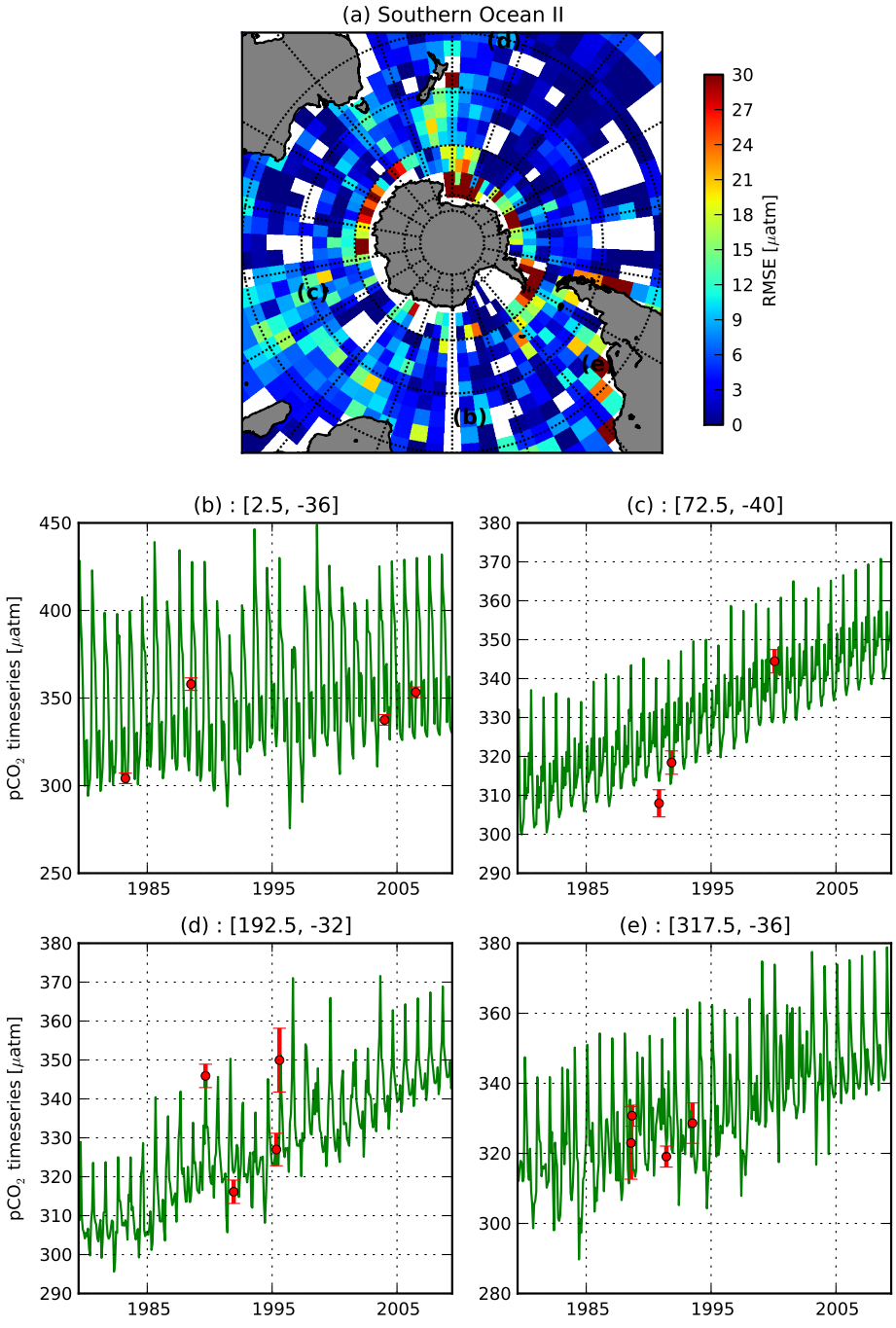

Figure A.2: Southern Ocean Results, <30S, >45S: RMSE in region and 4 example timeseries

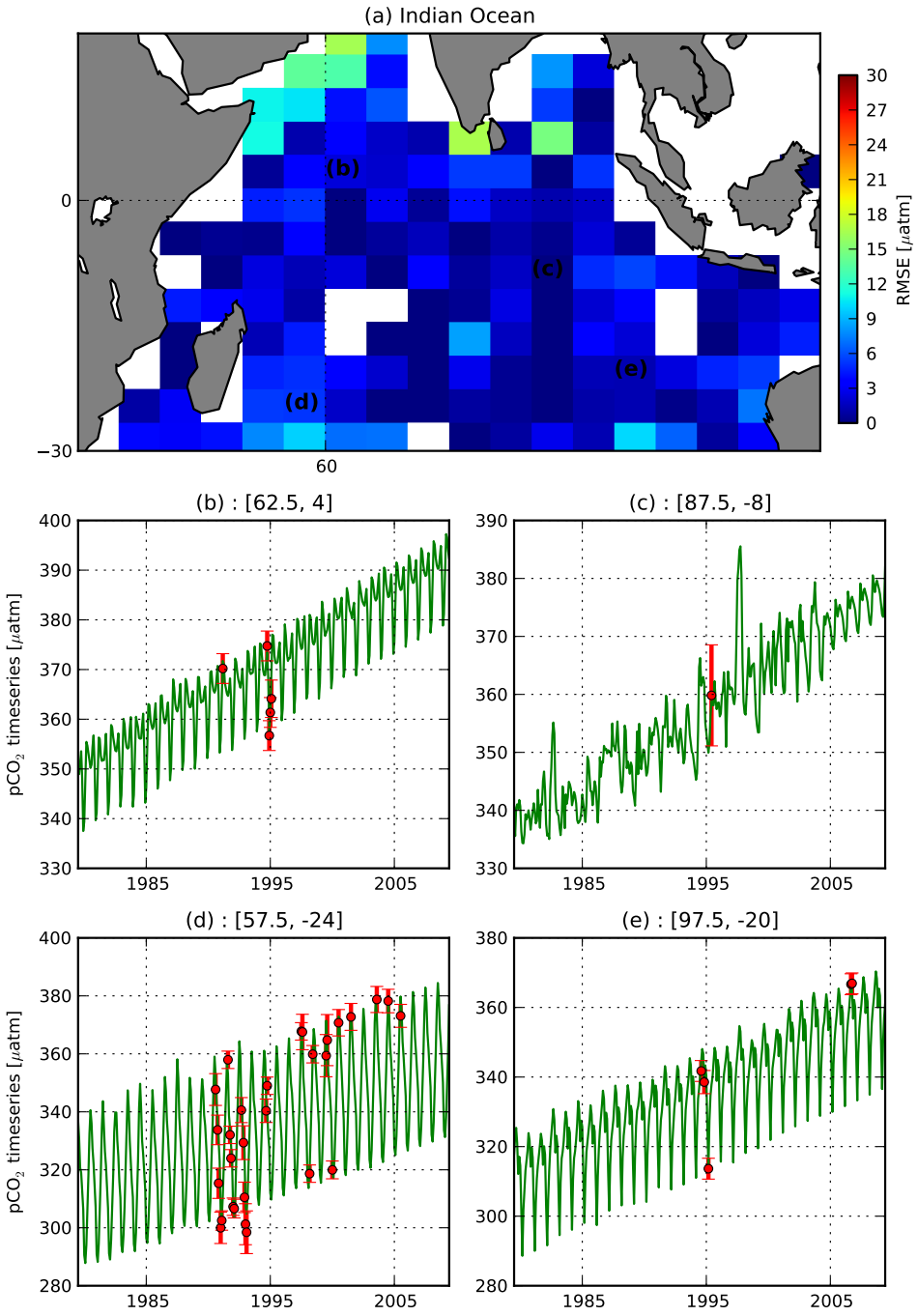

Figure A.3: Indian Ocean Results: RMSE in region and 4 example timeseries

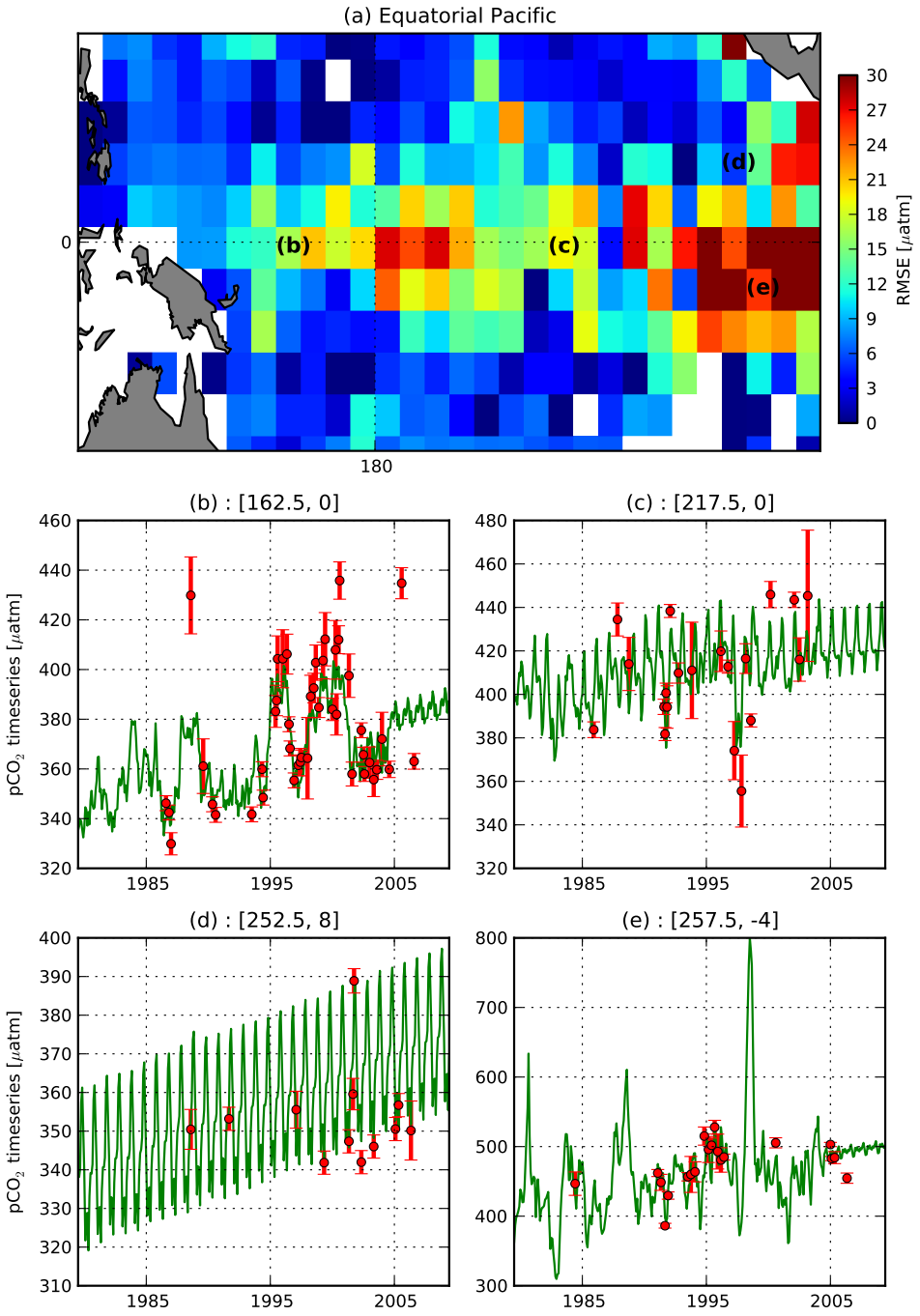

Figure A.4: Equatorial Pacific Results: RMSE in region and 4 example timeseries

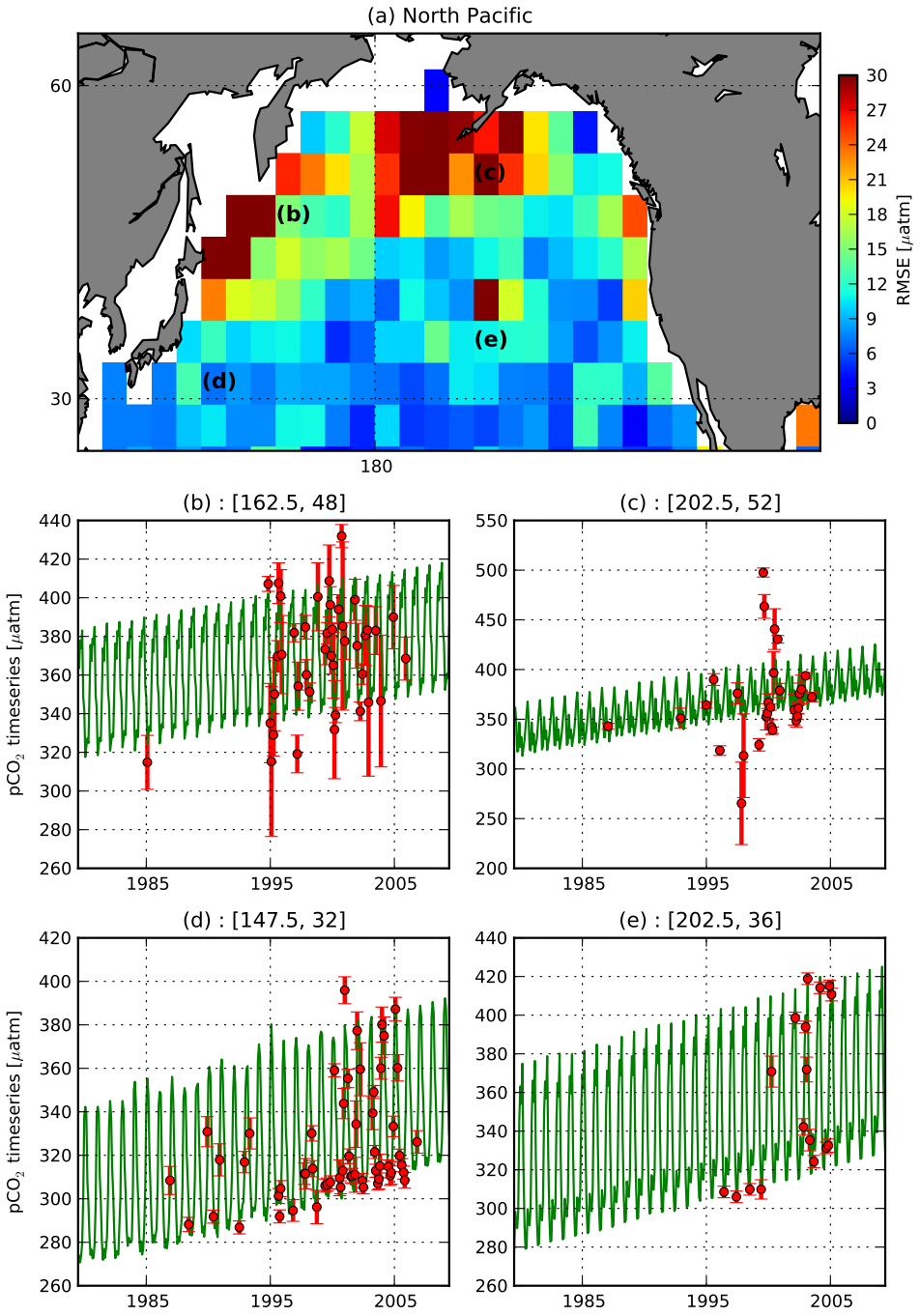

Figure A.5: North Pacific Results: RMSE in region and 4 example timeseries

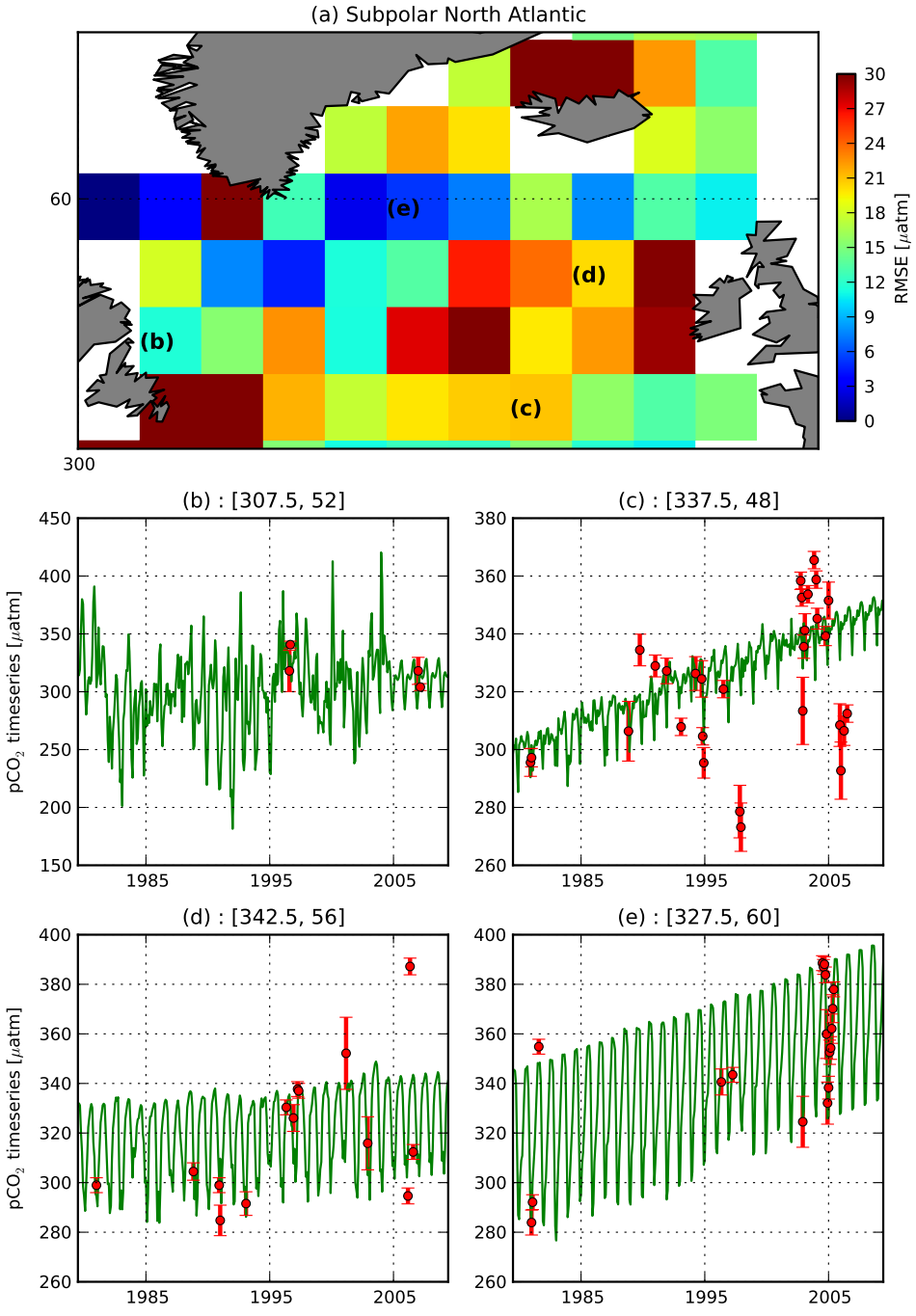

Figure A.6: Subpolar North Atlantic Results: RMSE in region and 4 example time-series

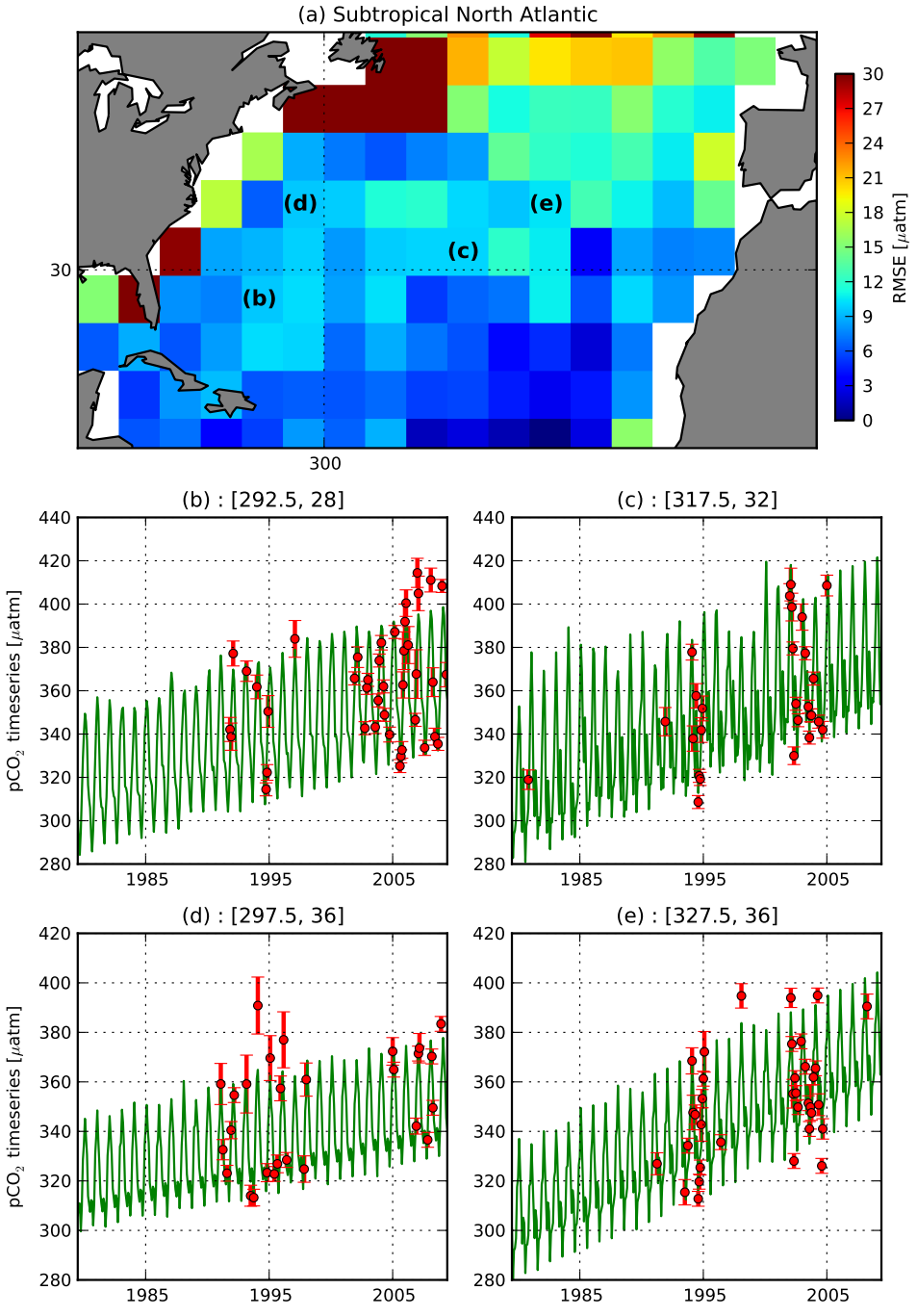

Figure A.7: Subtropical North Atlantic Results: RMSE in region and 4 example timeseries

A.3 Regional Trends and Fluxes

Here we list regionally compiled results from the MCMC inversion of LDEO2010. We use the regional maps from CARBONTRACKER Jacobson et al. (2007) to divide the ocean surface. The regions are shown in figure A.8. Table A.3 shows the regionally-averaged slope estimates for the MCMC results and the prior distribution. The error estimate in the slope measurement is reported in two ways. The first is by calculating the root sum of squares of the error of the cells in the region as traditional uncertainty analysis requires. This is reported as the $\pm\sigma$ bands in the slope estimates. We also show the standard error of the slope estimates over the region, which is the root sum of squares of the difference between each grid cell's estimate for A and the regional mean. This is meant to show the level of coherence in the estimate across each region.

Table A.4 shows the regional breakdown of the flux estimates. There we show the 10-yr averaged flux about the year 2000 into the different ocean regions, in PgC yr^{-1}, for the MCMC-derived pCO_2 fields. We also show the change in the flux into each region over the 30 year time period, 1980-2009, in the column $MCMC\Delta$, to give an indication of the importance of the time-varying nature of the pCO_2 history. For comparison, we also include the climatological fluxes from Takahashi et al. Takahashi et al. (2009a).

Tables A.5 and A.6 show the differences in the regional results of the MCMC sensitivity inversion cases.

Table A.3: pCO_2 Slope Estimates

Region	Area (%)	MCMC A	MCMC SE	Prior A	Prior SE
1.0	1.4	1.52 ± 1.06	0.0	1.54 ± 1.08	0.0
2.0	2.7	1.24 ± 0.54	0.1	1.32 ± 0.68	0.0
3.0	2.1	1.31 ± 0.45	0.2	1.37 ± 0.85	0.1
4.0	3.9	1.58 ± 0.38	0.1	1.52 ± 0.66	0.1
5.0	3.8	1.40 ± 0.42	0.1	1.46 ± 0.46	0.0
6.0	2.8	1.44 ± 0.67	0.1	1.38 ± 0.71	0.0
7.0	3.2	1.53 ± 0.59	0.1	1.41 ± 0.63	0.1
8.0	2.8	1.33 ± 0.45	0.1	1.36 ± 0.53	0.0
9.0	2.5	1.45 ± 0.43	0.0	1.44 ± 0.46	0.0
10.0	7.4	1.29 ± 0.63	0.0	1.22 ± 0.67	0.0
11.0	1.3	1.33 ± 0.52	0.1	1.43 ± 0.56	0.0
12.0	2.4	1.58 ± 0.39	0.1	1.63 ± 0.50	0.0
13.0	2.8	1.42 ± 0.39	0.1	1.48 ± 0.53	0.0
14.0	2.9	1.48 ± 0.39	0.1	1.60 ± 0.50	0.0
15.0	2.9	1.40 ± 0.43	0.1	1.52 ± 0.85	0.1
16.0	6.2	1.35 ± 0.45	0.1	1.53 ± 0.63	0.0
17.0	5.5	1.59 ± 0.58	0.1	1.29 ± 0.84	0.0
18.0	3.2	1.37 ± 0.46	0.1	1.40 ± 0.61	0.0
19.0	4.8	1.58 ± 0.72	0.1	1.47 ± 0.86	0.1
20.0	4.4	1.38 ± 0.44	0.1	1.44 ± 0.46	0.0
21.0	3.0	1.43 ± 0.60	0.1	1.57 ± 0.66	0.1
22.0	3.4	1.44 ± 0.45	0.0	1.42 ± 0.47	0.0
23.0	1.0	1.55 ± 0.42	0.1	1.56 ± 0.42	0.1
24.0	0.2	1.47 ± 0.45	0.1	1.57 ± 0.46	0.1
25.0	4.0	1.51 ± 0.39	0.0	1.51 ± 0.42	0.0
26.0	3.5	1.39 ± 0.63	0.1	1.35 ± 0.64	0.0
27.0	4.5	1.45 ± 0.54	0.0	1.39 ± 0.56	0.0
28.0	4.3	1.49 ± 0.45	0.1	1.44 ± 0.49	0.0
29.0	4.0	1.45 ± 0.47	0.0	1.43 ± 0.50	0.0
30.0	3.5	1.52 ± 0.40	0.0	1.45 ± 0.41	0.0
World	100.0	1.44 ± 0.56	0.0	1.43 ± 0.66	0.0

Table A.4: Regional Flux Estimates

Region	Area (%)	MCMC Flux [PgC]	MCMC Δ [PgCyr^{-1}]	Clim. Flux [PgC]
1.0	1.4	0.15 ± 0.03	0.0	0.06 ± 0.01
2.0	2.7	0.32 ± 0.06	0.1	0.27 ± 0.05
3.0	2.1	0.16 ± 0.03	0.1	0.13 ± 0.03
4.0	3.9	0.03 ± 0.01	-0.0	0.04 ± 0.01
5.0	3.8	-0.04 ± 0.01	0.0	-0.04 ± -0.01
6.0	2.8	-0.10 ± 0.02	0.0	-0.08 ± -0.02
7.0	3.2	-0.02 ± 0.00	0.0	-0.01 ± -0.00
8.0	2.8	0.21 ± 0.04	0.1	0.17 ± 0.03
9.0	2.5	0.11 ± 0.02	0.1	0.08 ± 0.02
10.0	7.4	0.06 ± 0.01	0.2	-0.05 ± -0.01
11.0	1.3	-0.03 ± 0.01	0.0	-0.00 ± -0.00
12.0	2.4	0.13 ± 0.03	0.0	0.14 ± 0.03
13.0	2.8	0.23 ± 0.05	0.1	0.24 ± 0.05
14.0	2.9	0.08 ± 0.02	0.0	0.09 ± 0.02
15.0	2.9	0.05 ± 0.01	0.0	0.04 ± 0.01
16.0	6.2	-0.05 ± 0.01	0.0	-0.03 ± -0.01
17.0	5.5	-0.11 ± 0.02	0.0	-0.14 ± -0.03
18.0	3.2	0.00 ± 0.00	0.0	-0.00 ± -0.00
19.0	4.8	-0.27 ± 0.05	-0.0	-0.29 ± -0.06
20.0	4.4	0.18 ± 0.04	0.1	0.16 ± 0.03
21.0	3.0	-0.04 ± 0.01	0.0	-0.03 ± -0.01
22.0	3.4	0.19 ± 0.04	0.1	0.18 ± 0.04
23.0	1.0	0.01 ± 0.00	0.0	0.00 ± 0.00
24.0	0.2	0.00 ± 0.00	0.0	0.01 ± 0.00
25.0	4.0	0.15 ± 0.03	0.0	0.10 ± 0.02
26.0	3.5	-0.08 ± 0.02	0.0	-0.09 ± -0.02
27.0	4.5	-0.03 ± 0.01	0.0	-0.03 ± -0.01
28.0	4.3	0.13 ± 0.03	0.0	0.13 ± 0.03
29.0	4.0	0.29 ± 0.06	0.1	0.29 ± 0.06
30.0	3.5	0.13 ± 0.03	0.1	0.10 ± 0.02
World	100.0	1.87 ± 0.37	1.2	1.42 ± 0.28

Table A.5: Regional Slope Sensitivity (μatm yr^{-1})

Region	Area (%)	IAV ΔA	SEAS ΔA
1.00	1.35	-0.01 ± 0.21	0.08 ± 0.49
2.00	2.67	0.03 ± 0.15	-0.10 ± 0.17
3.00	2.09	-0.02 ± 0.24	-0.05 ± 0.16
4.00	3.93	-0.00 ± 0.10	-0.01 ± 0.57
5.00	3.80	0.01 ± 0.08	-0.03 ± 0.09
6.00	2.75	0.04 ± 0.18	-0.02 ± 0.16
7.00	3.18	-0.06 ± 0.16	-0.01 ± 0.12
8.00	2.77	0.02 ± 0.12	-0.01 ± 0.11
9.00	2.46	-0.01 ± 0.10	-0.09 ± 0.14
10.00	7.40	0.00 ± 0.13	-0.00 ± 0.15
11.00	1.26	-0.02 ± 0.10	-0.12 ± 0.10
12.00	2.38	-0.01 ± 0.08	0.09 ± 0.09
13.00	2.85	-0.09 ± 0.08	0.06 ± 0.07
14.00	2.91	0.04 ± 0.08	0.00 ± 0.09
15.00	2.86	-0.06 ± 0.11	0.03 ± 0.10
16.00	6.19	-0.02 ± 0.11	0.03 ± 0.12
17.00	5.46	0.08 ± 0.19	-0.05 ± 0.20
18.00	3.20	-0.06 ± 0.13	0.00 ± 0.13
19.00	4.83	0.04 ± 0.19	-0.09 ± 0.21
20.00	4.42	0.00 ± 0.09	-0.01 ± 0.09
21.00	2.99	0.01 ± 0.11	0.02 ± 0.17
22.00	3.36	0.00 ± 0.10	-0.00 ± 0.09
23.00	1.04	0.01 ± 0.07	-0.01 ± 0.07
24.00	0.17	-0.00 ± 0.08	0.02 ± 0.07
25.00	3.95	-0.01 ± 0.08	-0.04 ± 0.09
26.00	3.51	-0.00 ± 0.11	0.04 ± 0.12
27.00	4.46	0.01 ± 0.13	0.02 ± 0.11
28.00	4.27	0.00 ± 0.08	-0.06 ± 0.09
29.00	3.98	-0.02 ± 0.09	-0.00 ± 0.09
30.00	3.49	-0.00 ± 0.08	0.02 ± 0.08
World	100.00	-0.00 ± 0.14	-0.01 ± 0.27

Table A.6: Regional Flux Sensitivity (1e-3 PgC yr^{-1})

Region	Area (%)	IAV Δ Φ	SEAS $\Delta\Phi$
1.00	1.35	-1.92 ± 0.38	-6.90 ± 0.38
2.00	2.67	10.38 ± 2.08	10.65 ± 2.08
3.00	2.09	-1.13 ± 0.23	-6.31 ± 0.23
4.00	3.93	-0.73 ± 0.15	-1.12 ± 0.15
5.00	3.80	-3.50 ± 0.70	3.71 ± 0.70
6.00	2.75	0.64 ± 0.13	-0.58 ± 0.13
7.00	3.18	2.12 ± 0.42	-3.35 ± 0.42
8.00	2.77	3.17 ± 0.63	-16.88 ± 0.63
9.00	2.46	2.87 ± 0.57	-12.40 ± 0.57
10.00	7.40	-5.55 ± 1.11	-54.96 ± 1.11
11.00	1.26	0.68 ± 0.14	-17.37 ± 0.14
12.00	2.38	-1.61 ± 0.32	2.52 ± 0.32
13.00	2.85	-0.52 ± 0.10	-13.91 ± 0.10
14.00	2.91	2.69 ± 0.54	-6.92 ± 0.54
15.00	2.86	-0.57 ± 0.11	-2.27 ± 0.11
16.00	6.19	-5.22 ± 1.04	-8.88 ± 1.04
17.00	5.46	-5.76 ± 1.15	-14.05 ± 1.15
18.00	3.20	-2.81 ± 0.56	-6.87 ± 0.56
19.00	4.83	-7.54 ± 1.51	4.21 ± 1.51
20.00	4.42	-1.35 ± 0.27	1.95 ± 0.27
21.00	2.99	3.55 ± 0.71	-14.00 ± 0.71
22.00	3.36	0.32 ± 0.06	-7.82 ± 0.06
23.00	1.04	1.95 ± 0.39	-13.86 ± 0.39
24.00	0.17	0.10 ± 0.02	-0.92 ± 0.02
25.00	3.95	-3.16 ± 0.63	6.72 ± 0.63
26.00	3.51	1.36 ± 0.27	-6.37 ± 0.27
27.00	4.46	-0.79 ± 0.16	-9.00 ± 0.16
28.00	4.27	0.65 ± 0.13	-7.93 ± 0.13
29.00	3.98	-3.35 ± 0.67	-14.29 ± 0.67
30.00	3.49	-2.73 ± 0.55	-18.35 ± 0.55
World	100.00	-17.74 ± 3.55	-235.55 ± 47.11

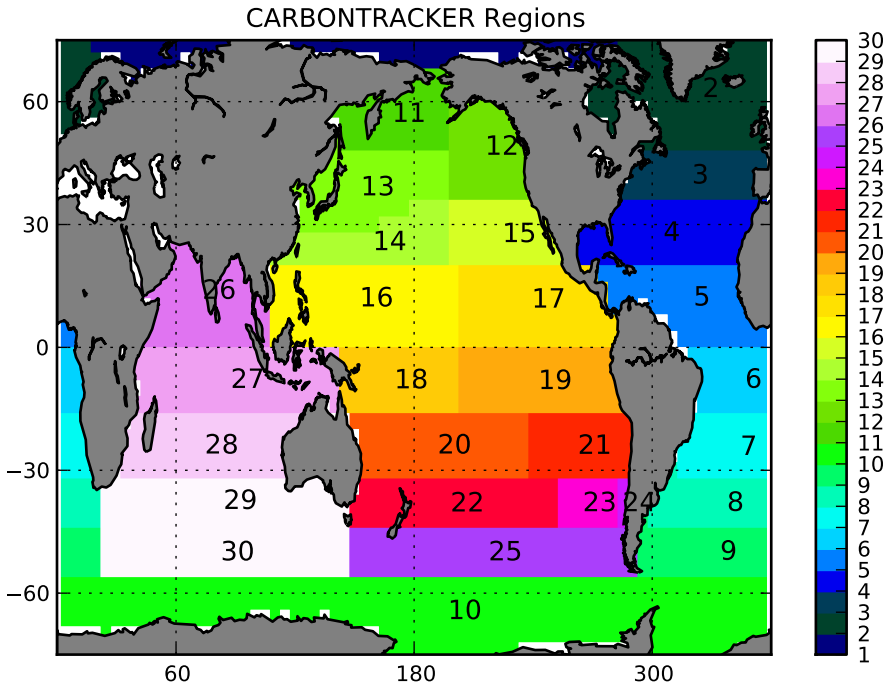

Figure A.8: The CARBONTRACKER regions used for dividing the ocean are mapped and labeled in this figure.

Bibliography

Ammann, C.M., Meehl, G.A., Washington, W.M., and Zender, C.S. A monthly and latitudinally varying volcanic forcing dataset in simulations of 20th century climate. *Geophysical Research Letters*, 30(12):pp. n/a, 2003. ISSN 1944-8007. doi: 10.1029/2003GL016875

Anav, A., Friedlingstein, P., Kidston, M., Bopp, L., Ciais, P., Cox, P., et al. Evaluating the Land and Ocean Components of the Global Carbon Cycle in the CMIP5 Earth System Models. *Journal of Climate*, 26(18):pp. 6801, 2013. ISSN 0894-8755. doi:10.1175/JCLI-D-12-00417.1

Anthoff, D., Rose, S., Tol, R.S.J., and Waldhoff, S. The time evolution of the social cost of carbon: An application of fund. Economics Discussion Paper 2011-44, Kiel Institute for the World Economy, 2011

Archer, D., Eby, M., Brovkin, V., Ridgwell, A., Cao, L., Mikolajewicz, U., et al. Atmospheric lifetime of fossil fuel carbon dioxide. *Annual Review of Earth and Planetary Sciences*, 37(1):p. 117, 2009

Arora, V., Scinocca, J., Boer, G., Christian, J., Denman, K., Flato, G., et al. Carbon emission limits required to satisfy future representative concentration pathways of greenhouse gases. *Geophysical Research Letters*, 38(5), 2011

Arora, V.K., Boer, G.J., Friedlingstein, P., Eby, M., Jones, C.D., Christian, J.R., et al. Carbon–Concentration and Carbon–Climate Feedbacks in CMIP5 Earth System Models. *Journal of Climate*, 26(15):pp. 5289, 2013. ISSN 0894-8755. doi: 10.1175/JCLI-D-12-00494.1

Aumont, O. and Bopp, L. Globalizing results from ocean in situ iron fertilization studies. *Global Biogeochemical Cycles*, 20(2), 2006

Ballantyne, A., Alden, C., Miller, J., Tans, P., and White, J. Increase in observed net carbon dioxide uptake by land and oceans during the past 50 years. *Nature*, 488(7409):pp. 70, 2012

Bates, N.R. Interannual variability of the oceanic co2 sink in the subtropical gyre of the north atlantic ocean over the last 2 decades. *Journal of Geophysical Research*, 112(C9):p. C09013, 2007

Bellouin, N., Collins, W., Culverwell, I., Halloran, P., Hardiman, S., Hinton, T., et al. The hadgem2 family of met office unified model climate configurations. *Geoscientific Model Development Discussions*, 4(2):pp. 765, 2011

Bodman, R.W., Rayner, P.J., and Karoly, D.J. Uncertainty in temperature projections reduced using carbon cycle and climate observations. *Nature Clim. Change*, 3(8):pp. 725, 2013. ISSN 1758-678X

Brodeau, L., Barnier, B., Treguier, A.M., Penduff, T., and Gulev, S. An era40-based atmospheric forcing for global ocean circulation models. *Ocean Modelling*, 31(3):pp. 88, 2010

Caldeira, K. and Duffy, P.B. The Role of the Southern Ocean in Uptake and Storage of Anthropogenic Carbon Dioxide. *Science*, 287(5453):pp. 620, 2000

Callendar, G.S. The artificial production of carbon dioxide and its influence on temperature. *Quarterly Journal of the Royal Meteorological Society*, 64(275):pp. 223, 1938

Ciais, P., Sabine, C.L., Bala, G., Bopp, L., Brovkin, V., Canadell, J.G., et al. Carbon and other biogeochemical cycles. In *Climate Change 2013: The Physical Science Basis Contribution of Working Group I to the Fifth Assessment Report of the Intergovernmental Panel on Climate Change*. Cambridge University Press, 2013

Ciasto, L.M. and Thompson, D.W. Observations of large-scale ocean-atmosphere interaction in the southern hemisphere. *Journal of Climate*, 21(6):pp. 1244, 2008

Cullison Gray, S.E., DeGrandpre, M.D., Moore, T.S., Martz, T.R., Friederich, G.E., and Johnson, K.S. Applications of in situ pH measurements for inorganic carbon calculations. *Marine Chemistry*, 125(1–4):pp. 82, 2011. ISSN 0304-4203. doi: http://dx.doi.org/10.1016/j.marchem.2011.02.005

Dietz, S. The treatment of risk and uncertainty in the us social cost of carbon for regulatory impact analysis. *Economics: The Open-Access, Open-Assessment E-Journal*, 6(2012-18), 2012. doi:10.5018/economics-ejournal.ja.2012-18

Doney, S.C., Tilbrook, B., Roy, S., Metzl, N., Le Quéré, C., Hood, M., Feely, R.A., and Bakker, D. Surface-ocean co¡ sub¿ 2¡/sub¿ variability and vulnerability. *Deep Sea Research Part II: Topical Studies in Oceanography*, 56(8):pp. 504, 2009

Dore, J.E., Lukas, R., Sadler, D.W., Church, M.J., and Karl, D.M. Physical and biogeochemical modulation of ocean acidification in the central north pacific. *Proceedings of the National Academy of Sciences*, 106(30):pp. 12235, 2009

Dufour, C.O., Sommer, J.L., Gehlen, M., Orr, J.C., Molines, J.M., Simeon, J., and Barnier, B. Eddy compensation and controls of the enhanced sea-to-air CO2 flux during positive phases of the Southern Annular Mode. *Global Biogeochemical Cycles*, 27(3):pp. 950, 2013. ISSN 1944-9224. doi:10.1002/gbc.20090

Dufresne, J.L., Foujols, M.A., Denvil, S., Caubel, A., Marti, O., Aumont, O., et al. Climate change projections using the ipsl-cm5 earth system model: from cmip3 to cmip5. *Climate Dynamics*, 40(9-10):pp. 2123, 2013

Dunne, J.P., John, J.G., Adcroft, A.J., Griffies, S.M., Hallberg, R.W., Shevliakova, E., et al. GFDL's ESM2 Global Coupled Climate–Carbon Earth System Models. Part I: Physical Formulation and Baseline Simulation Characteristics. *Journal of Climate*, 25(19):pp. 6646, 2012. ISSN 0894-8755. doi:10.1175/JCLI-D-11-00560.1

Dunne, J.P., John, J.G., Shevliakova, E., Stouffer, R.J., Krasting, J.P., Malyshev, S.L., et al. Gfdl's esm2 global coupled climate–carbon earth system models. part ii: Carbon system formulation and baseline simulation characteristics*. *Journal of Climate*, 26(7):pp. 2247, 2013

EPA, U. Regulatory impact analysis for the proposed carbon pollution guidelines for existing power plants and emissions standards for modified and reconstructed power plants. Technical report, U.S. Environmental Protection Agency, Office of Air Quality Planning and Standards, 2014

Etheridge, D., Steele, L., Langenfelds, R., Francey, R., Barnola, J., and Morgan, V. Historical co2 records from the law dome de08, de08-2, and dss ice cores. *Trends: a compendium of data on global change*, pp. 351–364, 1998

Fay, A.R. and McKinley, G.A. Global trends in surface ocean pco2 from in situ data. *Global Biogeochemical Cycles*, 27(2):pp. 541, 2013. ISSN 1944-9224. doi: 10.1002/gbc.20051

Feely, R., Takahashi, T., Wanninkhof, R., McPhaden, M., Cosca, C., Sutherland, S., and Carr, M.E. Decadal variability of the air-sea co2 fluxes in the equatorial pacific ocean. *Journal of Geophysical Research: Oceans (1978–2012)*, 111(C8), 2006

Friedlingstein, P., Cox, P., Betts, R., Bopp, L., von Bloh, W., Brovkin, V., et al. Climate–Carbon Cycle Feedback Analysis: Results from the C 4 MIP Model Intercomparison. *Journal of Climate*, 19(14):pp. 3337, 2006. ISSN 0894-8755. doi: 10.1175/JCLI3800.1

Friedlingstein, P., Meinshausen, M., Arora, V.K., Jones, C.D., Anav, A., Liddicoat, S.K., and Knutti, R. Uncertainties in CMIP5 Climate Projections due to Carbon Cycle Feedbacks. *Journal of Climate*, 27(2):pp. 511, 2013. ISSN 0894-8755. doi: 10.1175/JCLI-D-12-00579.1

Frölicher, T., Sarmiento, J., Paynter, D., Dunne, J., and Winton, M. Carbon and heat uptake in the cmip5 models: The dominance of the southern ocean. *submitted to Journal of Climate*, 2014

Frölicher, T.L., Joos, F., Raible, C.C., and Sarmiento, J.L. Atmospheric co2 response to volcanic eruptions: The role of enso, season, and variability. *Global Biogeochemical Cycles*, 27(1):pp. 239, 2013. ISSN 1944-9224. doi:10.1002/gbc.20028

Galbraith, E.D., Gnanadesikan, A., Dunne, J.P., and Hiscock, M.R. Regional impacts of iron-light colimitation in a global biogeochemical model. *Biogeosciences*, 7(3):pp. 1043, 2010. doi:10.5194/bg-7-1043-2010

Galbraith, E.D., Kwon, E.Y., Gnanadesikan, A., Rodgers, K.B., Griffies, S.M., Bianchi, D., et al. Climate variability and radiocarbon in the cm2mc earth system model. *Journal of Climate*, 24(16):pp. 4230, 2011

Geiderl, R.J., Maclntyre, H.L., and Kana, T.M. A dynamic regulatory model of phytoplanktonic acclimation to light, nutrients, and temperature. *Limnol. Oceanogr*, 43(4):pp. 679, 1998

Geweke, J. *Evaluating the accuracy of sampling-based approaches to the calculation of posterior moments*, volume 196. Federal Reserve Bank of Minneapolis, Research Department, 1991

Gille, S.T. Decadal-scale temperature trends in the southern hemisphere ocean. *Journal of Climate*, 21(18):pp. 4749, 2008

Griffies, S.M., Harrison, M.J., Pacanowski, R.C., and Rosati, A. A technical guide to MOM4. Technical report, 2004

Gruber, N., Gloor, M., Mikaloff Fletcher, S.E., Doney, S.C., Dutkiewicz, S., Follows, M.J., et al. Oceanic sources, sinks, and transport of atmospheric CO2. *Global Biogeochemical Cycles*, 23(1):p. GB1005, 2009. ISSN 1944-9224. doi: 10.1029/2008GB003349

Hallberg, R. and Gnanadesikan, A. The Role of Eddies in Determining the Structure and Response of the Wind-Driven Southern Hemisphere Overturning: Results from the Modeling Eddies in the Southern Ocean (MESO) Project. *Journal of Physical Oceanography*, 36(12):pp. 2232, 2006. ISSN 0022-3670. doi:10.1175/JPO2980.1

Hansen, J., Ruedy, R., Sato, M., and Lo, K. Global surface temperature change. *Reviews of Geophysics*, 48(4):pp. n/a, 2010. ISSN 1944-9208. doi:10.1029/2010RG000345

Harman, I., Trudinger, C., and Raupach, M. Sccm–the simple carbon-climate model: Technical documentation. Technical report, 2011

Hastings, W.K. Monte carlo sampling methods using markov chains and their applications. *Biometrika*, 57(1):pp. 97, 1970

Hauck, J., Völker, C., Wang, T., Hoppema, M., Losch, M., and Wolf-Gladrow, D.A. Seasonally different carbon flux changes in the Southern Ocean inresponse to the southern annular mode. *Global Biogeochemical Cycles*, 27(4):pp. 1236, 2013. ISSN 1944-9224. doi:10.1002/2013GB004600

Hof, A.F., Hope, C.W., Lowe, J., Mastrandrea, M.D., Meinshausen, M., and van Vuuren, D.P. The benefits of climate change mitigation in integrated assessment models: the role of the carbon cycle and climate component. *Climatic change*, 113(3-4):pp. 897, 2012

Hogg, A.M.C., Meredith, M.P., Blundell, J.R., and Wilson, C. Eddy heat flux in the southern ocean: Response to variable wind forcing. *Journal of Climate*, 21(4):pp. 608, 2008

Houghton, R., House, J., Pongratz, J., van der Werf, G., DeFries, R., Hansen, M., Quéré, C.L., and Ramankutty, N. Carbon emissions from land use and land-cover change. *Biogeosciences*, 9(12):pp. 5125, 2012

Interagency Working Group on the Social Cost of Carbon, U. Appendix 15a. social cost of carbon for regulatory impact analysis under executive order 12866. Technical report, U.S. Department of Energy, 2010

Ishii, M., Saito, S., Tokieda, T., Kawano, T., Matsumoto, K., and Inoue, H.Y. Variability of surface layer co2 parameters in the western and central equatorial pacific. *Global Environmental Changes in the Ocean and on Land, Eds., M. Shiyomi, H. Kawahata. H. Koizumi, A. Tsuda, and Y. Awaya, TERRAPUB, Tokyo*, pp. 59–94, 2004

Ito, A. A historical meta-analysis of global terrestrial net primary productivity: are estimates converging? *Global Change Biology*, 17(10):pp. 3161, 2011

Jacobson, A.R., Fletcher, S.E.M., Gruber, N., Sarmiento, J.L., and Gloor, M. A joint atmosphere-ocean inversion for surface fluxes of carbon dioxide: 2. regional results. *Global Biogeochemical Cycles*, 21(1):p. GB1020, 2007

Jain, A.K., Meiyappan, P., Song, Y., and House, J.I. Co2 emissions from land-use change affected more by nitrogen cycle, than by the choice of land-cover data. *Global change biology*, 19(9):pp. 2893, 2013

Johnson, K.S., Berelson, W.M., Boss, E.S., Chase, Z., Claustre, H., Emerson, S.R., et al. Observing biogeochemical cycles at global scales with profiling floats and gliders: Prospects for a global array. *Oceanography*, 22(3):pp. 216, 2009. doi: http://dx.doi.org/10.5670/oceanog.2009.81

Johnson, K.S., Riser, S.C., and Karl, D.M. Nitrate supply from deep to near-surface waters of the North Pacific subtropical gyre. *Nature*, 465(7301):pp. 1062, 2010. ISSN 0028-0836

Jones, C.D. and Cox, P.M. Modeling the volcanic signal in the atmospheric co2 record. *Global Biogeochemical Cycles*, 15(2):pp. 453, 2001. ISSN 1944-9224. doi: 10.1029/2000GB001281

Joos, F., Bruno, M., Fink, R., Siegenthaler, U., Stocker, T., Le Quéré, C., and Sarmiento, J. An efficient and accurate representation of complex oceanic and biospheric models of anthropogenic carbon uptake. *Tellus B*, 48(3):pp. 397, 1996. ISSN 1600-0889. doi:10.1034/j.1600-0889.1996.t01-2-00006.x

Joos, F., Roth, R., Fuglestvedt, J., Peters, G., Enting, I., Bloh, W.v., et al. Carbon dioxide and climate impulse response functions for the computation of greenhouse gas metrics: a multi-model analysis. *Atmospheric Chemistry and Physics*, 13(5):pp. 2793, 2013

Kalnay, E., Kanamitsu, M., Kistler, R., Collins, W., Deaven, D., Gandin, L., et al. The NCEP/NCAR 40-Year Reanalysis Project. *Bulletin of the American Meteorological Society*, 77(3):pp. 437, 1996. ISSN 0003-0007. doi:10.1175/1520-0477(1996)077⟨0437:TNYRP⟩2.0.CO;2

Kamenkovich, I., Cheng, W., Schmid, C., and Harrison, D.E. Effects of eddies on an ocean observing system with profiling floats: Idealized simulations of the Argo array. *Journal of Geophysical Research: Oceans*, 116(C6):p. C06003, 2011. ISSN 2156-2202. doi:10.1029/2010JC006910

Keeling, C.D., Piper, S.C., Bacastow, R.B., Wahlen, M., Whorf, T.P., Heimann, M., and Meijer, H.A. Exchanges of atmospheric co2 and 13co2 with the terrestrial biosphere and oceans from 1978 to 2000. i. global aspects. Technical Report SIO Report Series, 01-06, Scripps Institute of Oceanography, San Diego, 2001

Keller, K., Bolker, B.B., and Bradford, D.F. Uncertain climate thresholds and optimal economic growth. *Journal of Environmental Economics and Management*, 48(1):pp. 723 , 2004. ISSN 0095-0696. doi:http://dx.doi.org/10.1016/j.jeem.2003.10.003

Khatiwala, S., Primeau, F., and Hall, T. Reconstruction of the history of anthropogenic co2 concentrations in the ocean. *Nature*, 462(7271):pp. 346, 2009

Kopp, R. and Mignone, B. Circumspection, reciprocity, and optimal carbon prices. *Climatic Change*, 120(4):pp. 831, 2013. ISSN 0165-0009. doi:10.1007/s10584-013-0858-5

Kopp, R.E. and Mignone, B.K. The u.s. government's social cost of carbon estimates after their first two years: Pathways for improvement. *Economics: The Open-Access, Open-Assessment E-Journal*, 6(2012-15), 2012. doi:10.5018/economics-ejournal.ja.2012-15

Kopp, R.E., Golub, A., Keohane, N.O., and Onda, C. The influence of the specification of climate change damages on the social cost of carbon. *Economics: The Open-Access, Open-Assessment E-Journal*, 6(2012-13), 2012. doi:10.5018/economics-ejournal.ja.2012-13

Kousky, C., Kopp, R.E., and Cooke, R.M. Risk premia and the social cost of carbon: a review. *Economics: The Open-Access, Open-Assessment E-Journal*, 5(2011-21):pp. 1, 2011

Large, W. and Yeager, S. The global climatology of an interannually varying air–sea flux data set. *Climate Dynamics*, 33(2-3):pp. 341, 2009

Le Quéré, C., Rödenbeck, C., Buitenhuis, E.T., Conway, T.J., Langenfelds, R., Gomez, A., et al. Saturation of the Southern Ocean CO2 Sink Due to Recent Climate Change. *Science*, 316(5832):pp. 1735, 2007. doi:10.1126/science.1136188

Le Quere, C., Raupach, M.R., Canadell, J.G., and Marland et al., G. Trends in the sources and sinks of carbon dioxide. *Nature Geosci*, 2(12):pp. 831, 2009. ISSN 1752-0894

Le Quéré, C., Takahashi, T., Buitenhuis, E.T., Rödenbeck, C., and Sutherland, S.C. Impact of climate change and variability on the global oceanic sink of CO2. *Global Biogeochemical Cycles*, 24(4):p. GB4007, 2010. ISSN 1944-9224. doi: 10.1029/2009GB003599

Le Quéré, C., Peters, G.P., Andres, R.J., Andrew, R.M., Boden, T., Ciais, P., et al. Global carbon budget 2013. *Earth System Science Data Discussions*, 6(2):pp. 689, 2013. doi:10.5194/essdd-6-689-2013

Le Quéré, C., Peters, G.P., Andres, R.J., Andrew, R.M., Boden, T.A., Ciais, P., et al. Global carbon budget 2013. *Earth System Science Data*, 6(1):pp. 235, 2014. doi:10.5194/essd-6-235-2014

Lee, K., Tong, L.T., Millero, F.J., Sabine, C.L., Dickson, A.G., Goyet, C., et al. Global relationships of total alkalinity with salinity and temperature in surface waters of the world's oceans. *Geophysical Research Letters*, 33(19):p. L19605, 2006. ISSN 1944-8007. doi:10.1029/2006GL027207

Lenton, A. and Matear, R.J. Role of the Southern Annular Mode (SAM) in Southern Ocean CO2 uptake. *Global Biogeochemical Cycles*, 21(2):p. GB2016, 2007. ISSN 1944-9224. doi:10.1029/2006GB002714

Lenton, A., Matear, R.J., and Tilbrook, B. Design of an observational strategy for quantifying the Southern Ocean uptake of CO2. *Global Biogeochemical Cycles*, 20(4):p. GB4010, 2006. ISSN 1944-9224. doi:10.1029/2005GB002620

Lenton, A., Metzl, N., Takahashi, T., Kuchinke, M., Matear, R.J., Roy, T., et al. The observed evolution of oceanic pco2 and its drivers over the last two decades. *Global Biogeochemical Cycles*, 26(2), 2012

Lenton, A., Tilbrook, B., Law, R.M., Bakker, D., Doney, S.C., Gruber, N., et al. Sea–air CO2 fluxes in the Southern Ocean for the period 1990-2009. *Biogeosciences*, 10(6):pp. 4037, 2013. doi:10.5194/bg-10-4037-2013

Li, Q.P., Franks, P.J.S., Landry, M.R., Goericke, R., and Taylor, A.G. Modeling phytoplankton growth rates and chlorophyll to carbon ratios in California coastal and pelagic ecosystems. *Journal of Geophysical Research: Biogeosciences*, 115(G4):p. G04003, 2010. ISSN 2156-2202. doi:10.1029/2009JG001111

Lindsay, K., Bonan, G., Doney, S., Hoffman, F., Lawrence, D., Long, M., et al. Preindustrial control and 20th century carbon cycle experiments with the earth system model cesm1-(bgc). *J. Climate*, 2013

Lovenduski, N.S. and Ito, T. The future evolution of the Southern Ocean CO2 sink. *Journal of Marine Research*, 67(5):pp. 597, 2009. ISSN 0022-2402. doi: 10.1357/002224009791218832

Lovenduski, N.S., Gruber, N., Doney, S.C., and Lima, I.D. Enhanced CO2 outgassing in the Southern Ocean from a positive phase of the Southern Annular Mode. *Global Biogeochemical Cycles*, 21(2):p. GB2026, 2007. ISSN 1944-9224. doi:10.1029/2006GB002900

Lovenduski, N.S., Gruber, N., and Doney, S.C. Toward a mechanistic understanding of the decadal trends in the southern ocean carbon sink. *Global Biogeochemical Cycles*, 22(3):p. GB3016, 2008

Lovenduski, N.S., Long, M.C., Gent, P.R., and Lindsay, K. Multi-decadal trends in the advection and mixing of natural carbon in the Southern Ocean. *Geophysical Research Letters*, 40(1):pp. 139, 2013. ISSN 1944-8007. doi:10.1029/2012GL054483

Luo, Y., Melillo, J., Niu, S., Beier, C., Clark, J.S., Classen, A.T., et al. Coordinated approaches to quantify long-term ecosystem dynamics in response to global change. *Global Change Biology*, 17(2):pp. 843, 2011

Maier-Reimer, E. and Hasselmann, K. Transport and storage of co2 in the ocean——an inorganic ocean-circulation carbon cycle model. *Climate dynamics*, 2(2):pp. 63, 1987

Majkut, J.D., Sarmiento, J.L., and Rodgers, K.B. A growing oceanic carbon uptake: Results from an inversion study of surface pCO2 data. *Global Biogeochemical Cycles*, 2014a. ISSN 1944-9224. doi:10.1002/2013GB004585

Majkut, J.D., Carter, B.R., Frölicher, T.L., Dufour, C.O., Rodgers, K.B., and Sarmiento, J.L. An observing system simulation for southern ocean carbon dioxide uptake. *Philosophical Transactions of the Royal Society A: Mathematical, Physical and Engineering Sciences*, 372(2019):p. 20130046, 2014b

Marshall, J. and Speer, K. Closure of the meridional overturning circulation through Southern Ocean upwelling. *Nature Geosci*, 5(3):pp. 171, 2012. ISSN 1752-0894

McKinley, G., Takahashi, T., Buitenhuis, E., Chai, F., Christian, J., Doney, S., et al. North pacific carbon cycle response to climate variability on seasonal to decadal timescales. *Journal of geophysical research*, 111(C7):p. C07S06, 2006

McKinley, G.A., Fay, A.R., Takahashi, T., and Metzl, N. Convergence of atmospheric and north atlantic carbon dioxide trends on multidecadal timescales. *Nature geoscience*, 4(9):pp. 606, 2011

Meinshausen, M., Raper, S.C.B., and Wigley, T.M.L. Emulating coupled atmosphere-ocean and carbon cycle models with a simpler model, magicc6 – part 1: Model description and calibration. *Atmospheric Chemistry and Physics*, 11(4):pp. 1417, 2011a. doi:10.5194/acp-11-1417-2011

Meinshausen, M., Smith, S., Calvin, K., Daniel, J., Kainuma, M., Lamarque, J.F., et al. The rcp greenhouse gas concentrations and their extensions from 1765 to 2300. *Climatic Change*, 109(1-2):pp. 213, 2011b. ISSN 0165-0009. doi:10.1007/s10584-011-0156-z

Meredith, M.P., Schofield, O., Newman, L., Urban, E., and Sparrow, M. The vision for a Southern Ocean Observing System. *Current Opinion in Environmental Sustainability*, 5(3–4):pp. 306, 2013. ISSN 1877-3435. doi:http://dx.doi.org/10.1016/j.cosust.2013.03.002

Metropolis, N., Rosenbluth, A.W., Rosenbluth, M.N., Teller, A.H., and Teller, E. Equation of state calculations by fast computing machines. *The Journal of Chemical Physics*, 21(6):pp. 1087, 1953. doi:http://dx.doi.org/10.1063/1.1699114

Metzl, N. Decadal increase of oceanic carbon dioxide in Southern Indian Ocean surface waters (1991–2007). *Deep Sea Research Part II: Topical Studies in Oceanography*, 56(8–10):pp. 607, 2009. ISSN 0967-0645. doi:http://dx.doi.org/10.1016/j.dsr2.2008.12.007

Mikaloff Fletcher, S.E., Gruber, N., Jacobson, A.R., Doney, S.C., Dutkiewicz, S., Gerber, M., et al. Inverse estimates of anthropogenic CO2 uptake, transport, and storage by the ocean. *Global Biogeochemical Cycles*, 20(2):p. GB2002, 2006. ISSN 1944-9224. doi:10.1029/2005GB002530

Morrison, A.K. and Hogg, A. On the Relationship between Southern Ocean Overturning and ACC Transport. *Journal of Physical Oceanography*, 43(1):pp. 140, 2012. ISSN 0022-3670. doi:10.1175/JPO-D-12-057.1

Newbold, S., Griffiths, C., Moore, C.C., Wolverton, A., and Kopits, E. The "social cost of carbon" made simple. NCEE Working Paper Series 201007, National Center for Environmental Economics, U.S. Environmental Protection Agency, 2010

Newbold, S.C. and Marten, A.L. The value of information for integrated assessment models of climate change. *Journal of Environmental Economics and Management*, 68(1):pp. 111 , 2014. ISSN 0095-0696. doi:http://dx.doi.org/10.1016/j.jeem.2014.01.002

Norby, R.J. and Zak, D.R. Ecological lessons from free-air co2 enrichment (face) experiments. *Annual review of ecology, evolution, and systematics*, 42(1):p. 181, 2011

Norby, R.J., DeLucia, E.H., Gielen, B., Calfapietra, C., Giardina, C.P., King, J.S., et al. Forest response to elevated co2 is conserved across a broad range of productivity. *Proceedings of the National Academy of Sciences of the United States of America*, 102(50):pp. 18052, 2005

Nordhaus, W. Estimates of the social cost of carbon: concepts and results from the dice-2013r model and alternative approaches. *Journal of the Association of Environmental and Resource Economists*, 1(1), 2014

Nordhaus, W.D. An optimal transition path for controlling greenhouse gases. *Science*, 258(5086):pp. 1315, 1992. doi:10.1126/science.258.5086.1315

Nordhaus, W.D. A review of the" stern review on the economics of climate change". *Journal of Economic Literature*, pp. 686–702, 2007

Peters, W., Jacobson, A.R., Sweeney, C., Andrews, A.E., Conway, T.J., Masarie, K., et al. An atmospheric perspective on north american carbon dioxide exchange: Carbontracker. *Proceedings of the National Academy of Sciences*, 104(48):pp. 18925, 2007. doi:10.1073/pnas.0708986104

Petit, J.R., Jouzel, J., Raynaud, D., Barkov, N.I., Barnola, J.M., Basile, I., et al. Climate and atmospheric history of the past 420,000 years from the vostok ice core, antarctica. *Nature*, 399(6735):pp. 429, 1999

Pfeil, B., Olsen, A., Bakker, D.C.E., Hankin, S., Koyuk, H., Kozyr, A., et al. A uniform, quality controlled surface ocean co2 atlas (socat). *Earth Syst. Sci. Data Discuss.*, 5(2):pp. 735, 2012. ESSDD

Piao, S., Sitch, S., Ciais, P., Friedlingstein, P., Peylin, P., Wang, X., et al. Evaluation of terrestrial carbon cycle models for their response to climate variability and to co2 trends. *Global change biology*, 19(7):pp. 2117, 2013

Polvani, L.M., Previdi, M., and Deser, C. Large cancellation, due to ozone recovery, of future southern hemisphere atmospheric circulation trends. *Geophysical Research Letters*, 38(4), 2011

Raftery, A.E. and Lewis, S.M. Implementing mcmc. In *Markov chain Monte Carlo in practice*, pp. 115–130. Springer, 1996

Raich, J.W. and Schlesinger, W.H. The global carbon dioxide flux in soil respiration and its relationship to vegetation and climate. *Tellus B*, 44(2):pp. 81, 1992. ISSN 1600-0889. doi:10.1034/j.1600-0889.1992.t01-1-00001.x

Ramsey, F.P. A mathematical theory of saving. *The economic journal*, pp. 543–559, 1928

Raupach, M., Canadell, J., Ciais, P., Friedlingstein, P., Rayner, P., and Trudinger, C. The relationship between peak warming and cumulative co2 emissions, and its use to quantify vulnerabilities in the carbon–climate–human system. *Tellus B*, 63(2):pp. 145, 2011. ISSN 1600-0889. doi:10.1111/j.1600-0889.2010.00521.x

Raupach, M.R. The exponential eigenmodes of the carbon-climate system, and their implications for ratios of responses to forcings. *Earth System Dynamics*, 4(1):pp. 31, 2013. doi:10.5194/esd-4-31-2013

Raupach, M.R., Gloor, M., Sarmiento, J.L., Canadell, J.G., Frölicher, T.L., Gasser, T., et al. The declining uptake rate of atmospheric co_2 by land and ocean sinks. *Biogeosciences Discussions*, 10(11):pp. 18407, 2013. doi:10.5194/bgd-10-18407-2013

Rayner, N., Parker, D., Horton, E., Folland, C., Alexander, L., Rowell, D., Kent, E., and Kaplan, A. Global analyses of sea surface temperature, sea ice, and night marine air temperature since the late nineteenth century. *Journal of Geophysical Research: Atmospheres (1984–2012)*, 108(D14), 2003

Reynolds, R.W., Rayner, N.A., Smith, T.M., Stokes, D.C., and Wang, W. An improved in situ and satellite sst analysis for climate. *Journal of climate*, 15(13):pp. 1609, 2002

Ricciuto, D.M., Davis, K.J., and Keller, K. A bayesian calibration of a simple carbon cycle model: The role of observations in estimating and reducing uncertainty. *Global Biogeochemical Cycles*, 22(2):pp. n/a, 2008. ISSN 1944-9224. doi:10.1029/2006GB002908

Rintoul, S.R., Meredith, M.P., Schofield, O., and Newman, L. The Southern Ocean Observing System. *Oceanography*, 25(3):pp. 68, 2012. ISSN 1042-8275. doi:http://dx.doi.org/10.5670/oceanog.2012.76

Rodgers, K., Aumont, A., Mikaloff-Fletcher, S., Plancherel, Y., Bopp, L., de Boyer Montégut, C., et al. Strong sensitivity of southern ocean carbon uptake and nutrient cycling to wind stirring. *Biogeosciences Discussions*, pp. bg–2013–377, 2013

Roe, G.H. and Baker, M.B. Why is climate sensitivity so unpredictable? *Science*, 318(5850):pp. 629, 2007

Roemmich, D., Johnson, G.C., Riser, S., Davis, R., Gilson, J., Owens, W.B., et al. The Argo Program: Observing the global ocean with profiling floats. Technical report, 2009. doi:10.5670/oceanog.2009.36

Roy, T., Bopp, L., Gehlen, M., Schneider, B., Cadule, P., Frölicher, T.L., et al. Regional Impacts of Climate Change and Atmospheric CO2 on Future Ocean Carbon Uptake: A Multimodel Linear Feedback Analysis. *Journal of Climate*, 24(9):pp. 2300, 2011. ISSN 0894-8755. doi:10.1175/2010JCLI3787.1

Sabine, C., Hankin, S., Koyuk, H., Bakker, D., Pfeil, B., Olsen, A., et al. Surface ocean co2 atlas (socat) gridded data products. *Earth System Science Data Discussions*, 5(2):pp. 781, 2012

Sabine, C.L., Feely, R.A., Gruber, N., Key, R.M., Lee, K., Bullister, J.L., et al. The Oceanic Sink for Anthropogenic CO2. *Science*, 305(5682):pp. 367, 2004

Sallée, J.B., Shuckburgh, E., Bruneau, N., Meijers, A.J.S., Bracegirdle, T.J., and Wang, Z. Assessment of Southern Ocean mixed-layer depths in CMIP5 models: Historical bias and forcing response. *Journal of Geophysical Research: Oceans*, 2013

Sarmiento, J., Gloor, M., Gruber, N., Beaulieu, C., Jacobson, A., Mikaloff Fletcher, S., Pacala, S., and Rodgers, K. Trends and regional distributions of land and ocean carbon sinks. *Biogeosciences*, 7(8):pp. 2351, 2010

Sarmiento, J.L., Le Quéré, C., and Pacala, S.W. Limiting future atmospheric carbon dioxide. *Global Biogeochemical Cycles*, 9(1):pp. 121, 1995. ISSN 1944-9224. doi: 10.1029/94GB01779

Sarmiento, J.L., Hughes, T.M.C., Stouffer, R.J., and Manabe, S. Simulated response of the ocean carbon cycle to anthropogenic climate warming. *Nature*, 393(6682):pp. 245, 1998. ISSN 0028-0836

Sarmiento, J.L., Gruber, N., Brzezinski, M.A., and Dunne, J.P. High-latitude controls of thermocline nutrients and low latitude biological productivity. *Nature*, 427(6969):pp. 56, 2004. ISSN 0028-0836

Schmidt, G.A., Ruedy, R., Hansen, J.E., Aleinov, I., Bell, N., Bauer, M., et al. Present-day atmospheric simulations using giss modele: Comparison to in situ, satellite, and reanalysis data. *Journal of Climate*, 19(2):pp. 153, 2006

Schuster, U. and Watson, A.J. A variable and decreasing sink for atmospheric co2 in the north atlantic. *Journal of Geophysical Research*, 112(C11):p. C11006, 2007

Screen, J.A., Gillett, N.P., Stevens, D.P., Marshall, G.J., and Roscoe, H.K. The role of eddies in the southern ocean temperature response to the southern annular mode. *Journal of Climate*, 22(3):pp. 806, 2009

Shevliakova, E., Stouffer, R.J., Malyshev, S., Krasting, J.P., Hurtt, G.C., and Pacala, S.W. Historical warming reduced due to enhanced land carbon uptake. *Proceedings of the National Academy of Sciences*, 2013. doi:10.1073/pnas.1314047110

Stern, N.H., Britain, G., and Treasury, H. *Stern Review: The economics of climate change*, volume 30. HM treasury London, 2006

Swart, N. and Fyfe, J. Observed and simulated changes in the southern hemisphere surface westerly wind-stress. *Geophysical Research Letters*, 39(16), 2012

Sweeney, C., Gloor, E., Jacobson, A.R., Key, R.M., McKinley, G., Sarmiento, J.L., and Wanninkhof, R. Constraining global air-sea gas exchange for co2 with recent bomb 14c measurements. *Global Biogeochemical Cycles*, 21(2), 2007

Takahashi, T., Sutherland, S.C., Feely, R.A., and Wanninkhof, R. Decadal change of the surface water pco2 in the north pacific: A synthesis of 35 years of observations. *Journal of geophysical research*, 111(C7):p. C07S05, 2006

Takahashi, T., Sutherland, S.C., Wanninkhof, R., Sweeney, C., Feely, R.A., Chipman, D.W., et al. Climatological mean and decadal change in surface ocean pco¡ sub¿ 2¡/sub¿, and net sea–air co¡ sub¿ 2¡/sub¿ flux over the global oceans. *Deep Sea Research Part II: Topical Studies in Oceanography*, 56(8):pp. 554, 2009a

Takahashi, T., Sutherland, S.C., and Kozyr, A. Global Ocean surface water partial pressure of CO2 database: measurements performed during 1968–2008 (Version 2008). *ORNL/CDIAC-152, NDP-088r*, 2009b

Tjiputra, J., Roelandt, C., Bentsen, M., Lawrence, D., Lorentzen, T., Schwinger, J., Seland, Ø., and Heinze, C. Evaluation of the carbon cycle components in the norwegian earth system model (noresm). *Geosci. Model Dev. Discuss*, 5(4):pp. 3035, 2012

Tol, R.S.J. The Social Cost of Carbon. In Rausser, GC and Smith, VK and Zilberman, D (editor), *ANNUAL REVIEW OF RESOURCE ECONOMICS, VOL 3*, volume 3 of *Annual Review of Resource Economics*, pp. 419–443. ANNUAL REVIEWS, 4139 EL CAMINO WAY, PO BOX 10139, PALO ALTO, CA 94303-0897 USA, 2011. ISBN 978-0-8243-4703-1. doi:{10.1146/annurev-resource-083110-120028}

Treguier, A.M., Le Sommer, J., Molines, J.M., and De Cuevas, B. Response of the southern ocean to the southern annular mode: Interannual variability and multidecadal trend. *Journal of Physical Oceanography*, 40(7):pp. 1659, 2010

Uppala, S.M., Kållberg, P., Simmons, A., Andrae, U., Bechtold, V., Fiorino, M., et al. The era-40 re-analysis. *Quarterly Journal of the Royal Meteorological Society*, 131(612):pp. 2961, 2005

van Vuuren, D.P., Lowe, J., Stehfest, E., Gohar, L., Hof, A.F., Hope, C., et al. How well do integrated assessment models simulate climate change? *Climatic Change*, 104(2):pp. 255, 2011

Vecchi, G.A. and Harrison, M.J. An Observing System Simulation Experiment for the Indian Ocean. *Journal of Climate*, 20(13):pp. 3300, 2007. ISSN 0894-8755. doi:10.1175/JCLI4147.1

Verdy, A., Marshall, J., and Czaja, A. Sea surface temperature variability along the path of the antarctic circumpolar current. *Journal of physical oceanography*, 36(7):pp. 1317, 2006

Wanninkhof, R., Asher, W.E., Ho, D.T., Sweeney, C., and McGillis, W.R. Advances in quantifying air-sea gas exchange and environmental forcing*. *Marine Science*, 1, 2009

Wanninkhof, R., Park, G.H., Takahashi, T., Sweeney, C., Feely, R., Nojiri, Y., et al. Global ocean carbon uptake: magnitude, variability and trends. *Biogeosciences*, 10(3):pp. 1983, 2013. doi:10.5194/bg-10-1983-2013

Watanabe, S., Hajima, T., Sudo, K., Nagashima, T., Takemura, T., Okajima, H., et al. Miroc-esm 2010: model description and basic results of cmip5-20c3m experiments. *Geoscientific Model Development*, 4(4):pp. 845, 2011. doi: 10.5194/gmd-4-845-2011

Waugh, D.W., Primeau, F., DeVries, T., and Holzer, M. Recent Changes in the Ventilation of the Southern Oceans. *Science*, 339(6119):pp. 568, 2013. doi:10.1126/science.1225411

Weatherhead, E.C., Reinsel, G.C., Tiao, G.C., Meng, X.L., Choi, D., Cheang, W.K., et al. Factors affecting the detection of trends: Statistical considerations and applications to environmental data. *Journal of Geophysical Research: Atmospheres*, 103(D14):pp. 17149, 1998. ISSN 2156-2202. doi:10.1029/98JD00995

Webster, M., Jakobovits, L., and Norton, J. Learning about climate change and implications for near-term policy. *Climatic Change*, 89(1-2):pp. 67, 2008. ISSN 0165-0009. doi:10.1007/s10584-008-9406-0

Woloszyn, M., Mazloff, M., and Ito, T. Testing an eddy-permitting model of the southern ocean carbon cycle against observations. *Ocean Modelling*, 39(1):pp. 170, 2011

Zhao, M. and Running, S.W. Drought-induced reduction in global terrestrial net primary production from 2000 through 2009. *Science*, 329(5994):pp. 940, 2010. doi:10.1126/science.1192666